Stony Brook University

Real-time Investigation of Li Microstructure Formation on Li Anodes for Li Batteries by Solid-state Li NMR, SEM, MRI and X-ray Tomography

A Dissertation Presented

by

Hee Jung Chang

to

The Graduate School

in Partial Fulfillment of the

Requirements

for the Degree of

Doctor of Philosophy

in

Chemistry

Stony Brook University

August 2015

Stony Brook University

The Graduate School

Hee Jung Chang

We, the dissertation committee for the above candidate for the
Doctor of Philosophy degree, hereby recommend
acceptance of this dissertation.

Clare P. Grey, Ph.D., Advisor

Professor, Department of Chemistry, Stony Brook University

Michael G. White, Ph.D., Chairperson

Professor, Department of Chemistry, Stony Brook University

Lisa Miller, Ph.D., Third Member

Professor, Department of Chemistry, Stony Brook University

Robert Kostecki, Ph.D., Outside Member

Senior Scientist, Environmental Energy Technology Division,
Lawrence Berkeley National Laboratory

This dissertation is accepted by the Graduate School

Charles Taber

Dean of the Graduate School

Abstract of the Dissertation

Real-time Investigation of Li Microstructure Formation on Li Anodes for Li Batteries by Solid-state Li NMR, SEM, MRI and X-ray Tomography

by

Hee Jung Chang

Doctor of Philosophy

in

Chemistry

Stony Brook University

2015

With increasing demands for higher energy storage, Li metal with the highest possible energy density and specific capacity of 3800 mA h g^{-1} has come back into focus as an attractive candidate for an anode material. However, there are still critical difficulties involving safety issues caused by the growth of Li microstructures (dendrites and moss) during cycling, which prevent its use in practical applications. In order to solve the various problems, fundamental understanding of behavior of Li metal anodes in working batteries and the conditions under which Li microstructures are formed is necessary

In situ NMR has a demonstrated ability to capture real time structural changes that are not obtainable via ex situ studies, such as the formation of metastable states and microstructural Li. In this research, I provide the first assignments of the Li metal NMR shifts to the different microstructure morphologies observed by SEM. The assignments are supported by susceptibility calculations, the results being critical in the development

of a method to monitor cell failure in situ. Magnetic resonance image (MRI) has also been performed to study the change in concentration of the lithium ions in the electrolyte in the vicinity of the electrode interface during current flow. Sand's time theory[1] is employed to investigate the relationship between dendrite formation and electrolyte concentration. Non-destructive X-ray phase contrast tomography was applied to further characterize electrochemical Li symmetrical cells. In situ tomography allows examination of microstructure growth in 3D at high resolution. The multiple growth and removal mechanisms reflect the complexity of the lithium electrodeposition and dissolution process in Li batteries.

The ability of the techniques performed here to distinguish between mossy and dendritic-type morphologies lays the groundwork for future investigations of Li depositions aimed at identifying the conditions (e.g., additives, applied current) where microstructural formation is minimized in practical Li metal-based batteries such as Li/S and Li/air.

1. C. Brissot, M. Rosso, J.-N. Chazalviel and S. Lascaud, *J. Electrochem. Soc.*, 1999, **146**, 4393-4400.

Table of Contents

List of Abbreviations

2D, 3D	two-dimensional, three-dimensional
BMS	bulk magnetic susceptibility
C4mpyr TFSI	butyl-methylpyrrolidinium bis(trifluoromethanesulfonyl)imide
CSI	chemical shift imaging
DEC	diethyl carbonate
DEE	diethyl ether
DLA	diffusion-limited aggregation
DMC	dimethyl carbonate
DME	dimethyl ether
DOL	1,3-dioxolane
DOS	density of states
EC	ethylene carbonate
EMC	ethyl methly carbonate
ESR	electron spin resonance
EV	electric vehicle
FEC	fluoroethylene carbonate
FFT	fast Fourier transform
FID	free induction decay
FOC	field of view
FT	Fourier Transformation
FWHM	full width at half maximum
G/L	Gaussian/Lorentzian
HEV	hybrid electric vehicle
HSAL	high surface area lithium
LIB	Li-ion battery
MAS	magic angle spinning
MRI	Magnetic resonance image
NMR	nuclear magnetic resonance
OCV	open circuit voltage
PC	propylene carbonate
PMMA	poly(methyl methacrylate)
RF	radio frequency
SEI	solid electrolyte interphase
SEM	scanning electron microscopy
SHES	self-healing electrostatic shield
SOC	state of charge

SS	solid-state
TE	total echo time
TEM	transmission electron microscopy
TFSI	bis(trifluoromethanesulfonyl)imide
TIP	temperature independent paramagnetism
TR	repetition time
VC	vinyldene carbonate
VSP	biologic potentiostat/galvanostat

List of Figures/Tables

Chapter 1

Chapter 2

Chapter 3

Chapter 4

Chapter 5

Acknowledgments

I would like to gratefully and sincerely thank my advisor, Professor Clare P. Grey for her guidance, understanding, patience, and most importantly, endless support during my graduate studies at Stony Brook University. Her wisdom, knowledge and commitment to the highest standards inspired and motivated me not only as a scientist but also as an instructor. It has been a wonderful experience working with such a great group of people.

I also thank my parents for the encouragement, attention and unconditional love. All the support they have provided me over the years was the greatest gift anyone has ever given me.

I would also like to express my gratitude to all of my committee members: Professor. Michael White, Lisa Miller and Dr. Robert Kostecki who graciously agreed to serve on my committee, when they were probably up to their neck in work.

I would like to acknowledge the collaborators for great assistance: Jim Quinn for SEM experiments (Department of material science), Alexej Jerschow (New York University) for MRI research, Dillip Gersappe for simulation (Department of material science) and the beamline team at Diamond in UK.

I would also like to thank the past and present group members: Lin-Shu Du, Dongli Zeng, Srinivasan Shekar, Paul Baley, Gunwoo Kim and especially Andy Ilott and Nicole Trease for their great help and support. I need to further thank all my friends, particularly Hyeyoung Jung, who has always been my company for the past 5 years and took some time to listen, even when I was just complaining. I will never forget our coffee time every in the morning at SAC.

Finally, I deeply thank my parents, younger brother, and my precious friend Hyeongho Shin for the encouragement, attention and unconditional love. All the support they have provided me over the years was the greatest gift anyone has ever given me. Without them, I may never have gotten to where I am today.

사랑합니다 그리고 감사합니다.

Vita, Publications and/or Fields of Study

- H. J. Chang, N.M. Trease, D. Zeng, L.-S. Du, C.P. Grey. "Investigating Li Microstructure Formation on Li Anodes for Lithium Batteries by In Situ ^{6}Li/^{7}Li NMR and SEM", *Journal of Physical Chemistry C*. **2015,** *119*, 16443-16451.

- H. J. Chang, A. J. Ilott, M. Mohammadi, N. M. Trease, A. Jerschow, C. P. Grey. "Correlating microstructural lithium growth with electrolyte salt depletion using in situ ^{7}Li MRI." (In preparation)

- S. Chandrashekar, N.M. Trease, H. J. Chang, L.-S. Du, C.P. Grey, and A. Jerschow. "^{7}Li MRI of Lithium Ion Batteries." *Nature Materials.* **2012**, *11,* 311-315.

- N.M. Trease, L. Zhou, H. J. Chang, B.Y, Zhu, and C.P. Grey. "In *Situ* NMR of Lithium Ion Batteries: Bulk Susceptibility Effects and Practical Considerations." *Solid State Nuclear Magnetic Resonance.* **2012**, *42,* 62-70.

- D. S. Eastwood, P. M. Bayley, H. J. Chang, O. O. Taiwo, Z. Liu, J. Vila-Comamala, C. Rau, P. J. Withers, P. R. Shearing, C. P. Grey, P. D. Lee. "Three-dimensional Characterization of Lithium Dendrite Structures using Synchrotron X-ray Phase Contrast Imaging" *Chemical Communications*. **2014**, *51*, 266-268

- A. J. Ilott, S. Chandrashekar, A. Klöckner, H. J. Chang, N. M. Trease, C. P. Grey, L. Greengard and A. Jerschow. "Visualizing Skin Effects in Conductors with MRI: ^{7}Li MRI Experiments and Calculations" *Journal of Magnetic Resonance*. **2014**, *245*, 143-149.

Chapter 1

Introduction

1.1 Motivation

The use of Li metal anodes in secondary lithium ion batteries (LIBs) provides the highest possible energy density.[2] Nevertheless, there are problems associated with the use of Li metal, such as short cycle life, lack of safety and poor thermal stability. These have prevented the use of metal as the anode in commercial LIBs. Many of these problems are associated with morphological changes on the lithium metal surface such as uneven growth of microstructure (dendrite or moss) on the metal surface upon charge-discharge cycling and formation and degradation of a solid electrolyte interface (SEI) on the electrodes.[3-5] These limitations eventually lead to a failure of the practical application of lithium metal as an anode. Various attempts by different methods have been made to prevent the drawbacks of using lithium metal anodes by using different types of separators and electrolytes, introducing additives, and coating the electrode for better surface adhesion.[6-11] However, details of the mechanism of dendritic or mossy Li formation and the functions of SEI in lithium batteries are not fully understood; and the common methods that have been used have generally been limited to only qualitative information about the amount and type of microstructure. Therefore, in this research, *in situ* NMR, MRI, X-ray tomography and SEM carefully were performed for both quantitative and qualitative studies of the electrochemical conditions of growth of Li dendrites or moss.

1.2 Battery Fundamental

1.2.1 General Background

A battery is a form of electrochemical energy storage that produces electricity from a chemical redox reaction. In 1800, Alessandro Volta developed the first electrochemical cell and over the past 200 years the development of batteries has progressed continuously. As energy demand and consumption have rapidly increased in the world, the need for batteries with increased cycle life has grown considerably for use in a diverse range of applications.

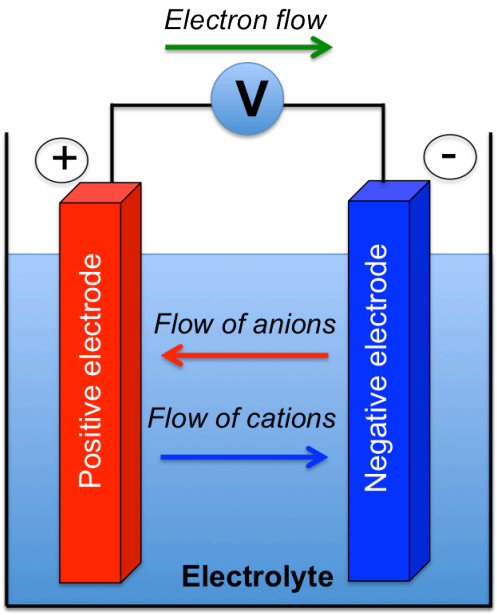

Figure 1.1 Diagram of the basic battery components.

All batteries are composed of a cathode (positive electrode) and an anode (negative electrode) separated by an electrolyte medium (Figure 1.1). The two electrodes have different chemical potentials and this difference gives the voltage supplied by a battery. The electrolyte is an ion conductor that can be aqueous or non-aqueous in liquid, paste, or solid form. For liquid electrolytes, a thin porous film referred to as separator is used to prevent physical contact

between the positive electrode and the negative electrode but allows the cations of the electrolyte to flow through it.

There are two main types of batteries; primary batteries and secondary batteries. Practically, the difference between the two batteries is the reversibility of the electrochemical reaction[1]. Primary batteries are assembled in their charged state and can be used (give current) immediately. Once, primary batteries are discharged, they are discarded as the chemical reactions that supply the current are irreversible. They are typically used in the areas where the initial cost must be economical for the consumer products and where recharging is not feasible for electronic products. Alkaline cells and carbon-zinc cells are the most common examples of primary batteries on the market.

Secondary batteries are designed to be rechargeable and used many times. Typically,

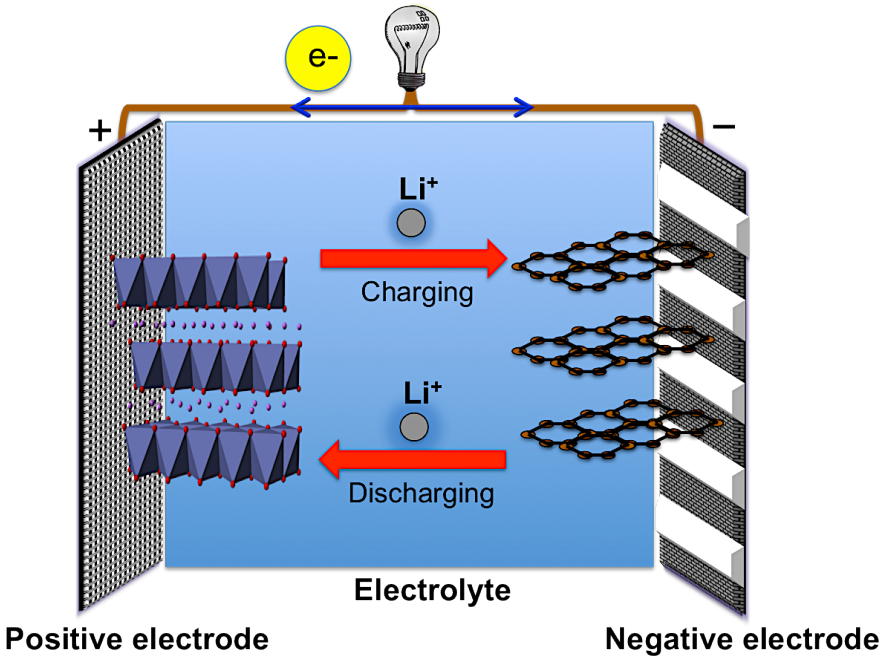

Figure 1.2 An example of the charge/ discharge intercalation mechanism in LIBs. The insertion or intercalation process is when lithium ions migrate and become embedded (i.e. intercalated) in the porous electrode material (e.g. Carbon). The lithium ions are inserted into the layered structure (e.g. $LiCoO_2$). When lithium ions are removed from the layered material it is referred to as extraction or de-intercalation.

secondary batteries are assembled in their discharged state and need to be charged prior to use. In secondary batteries, the electrochemical reactions between positive and negative electrode are reversible. The current is applied to the battery from devices that are called chargers or rechargers. They are mostly used in industrial and automotive applications, computers, cell phones, and mp3 players. In the 19th to the early 20th century, only two batteries, lead-acid and nickel-cadmium (NiCd), were commercially a success. Recently, nickel-metal hybrid batteries and lithium-ion batteries were introduced and have been used in various applications[12] as described in Table 1.

Since the early 1990s, LIBs have become commercially available after the initial announcement by Sony and they are used now world-wide.[2, 12, 13] The first secondary LIBs worked using an insertion mechanism and consisted of titanium sulfide (TiS_2), that has a layer structure, as the cathode, metallic lithium as the anode, and a non-aqueous electrolyte. However, due to several serious safety and cycle life issues associated with metallic lithium anodes discussed in the following sections, another careful selection of cathode and anode pairs was required. Today, most LIBs function using intercalation reactions where lithium ions are inserted into or extracted from a host matrix (e.g. $LiCoO_2$ cathode/ graphite anode) with retention of the crystal structures of electrodes, shown in Fig. 1.2.

1.2.2 Criteria for battery materials

In general, battery materials are identified by several parameters: potential (V), which is difference in voltage between cathode and anode, specific capacity (Ah/kg), which is how much electric charge can be stored per mass, specific energy (gravimetric energy, Wh/kg) and energy density (volumetric energy, Wh/L) which is the internal energy in a battery per mass and per volume, respectively.[14] These parameters are very important criteria for battery evaluation. As an example, the gravimetric and volumetric specific capacities for several materials that function as the anode in LIBs are shown in Fig. 1.3. The theoretical capacity was calculated based on the maximum Li-containing phase of Li-M binary phase (LiC_6, $Li_{22}M_5$ [M= Si, Ge, Sn, Pb]).[15]

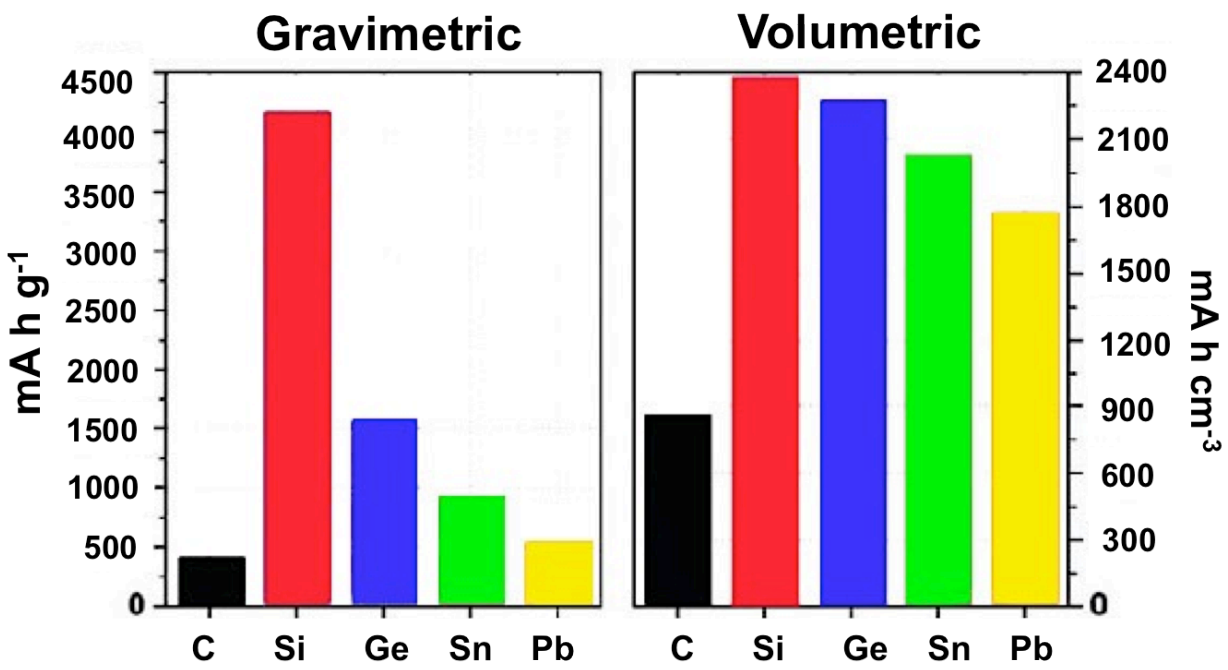

Figure 1.3 Gravimetric and volumetric specific capacities of several Li alloying anode materials for lithium batteries. (The Figure is adapted from reference 15.)

Table 1.1. Comparison of different types of Secondary batteries: the lead-acid (Pb-acid), Nickel-Cadmium (NiCd), Nickel-metal hybrid (NiMH), and LIB.[12, 13, 16]

Battery Type	Pb-acid	NiCd	NiMH	Lithium-ion/polymer
Nominal Voltage (V)	2.0	1.25	1.25	3.5
Gravimetric Energy (Wh/kg)	30-40	40-60	30-80	100-265
Volumetric Energy (Wh/L)	60-75	150-190		250-620/730
Cycle Life	200 to 300	1000 to 1500	500 to 1000	400 to 1200
Self discharge (per month)	5%	20%	30%	< 5%
Advantage	• Low cost • Established recycling process • Stationary energy storage for uninterruptible power	• Tolerating deep discharge for long periods • High energy density	• High energy density • Stable energy storage • Low environmental impact	• High energy density (Vs Pb) • Good low temperature performance (Vs Pb) • Light weight (Vs Pb) • High rate capability (Vs Pb) • No memory effect (Vs Ni) • Low self-discharge (Vs Ni)
Application	• Motor vehicle starting, lighting and ignition (SLI) batteries • Large backup power supplies	• Potable electronics and toys • Cordless and wireless tools	Best choice for hybrid electric vehicles: Toyota Prius, Honda Insight, Ford Escape, Chevrolet Malibu	Portable electronic devices Electric vehicle (Tesla)

1.3 Research Objective

1.3.1 Li metal anode

Lithium metal has the atomic number 3, a very low atomic weight and a low density (0.534g/cm^3). It has the lowest voltage (-3.045V vs. standard hydrogen electrode) and provides the largest gravimetric energy density (3860 mA h g^{-1}) among metallic anode materials, which is ten times greater than the most commercially available anode, graphite (372 mA h g^{-1})[13, 17] Figure 1.4 shows voltage versus capacity for positive- and negative-electrode materials presently used or under serious considerations for the next generation of rechargeable Li-based cells. The output voltage values for Li-ion cells or Li-metal cells are represented.

Depending upon the cathode material, lithium metal cells can produce voltages from 1.5V up to 4V, which is higher than lead/acid (2.1V) and zinc-carbon cells (1.5V). In the late 20th century, because lithium metal has the greatest electrochemical potential, it became the most attractive material for anode candidates and has been commercialized for various applications as

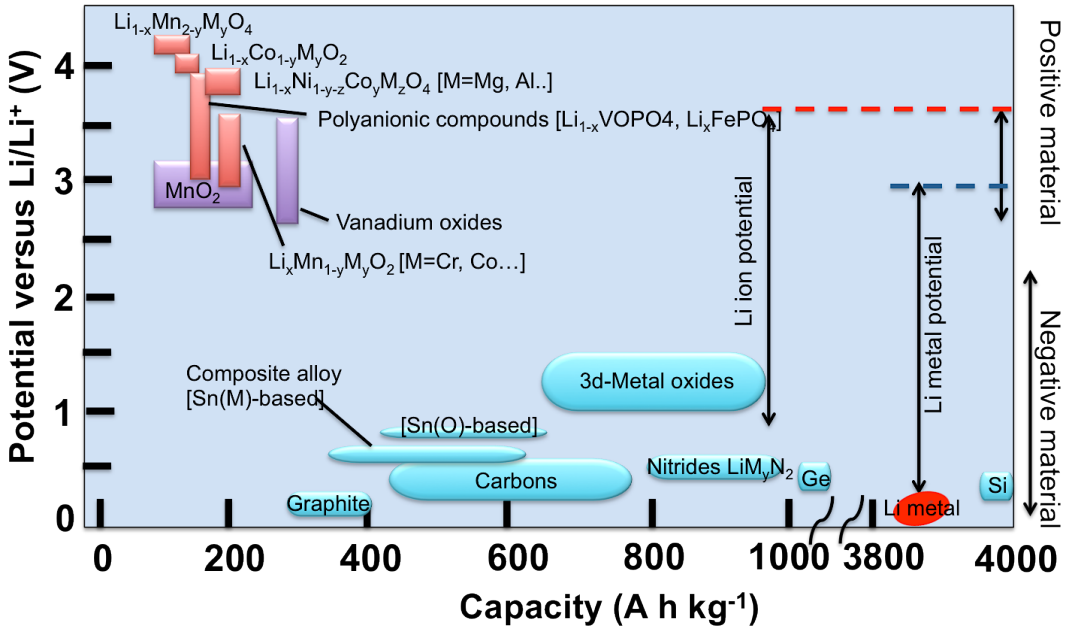

Figure 1.4 Electrode materials of LIBs. (The Figure is adapted from the reference 1.)

primary batteries such as lithium iron disulfide (Li-FeS_2), lithium manganese dioxide (Li-MnO_2), and lithium-thionyl chloride (Li-$SOCl_2$).

However, practical applications using Li metal for secondary batteries are still hindered due to the safety problems related to dendrite growth. The find a solution to these problems, a fundamental understanding of the behavior of Li metal anodes in working batteries and the conditions under which Li microstructures are formed are necessary.

1.3.2 Li deposition in Li batteries

In contrast to the significant developments in lithium insertion compounds during the 1970s and 1980s, lithium metal batteries have experienced very slow progress due to safety issues arising from formation of microstructures, particularly dendrites at the metallic lithium anode upon repeated stripping and plating of lithium especially at high rate charge and discharge. Once formed the dendrites can break, resulting in "dead lithium" or, in a much worse case, penetrate the separator leading to short-circuits and possible fires or explosions.

The formation and nature of the microstructures is thought to depend on many factors including charge and discharge current densities, the type of electrolyte, the SEI formation and degradation, the stack pressure generated inside a battery (i.e., the pressure exerted on the stack of current collectors, electrodes and separator) and the type of separator.[6-11] The mechanical properties, porosity, ionic resistance, thickness, etc., of the separator can all affect the formation of microstructures and their morphologies.[8, 10] Growth is hindered at slow current rates, and by the use of high stack pressure, although it is still not clear whether conditions exist where it is completely fail-safe to charge a Li metal battery.[12, 18-20]

When a battery starts to function, the lithium metal chemically reacts with non-aqueous electrolyte and the solid electrolyte interphase (SEI) layer immediately forms on it.[4, 21, 22] The SEI is thought to play a role in preventing physical contact and side reactions between a metallic lithium anode and the electrolyte. The electrolyte salt and solvent mainly influences SEI

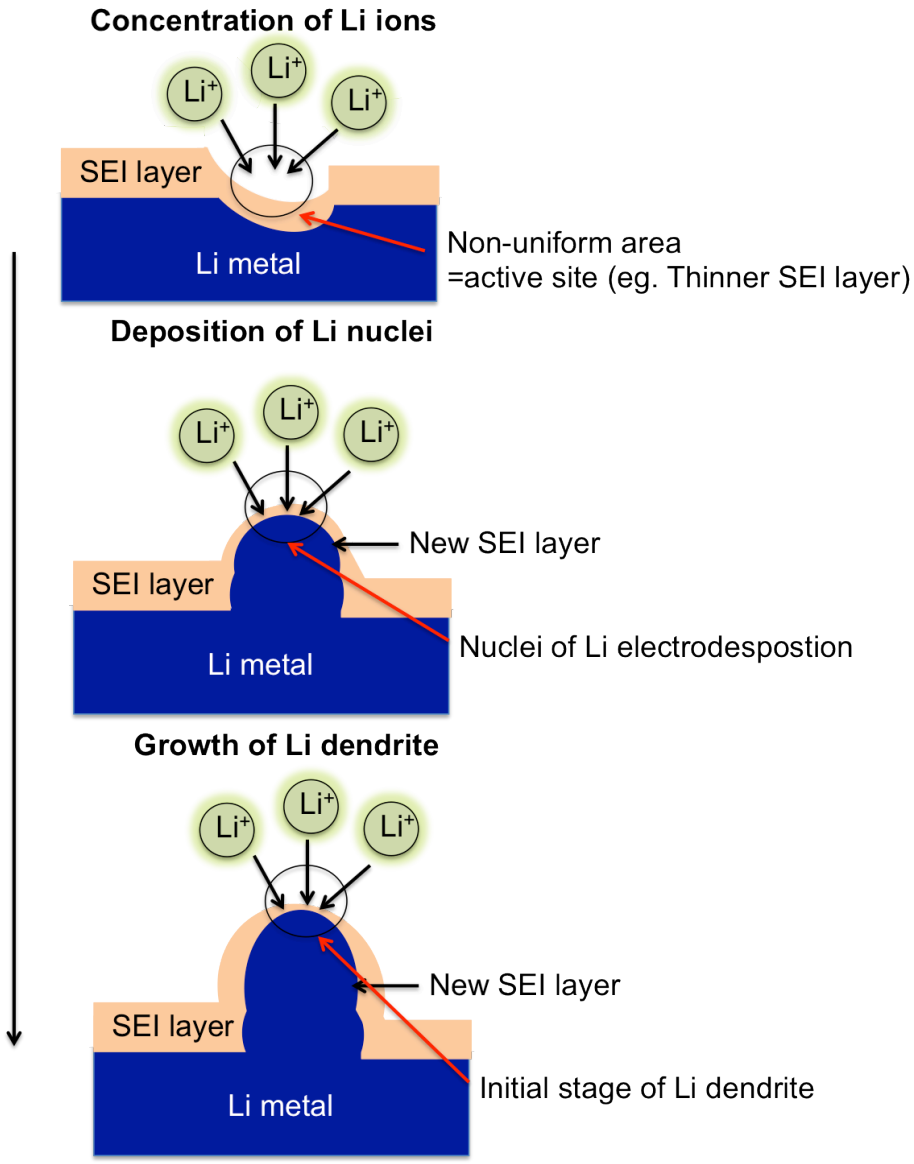

Figure 1.5 Schematic illustration of a possible path of dendrite formation on lithium metal surface (The Figure is adapted from reference 21)

composition as it is consists of insoluble byproducts from electrolyte decomposition.[6, 23, 24] It is generally believed that the repeated breakdown and repair of the surface film can generate in non-uniform Li deposition (in Figure 1.5).[6, 23, 24] Therefore, formation of adequate SEI layer is a important factor to prevent growth of dendrites.[21]

1.3.3 The observation methods of Li deposition

Scanning electron microscopy (SEM), transmission electron microscopy (TEM) and optical microscopy, have been used to visually investigate electrodeposition in batteries.[25-28] The first direct observation of Li microstructures in Li/ Li and Li/ Li-Al alloy coin cells with a liquid organic electrolyte was reported by Epelboin *et al.* in 1980, using TEM.[29] Subsequently, *in situ* SEM was used by Yamaki and coworkers to view Li microstructures in a Li coin cell with a liquid electrolyte system.[19] In 1993, Yamaki and coworkers used *in situ* optical microscopy to monitor Li deposition; they reported that the amount of needle-like Li deposits decreased with decreasing current density, which correlated with improved cycle life.[30]

Lopez *et al*. reported the growth of dendritic/mossy surfaces at the micrometer- and submicrometer scale by using SEM.[27] Coin cells using a lithium metal electrode and a $Li_4Ti_5O_{12}$

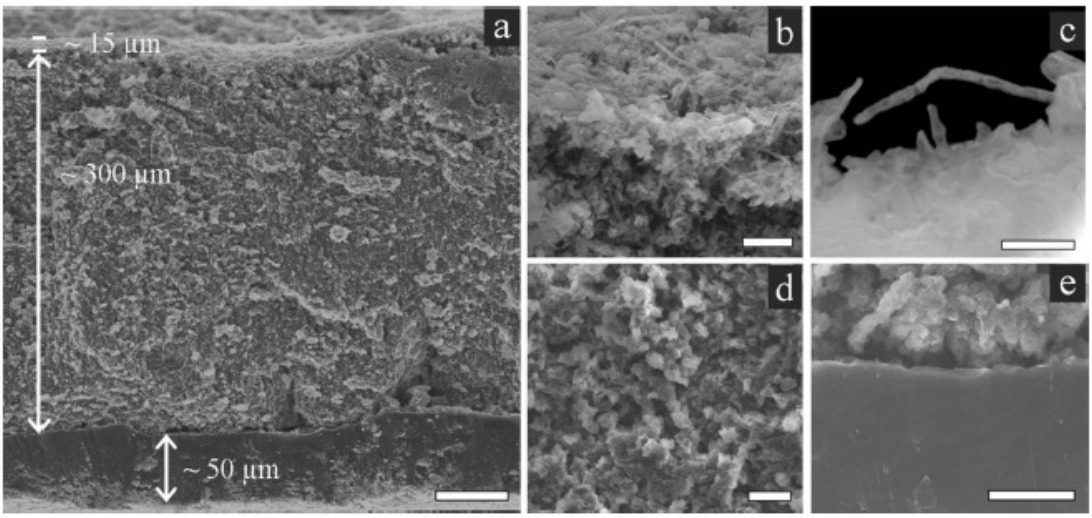

Figure 1.6 SEM images from reference 27 showing morphological features of lithium metal after 250 cycles (a) Low magnification image of the different layers, (b) the dendrite layer, (10~15 µm thick) (c) needle-like dendrite in the dendrite layer, (d) the porous layer (280~300 µm thick) and residual layer (50~60 µm thick), (e) the interphase region between porous layer and residual metallic lithium. The white scale bars represent (a) 50 µm, (b, d, e) 10 µm and (c) 2 µm. (The Figure is taken from reference 27)

electrode in 1.2M $LiPF_6$ dissolved in ethylene carbonate (EC): ethyl methyl carbonate (EMC) (30:70 wt%) were analyzed before and after cycling. Interestingly, they found three morphologically distinct regions, assigned as a top dendritic layer, an intermediate porous layer, and a residual lithium layer (the initial anode metal), which grow up from the bottom to the surface of lithium metal anode. The direct relationship of cell failure and capacity loss is suggested to be due to a decrease in residual lithium thickness and drying of the electrolyte, as shown Figure 1.6.[27] Since the formation of dendrites is generally accepted as one cause of battery failure, the results from Lopez *et al*. motivated this *in situ* NMR study. Although various methods have been used to study electrodeposition in order to understand the mechanisms involved, they have generally provided only qualitative information about the amount and type of microstructure.

Nuclear magnetic resonance (NMR) and magnetic resonance imaging (MRI) have been used in the study of battery electrode materials.[31-33] Bhattacharyya *et al*. first monitored metallic lithium deposited on the lithium metal anode by using *in situ* NMR and were able to resolve distinct signals from bulk Li metal in the electrodes and from the Li metal microstructures.[34] They developed a method to quantify the amount of microstructure (dendrite or mossy Li) formed by using simple calculations based on the skin depth (d), how far a radiofrequency (rf) pulse can penetrate into the metal (see section 1.4.3), of a bulk metallic Li strip under rf excitation. In their study, three different cells were investigated to observe the formation of Li microstructures at different stages. In addition, two different ionic liquids were tested to prevent dendrite formation. The results showed that it is possible to monitor from the early stages of dendrite formation in Li batteries and quantify them. MRI techniques have been applied by Chandrashekar *et al*. to study Li metal batteries *in situ* and utilized chemical shift imaging (CSI) to identify two different types of Li microstructure, one on the Li metal surface and one growing between the electrodes.[35] Dendrites extending far from the Li anode were shown to give rise to a narrow range of shifts, whereas other microstructures closer to the electrode surface gave rise to broad resonances. More recently, Indris *et al.* investigated dendrite formation in different electrolytes using *in situ* ^{7}Li NMR. They observed the more efficient suppression of dendrite growth in an ionic liquid than the standard electrolyte of 1M $LiPF_6$ in EC: dimethylene carbonate

(DMC).[36]The use of *in situ* electron spin resonance (ESR) has recently been demonstrated,[37, 38] the temperature independent paramagnetism (TIP)[34, 39] of Li metal giving rise to an ESR signal that is dependent on the geometry of Li metal as well as sample impurities. The order of magnitude greater skin depth in NMR experiments (d = 17 μm) compared to ESR experiments (d = 1 μm)[37] gives NMR the ability to detect and quantify thicker and more dense microstructures. Although, the ESR method is currently only semi-quantitative[37] the inherent increased sensitivity of ESR compared to NMR may allow the early stages of Li microstructure formation to be tracked, suggesting that the ESR and NMR experiments will provide complementary information.

1.3.4 The mechanistic models of Li microstructure growth.

Dendrite growth in Li batteries has been observed in many studies and there are two different growth mechanical models that have been proposed; tip-controlled growth and base-controlled growth. Significant differences in the preferential growth location have been described using mechanistic models such as the Barton and Bockris surface-tension model in which overpotentials are related to surface diffusion,[40] a Brownian statistical simulation model which generalized the particle diffusion-limited aggregation (DLA) process,[41] the Chazalviel and Rosso electromigration-limited models[42, 43] (discussed in Chapter 4) and Yamaki's model.[44]

The Barton and Bockris[40] model proposes that overpotential threshold is required for initiation and propagation of zinc dendrite growth. They proposed that the acceleration of dendrite growth at the protrusion rather than the electrode surface arises from the conditions of spherical diffusion around the tip of the protrusion while linear diffusion occurs on the rest of the smooth surface. The threshold of the initiation and the propagation of dendrite growth is determined from the critical overpotential where diffusion is altered from linear to spherical.

In the Brownian simulation model,[41, 45] two parameters are considered to predict morphology of electrodeposition; the sticking coefficient, which refers to the deposition probability of a mobile cation to the metal surface, and the concentration of particles in the

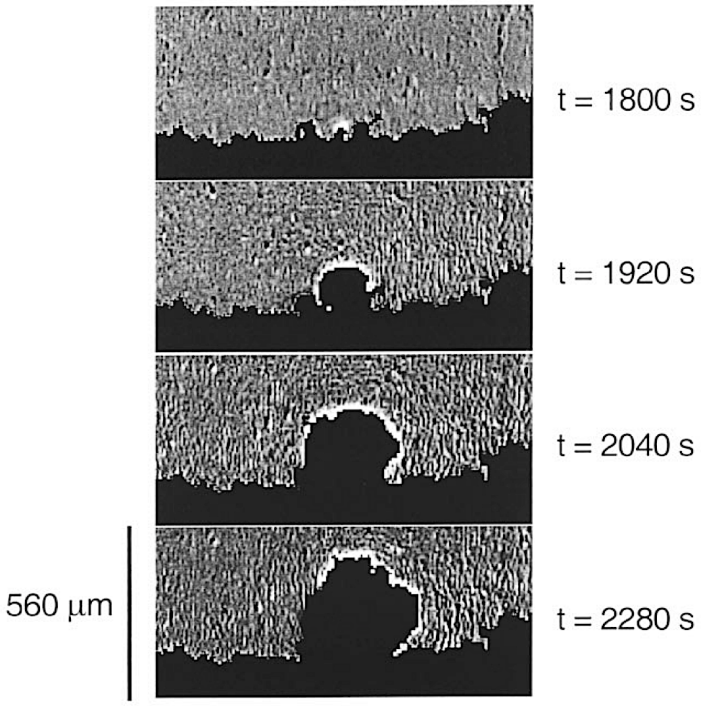

Figure 1.7 At high current densities of 0.7 mA cm^{-2} the dendrites have an arborescent-like morphology. These pictures evidence the existence of large concentration gradients at the top of the growing dendrite. The highest concentration gradient is shown in white color. (The Figure is from reference 42.)

electrolyte solution. The model excludes any physical parameters such as surface tension, reaction kinetics, or surface roughness, although these quantities are partly encapsulated in the value of the sticking coefficient. Low sticking probability gives rise to denser structures because the cations are able to diffuse into the existing microstructure before deposition, while high sticking probability results in deposition at extremities of the microstructure, leading to dendrite growth. Further modifications have been made using different determinations of deposition probabilities depending on multiple parameters such as the overpotential, the limiting current density, the exchange current density and electrolyte concentration.[46-48]

Unlike the diffusion-controlled mechanism in the above two models, the Chazalviel model explores dendrite growth triggered by changes in the electrolyte concentration at the surface of the electrode.[42] Chazalviel predicts two different behaviors in the ionic concentration gradient; at low and high current density. At low current density the concentration gradient in the electrolyte reaches a steady state, resulting in a stationary ion distribution and potential in the cell, with no

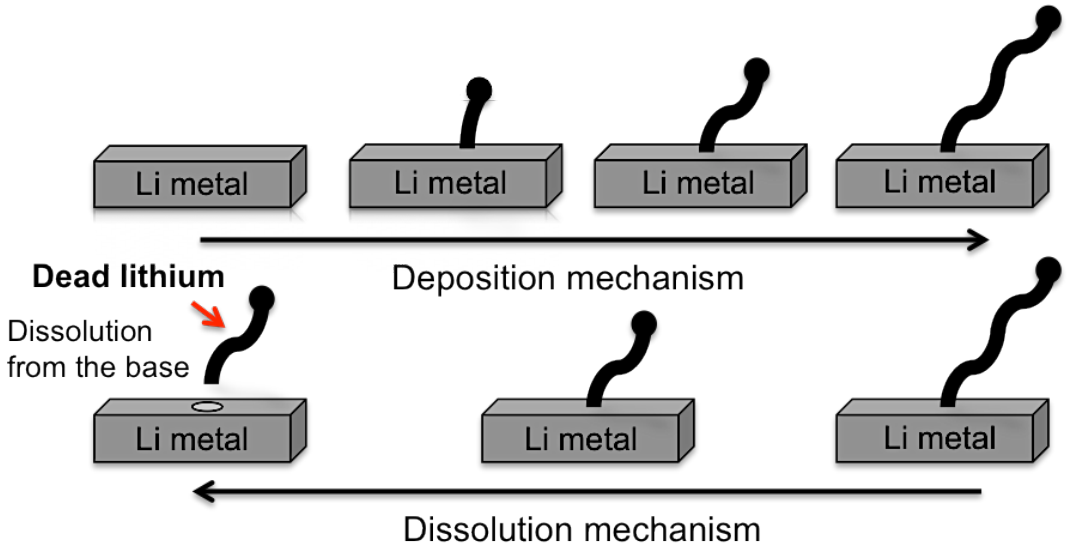

Figure 1.8 Yamaki model of lithium deposition and dissolution at the Li electrode. (The Figure is adapted from reference 44.)

dendrite growth expected. In contrast, at high current density, a steady state is not reached, and the concentration continuously depletes in the vicinity of the negative electrode until eventually the anion concentration drops to zero (Figure 1.7). The excess of positive charge violates charge neutrality producing a large space charge and electric field at the electrode. The large electric field results in nucleation and unavoidable dendrite growth. [1, 43, 49]

Yamaki *et al*. also reported that Li deposition occurs from the base instead of at the tip of existing protrusions, at least in the early stage of dendrite formation, where the surface tension created by Li deposition between SEI layers and Li surface is large enough to deform the existing Li dendrites (Figure 1.8).[44] Kohl *et al*. experimentally observed dendrite growth from the tip, as well as from the base using *in situ* optical microscopy and *ex situ* SEM experiments.[50] The growth at the tip, which is the electrochemically active site, is an electrochemical process, while the extrusion-based growth is thought to be a surface tension mechanism, which was proposed by Yamaki group[44] indicating a build-up of stress caused by the solid electrolyte interface (SEI) layer covering the metal surface. The deposition rate at the tip is significantly higher than at the sidewalls or base.

1.4 NMR

1.4.1 General Background

Nuclear Magnetic Resonance (NMR) is a very powerful and useful technique to study the local environment of a nucleus, which is based on the interaction of a nuclear dipole moment with a static magnetic field.

In NMR, the total interaction energy of nucleus is the sum of all interactions, such as Zeeman interaction (H_z), chemical shielding (H_σ), dipolar coupling (H_d), J-coupling (H_j), Knight shift (H_k), and paramagnetic interactions (H_p) as given in Equation 1.1.

$$H = H_Z + H_\sigma + H_d + H_j + H_k + H_P \tag{1.1}$$

Each of these interactions contributes to the total frequency of the nucleus. Where some interactions cause a shift of the frequency, others induce a broadening of the peak.

When a nucleus with a nuclear magnetic dipole moment, also referred to as a "spin", is placed in a magnetic field, the spin behaves as a magnetic moment vector and aligns itself with the external field, up or down, known as the Zeeman interaction. A radio frequency pulse can excite the nuclear spins at a specific resonance frequency, ω_0.

$$\omega_0 = \gamma \times B_0 \tag{1.2}$$

In Equation 1.2, ω_0 is the Larmor frequency, $\mathbf{B_0}$ is the magnetic field strength and γ is the gyromagnetic ratio of the nucleus. The electrons near the nucleus circulate about the direction of the applied magnetic field. This circulation induces a small magnetic field at the nucleus, which mostly opposes the externally applied field. The effective magnetic field at the nucleus is therefore generally less than the applied field, the reduction being referred to as shielding. The

effective magnetic field induces a difference in frequency of the observed atom, ω, called chemical shielding (σ), in Equation 1.3.

$$\omega = (1-\sigma)\omega_0 \tag{1.3}$$

Since different atomic nuclei within a molecule resonate at different radio frequencies for the same magnetic field strength, they can be easily separated in NMR spectra. In NMR, frequencies are usually referenced to a frequency ω_{ref}, this is referred to as the chemical shift (δ) (note that ω_{ref} is typically set to ω_0).

$$\delta = \frac{\omega - \omega_{ref}}{\omega_{ref}} \tag{1.4}$$

In this study, besides the Zeeman interaction, the other major interactions contributing to the NMR shift are the Knight shift and paramagnetic interactions, which will be introduced briefly in the following section. In addition, bulk magnetic susceptibility (BMS) and skin depth effects need to be considered when measuring static NMR signals of a metal. They will be discussed in section 1.4.3.

1.4.2 The Knight Shift and Paramagnetic Interactions

The Knight shift is a measure of the density of states at the Fermi level in a metal, it arises due to the conduction electrons, which are delocalized in metals.[51, 52] The conducting electrons occupy a Fermi distribution within the electronic states of the material from the lowest energy up to the Fermi energy in a pair-wise fashion due to the Pauli Exclusion Principle. Without an external field, spin-up and spin-down states are degenerate (equally populated), however, under a magnetic field there is a shift in energy of the spin-up and spin-down states leading to a population difference. The imbalance in the number of these states leads to an extra effective field at a given nucleus in an external field, and hence an associated susceptibility termed as the

Pauli susceptibility. The magnitude of this field can be calculated as $\Delta B = \frac{2\mu_0}{3}\chi_p \Omega \langle \psi(0)^2 \rangle_F B_0$; χ_p is the Pauli susceptibility produced by the conducting electrons, Ω is the volume per electron, ψ the wave function of the electron at the nucleus (r=0) and $\mathbf{B}_0$, the external magnetic field. This effect is dominated by s-electrons, as only s-electrons have significant density at the nucleus. The Knight shift is generally positive and much larger than the chemical shielding; typical values are 5200 ppm for Ag, 25000 ppm for Hg and 250 ppm for Li metal. In this study, it is the major contribution of the large shift of the Li metal peak, since the typical range for diamagnetic Li is from 10 ppm to -10 ppm.

In a paramagnetic material, there are two dominant interactions, the Fermi-contact shift and the dipolar coupling.[33] The Fermi-contact is a measure of a non-zero delocalized electron density of the unpaired electrons that are transferred from the paramagnet to the NMR nucleus through the bonds. The dipolar interaction is a through-space coupling between the magnetic moment of the studied nucleus and the electronic spins; causing a broadening resulting in large spinning side band manifolds under MAS conditions (see section 1.4.4).

1.4.3 BMS effect and Skin depth

When a paramagnetic material placed in a static magnetic field, the field varies across the material in a way that depends on three important factors; the sample shape, packing of the particles that comprise the material, and the orientation of the sample with respect to the field, giving rise to the bulk magnetic susceptibility (BMS) effects.

Bulk magnetic susceptibility (BMS) effects are seen in many *in situ* NMR experiments. They can be studied by modifying the orientation (parallel and perpendicular) of lithium metal with respect to the magnetic field.[28, 53, 54] In ^{7}Li NMR spectra, when a lithium metal strip is oriented parallel ('vertical') to the magnetic field the metal peak is shifted to greater values than when it is oriented perpendicular ('horizontal') as shown in Figure 1.9.[53]

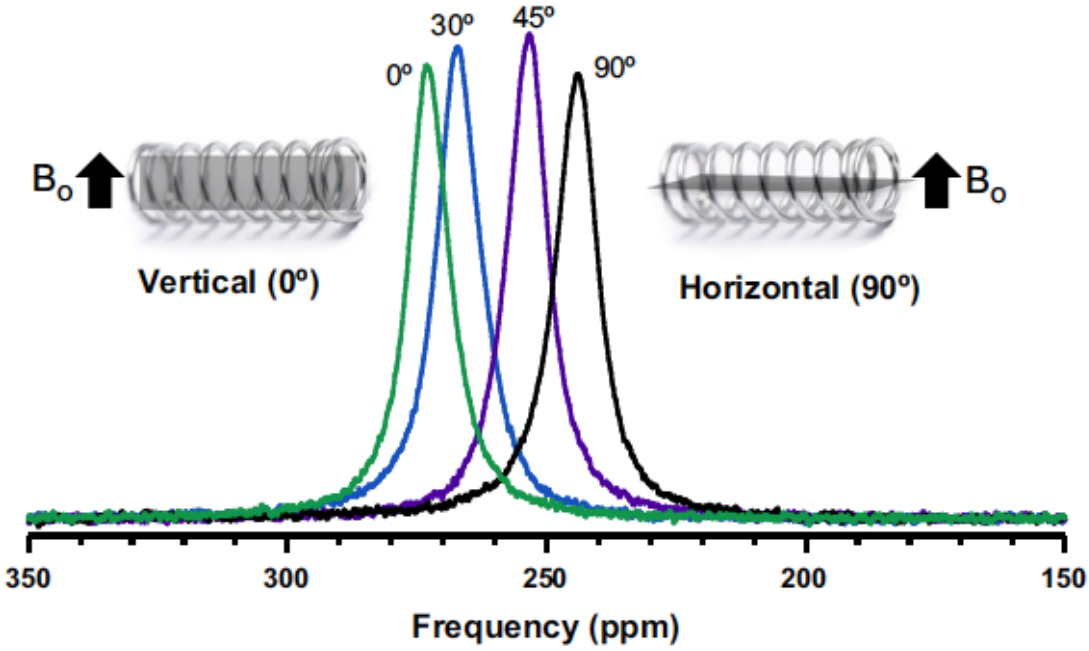

Figure 1.9 Bulk magnetic susceptibility effect on the ^{7}Li shift of lithium metal. Spectra are given for lithium metal strips (4 mm x 10 mm x 0.38 mm), with their short axes oriented at approximately 0° (vertical), 30°, 45°, and 90° (horizontal) with respect to B_0, at shifts of 272, 267, 254, and 244 ppm, respectively. The schematic shows the orientation of the lithium metal strip in the NMR coil at 0° (vertical) and 90° (horizontal) with respect to B_0. Spectra were acquired at 77.5 MHz (4.7 T).

Skin-depth is a measure of the ability of the radio frequency (rf) pulse to penetrate into the metal.[34, 55] It is a function of known physical constants, properties inherent to the metal and the frequency of the rf pulse. The skin depth, d, can be readily calculated using Equation 1.5, where μ_0 is the permeability of the vacuum (= 4π x 10^{-7} m kg/A^{2}s^2), μ_r is the relative permeability of the metal (for Li, μ_r = 1.00002), ρ is the resistivity of the metal (for Li, ρ = 92.8 nΩ m), and f is the frequency of applied radiofrequency (77.5 MHz for ^{7}Li, 28.9 MHz for ^{6}Li).

$$d = \frac{1}{\sqrt{\pi \mu_0}} \sqrt{\frac{\rho}{\mu_r f}} \tag{1.5}$$

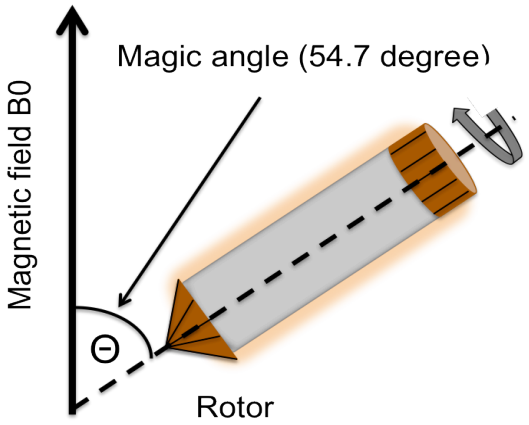

Figure 1.10 Schematic representation of the MAS technique where Θ is the angle between the rotor and the external magnetic field.

In this study, the skin depth (17.4 μm for ^{7}Li, 28.5 μm for ^{6}Li) is much larger than the reported thickness of dendritic or mossy whiskers of 1~2 μm[33], thus the penetration of microstructures is assumed to be total and used to calculate the mass of microstructures.

1.4.4 Static versus MAS solid-state NMR

In liquid state NMR, typically the molecular motion leads to isotropic spectra. Unlike liquids, in solid-state NMR, spectra are broadened due to the orientation dependence of the different crystallites with the magnetic field and the presence of anisotropic interactions. Magic-Angle Spinning (MAS) is a technique often used to perform experiments in solid-state NMR spectroscopy. By spinning the sample at high speeds at the magic angle (Θ of 54.736^{o}, Figure 1.10) with respect to the external magnetic field, anisotropic components of interactions such as chemical shielding, heteronuclear dipolar coupling and first order quadrupolar coupling are removed. Slower MAS spinning speeds result in an isotropic resonance flanked by spinning sidebands that occur at multiples of the spinning frequency.

Static *in situ* NMR spectroscopy has been used to obtain real-time local structural changes while cycling batteries. It has the great advantage of performing feasible, quantitative and non-invasive experiments to study changes in LIBs. The first *in situ* experiments of batteries were

performed by Gerald *et al.*[56] for both NMR and for MRI with a toroid cavity. However, poor signal-to-noise was obtained with the toroid design and a different battery design was required to study LIBs. Letellier *et al.*[57] improved the *in situ* NMR design, performing experiments using Bellcore[58] plastic bag technology. Plastic batteries have the advantage that they can be used in a conventional static probe, without the need to apply external compression to the battery in lieu of the specialized probe with toroid cavity, used by Gerald *et al*.[56].

1.5 MRI

In 1977, the first magnetic resonance imaging (MRI) machine was introduced into medical settings to produce high quality images of the inside of the human body (Figure 1.11). The technique was intentionally called magnetic resonance imaging rather than nuclear magnetic resonance imaging (NMRI) because of the negative connotations associated with the word nuclear. Magnetic resonance imaging has been popular with radiologists and remarkable technological advances have been achieved providing better spatial resolution, the ability to identify a small and dense object with contrast resolution, visualization of an object with similar characteristics (soft tissues).

Recently, the use of MRI as a diagnostic tool extends to material science field. The ealier studies of MRI of Li batteries have been very sparse, and limited to either imaging the electrolyte only[59], or visualizing ^{7}Li signals from specifically constructed cells that allow for spatial resolution via radiofrequency (rf) field gradients.[60] In 2012, our team first demonstrated two- and three-dimensional ^{7}Li MRI and chemical shift imaging (CSI) of batteries, particularly symmetric Li metal cells, with full control over resolution and imaging axes.[35] The more details of our work will be introduced in the following section 1.6 (MRI application).

Figure 1.11 An example MRI scan of human brain.

1.5.1 Magnetic field gradient and dimensionality

The MRI is basically based on the principles of NMR. The difference of MRI from the NMR is the extra electromagnets called "gradient coils". Three magnetic field gradients ($\mathbf{G_x}$, $\mathbf{G_y}$, $\mathbf{G_z}$) can be produced by three sets of gradient coils around the $\mathbf{B_0}$ field, with its longitudinal axis orientated in the z direction, and then by passing a direct current through the coils. The magnetic field generated from the G_z coil pair adds to the B_0 field, with the result that one end of the magnet has higher field strength than the other. The gradient coils can be used to produce deliberate variations in $\mathbf{B_0}$ to provide spatial dimensionality of the objects measured. The variation in the main magnetic field with respect to position permits a 2- and 3- dimensional image to be generated by one or two phase encoded dimensions, respectively, and a frequency encoded dimension. Three-dimensional images can also be obtained using slice selection. The symbols for the magnetic field gradients in the x, y and z direction can be written as G_x, G_y, and G_z shown in Figure 1.12.[61]

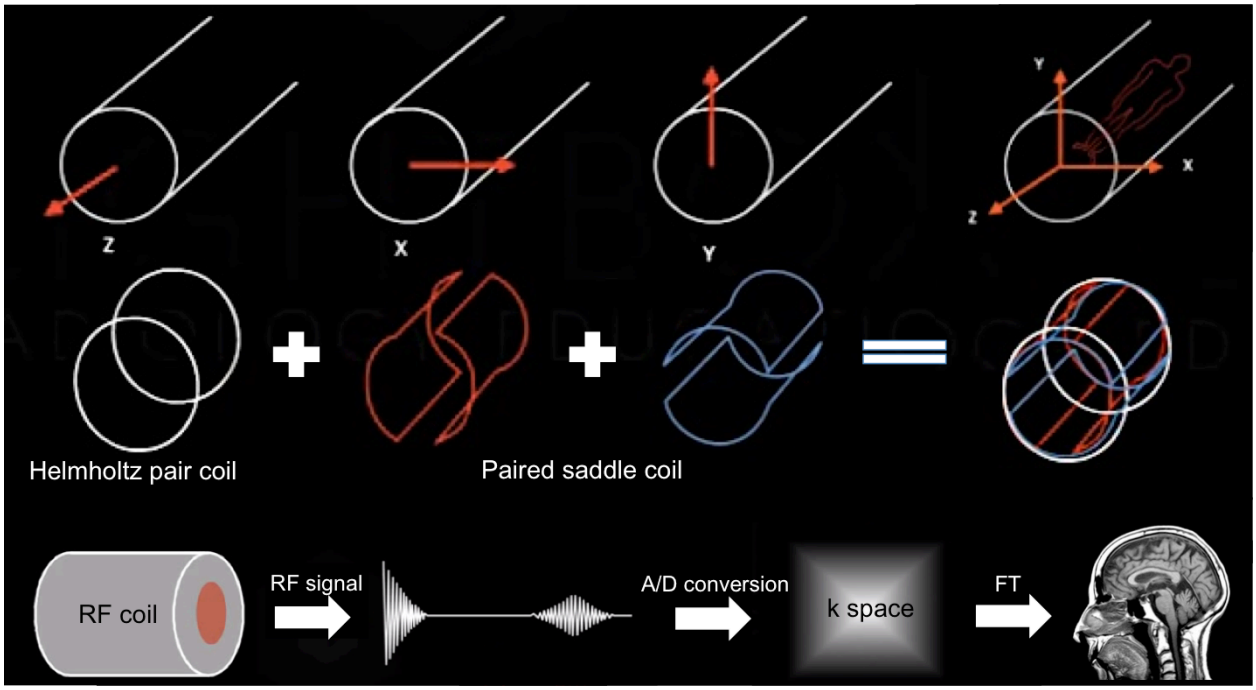

Figure 1.12 The configuration of gradient coils, indicates the magnetic field gradient in the x, y, and z directions and the processing of MRI image. (The Figure is adapted from reference 61.)

1.5.2 Frequency Encoding

Frequency-encoding is a direct detection method and has the effect of spatially encoding the excited slice along the gradient direction, so that columns of spins perpendicular to the gradient, G_x, axis precess at slightly different Larmor frequencies of $\omega_0(x) = \gamma \mathbf{B}_0 + \gamma x G_x$ at position x. Recall from the NMR introduction and the previous section, that γ is the gyromagnetic ratio and G_x is a magnetic field gradient in the x direction. Each frequency is related to the corresponding spatial location along the direction of the gradient and the spectrum provides a projection of the object being imaged.

A frequency-encoding gradient (G_x) is turned on just before the receiver is gated on and is left on while the signal is acquired or read out. For this reason the particular use of the frequency-encoding gradient is also known as the readout gradient and the direction of the

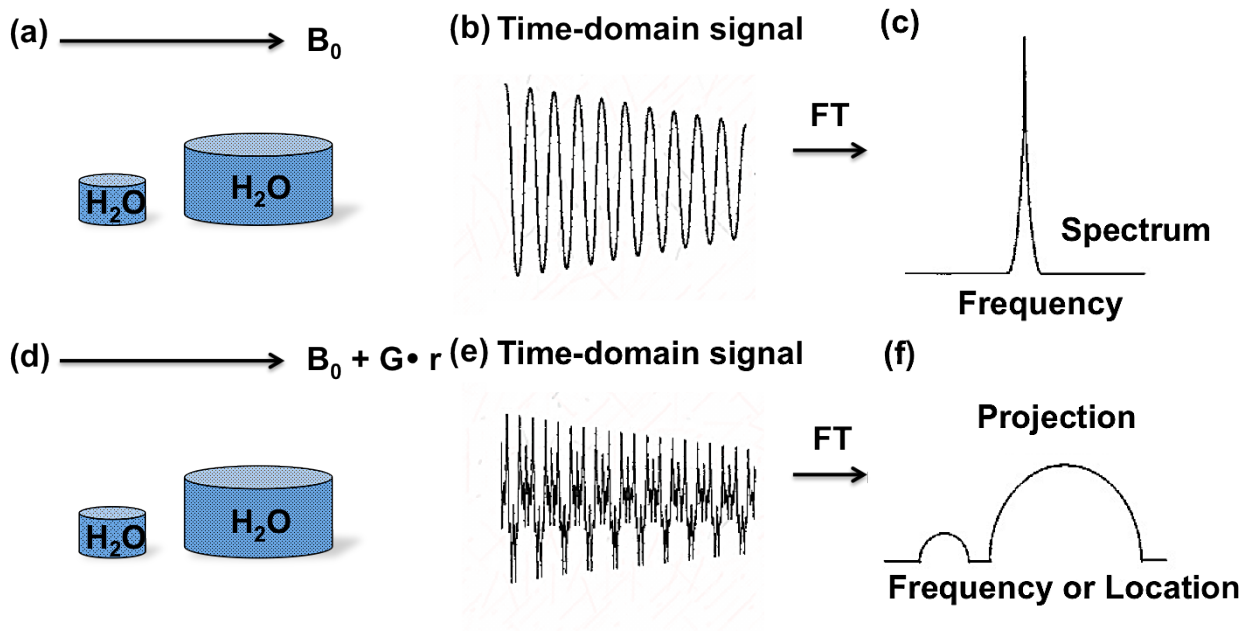

Figure 1.13 Two FIDs and their Fourier transforms. NMR signal for two plates of water in the absence (top row) and presence (bottom row) of a frequency encoding gradient, r the spatial location along the gradient direction and FT the Fourier transform. (a~c) without the gradient and (d~f) with the gradient. In the presence of the gradient, a spectrum after FT (f) shows spatial information regarding the two water plates. (The Figure is adapted from 62).

gradient is called the readout direction. Figure 1.13[62] shows the effect of a frequency-encoding gradient on an object consisting of water in two different plates. In the absence of an applied gradient, the NMR signal (free-induction decay (FID)) contains a single frequency in the time domain. After the Fourier transform of the FID, a conventional NMR spectrum in which the signal amplitude is plotted as a function of frequency can be obtained consisting of a single resonance (Figure 1.13a,b,c). If a frequency-encoding gradient is then applied to the same object (horizontal direction, r_x in Figure 1.13d,e,f), the two regions experience different magnetic field strengths resulting in a FID containing multiple frequencies in the time-domain. Due to the spatial dependence of the frequency, the frequency axis can be converted to distance. The amplitude of the signal is proportional to the number of spins in the plane perpendicular to the gradient. Therefore, a frequency-encoding gradient produces a projection of the object with the spatial information encoded in the NMR signal.

1.5.3 Phase Encoding

The idea of phase encoding is to create a linear spatial localization in MRI, as is done for frequency-encoding. It is typically used to spatially encode information orthogonal (G_y or G_z) to the frequency-encoded direction (G_x), as shown in Figure 1.14[63]. For example, in the absence of the phase encoding gradient, spins at A and B precess at the same resonance frequency ($\omega_0 = \gamma \mathbf{B_0}$). When the gradient pulse is turned on along the direction of y axis, spins at A and B start to precess at different frequencies and over the time period τ a spin at location y will gain a phase shift of $\Delta\phi = \tau\Delta\omega(y) = \gamma\tau G_y y$ compared to the reference spins at y=0. The combination of the signal from A and B results in an averaged phase shift of ½ ($\phi_A+\phi_B$) in a sine wave of the same base frequency. The magnetization vectors in space will form a helical shape along the y-axis. After the gradient is turned off, the helix shape remains since the spins return to an identical precession frequency. In practice, individual phase contribution from A or B cannot be determined from a single measurement, therefore multiple phase encoding steps are required to gain spatial information in the phase encoding direction.

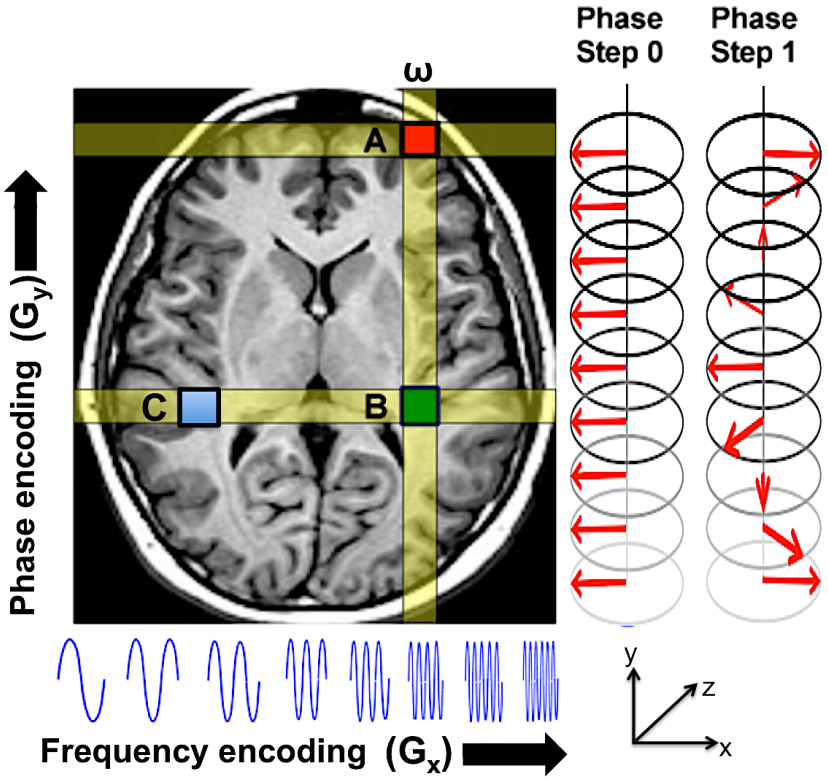

Figure 1.14 An illustrated example of phase encoding steps and frequency encoding. Consider 3 pixels, A (red square), B (green square), and C (blue square) in an image. A and B lie along the same frequency-encoding column with different gradient-induced phase shift. B and C resonate at the different frequencies. Frequency encoding cannot distinguish between pixels within column A and B hence phase encoding method is required for spatial detection. (The Figure is adapted from reference 63.)

1.5.4 Slice Selection

Slice selection is achieved by applying a linear magnetic field gradient to the entire sample during the period that a selective rf pulse is applied (Figure 1.15[64]). A slice selection gradient G_z in the z direction is used to excite a slice of spins in the xy plane at the resonance frequency of $\omega_0(z) = \gamma \mathbf{B}_0 + \gamma z G_z$. Only a narrow plane (slice) perpendicular to the longitudinal axis at the center of the sample will be excited by the rf pulse. Everywhere else in the sample is receiving the wrong frequency of excitation for resonance to occur and the range of frequencies of excitation incorporated in the rf pulse is important to determine the shape of the slice profile.

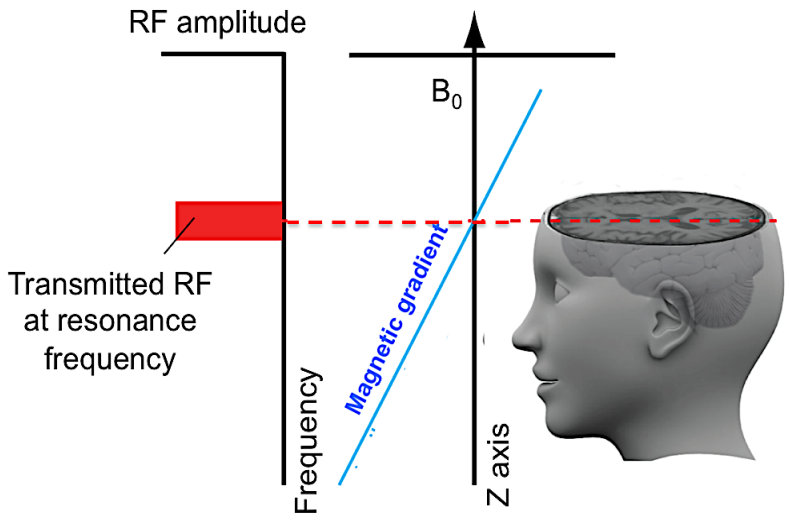

Figure 1.15 Illustration of slice selection during the rf excitation phase using a longitudinal magnetic field gradient. (The Figure is adapted from reference 64.)

This technique allows a slice, with thickness determined by the magnetic field gradient strength, to be selected from a sample.

1.5.5 Chemical Shift Imaging

Chemical shift imaging (CSI) combines the spatial information of MRI with the chemical speciation of NMR. The chemical shift dimension is the typically the direct dimension, the image is obtained only using phase-encoded gradients.

1.6 MRI applications for Li metal anodes

In 2012, we demonstrated the two different types of Li microstructures (moss and dendrite) formed on the Li metal surface using ^{7}Li MRI images and chemical shift imaging (CSI).[35] The work has further shown that challenges due to the orientation-dependent rf penetration of the electrodes can be overcome. In our MRI project, my contributions have been to prepare samples and carry out the experiments.

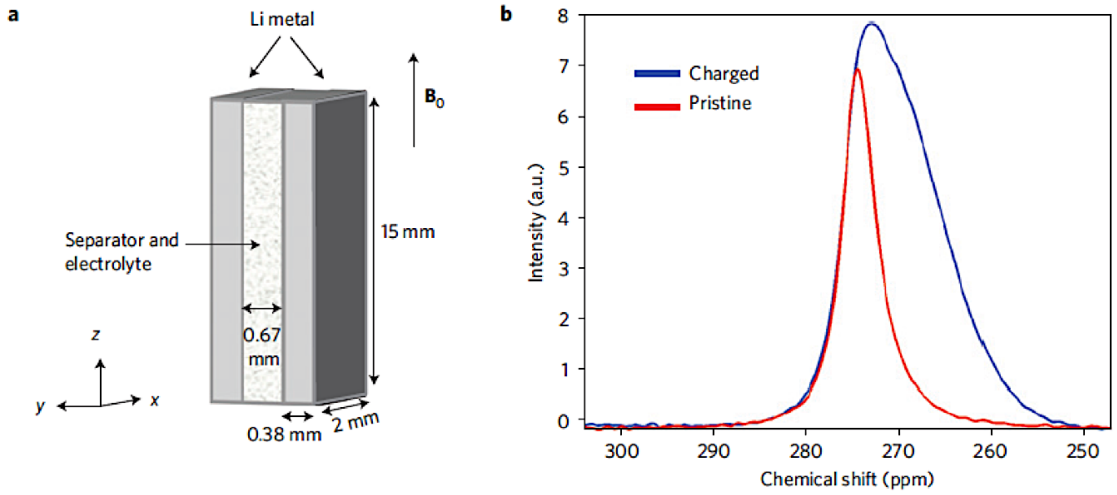

Figure 1.16 Schematic representations of a bag-cell battery and one-dimensional 7Li NMR spectra in the pristine and charged states. (a) Schematic representation of the bag-cell battery, and its orientation with respect to the static magnetic field in the NMR spectrometer. The x, y and z axes correspond to the gradient axes of the triple-axis gradient probe and the z axis also corresponds to the direction of the static magnetic field $\mathbf{B}_0$. (b) Comparison of the ^{7}Li NMR spectra of the Li-metal resonance from a symmetric Li-metal bag cell before (pristine) and after applying a current (charged). The area under the spectrum of the charged state is 2.3 times larger than that of the pristine state.

Investigation of Li electrodes in a symmetric cell was carried out in their pristine, and subsequently charged states. The images reveal the location of the Li microstructures on or in the vicinity of the negative electrode. The microstructures are characterized by a significant increase in the intensity of the ^{7}Li signal, and the observation of distinct susceptibility shifts that are characteristic of different microstructures. Thus, a compelling demonstration of the use of MRI to report nondestructively on processes that occur inside a battery, and in particular on the electrodes, was presented.

Figure 1.16b compares the 1D NMR spectra of the cell, obtained in the optimum arrangement of the cell where the long axis of the Li metal strips are parallel to $\mathbf{B}_0$ and the $\mathbf{B}_1$ field is perpendicular to ion flow, before and after passing a single current density of 29 A/m^2 for 4 hours. Substantial amounts of Li microstructure are formed, as confirmed by the difference in signal integral between the spectra before and after charging. This difference arises from the fact that microstructures are unaffected by the skin depth effect and therefore add to the signal in

proportion to the amount of Li. Since the surface area and skin depth are known, the new signal can be quantified by normalizing it to the signal obtained from the skin-depth of the bulk metal material before charging, and the amount of accumulated microstructural Li can be determined.

The calculation of the amount of deposited microstructure yielded a value of 0.89 mg. The total amount of Li deposited, as calculated from the electrochemical measurements and assuming 100% Columbic efficiency is 0.91 mg, which is in very good agreement with the amount determined by NMR. The substantial new signal observed in the charged battery spectrum exhibits a resonance that continuously extends from the pristine metal resonance (with a Knight shift of approximately 274 ppm) up to approximately 10 ppm upfield and can therefore be attributed to dendritic, mossy and other microstructural metallic Li formed upon charging. These upfield shifts arise from bulk magnetic susceptibility effects caused by the metal electrodes.

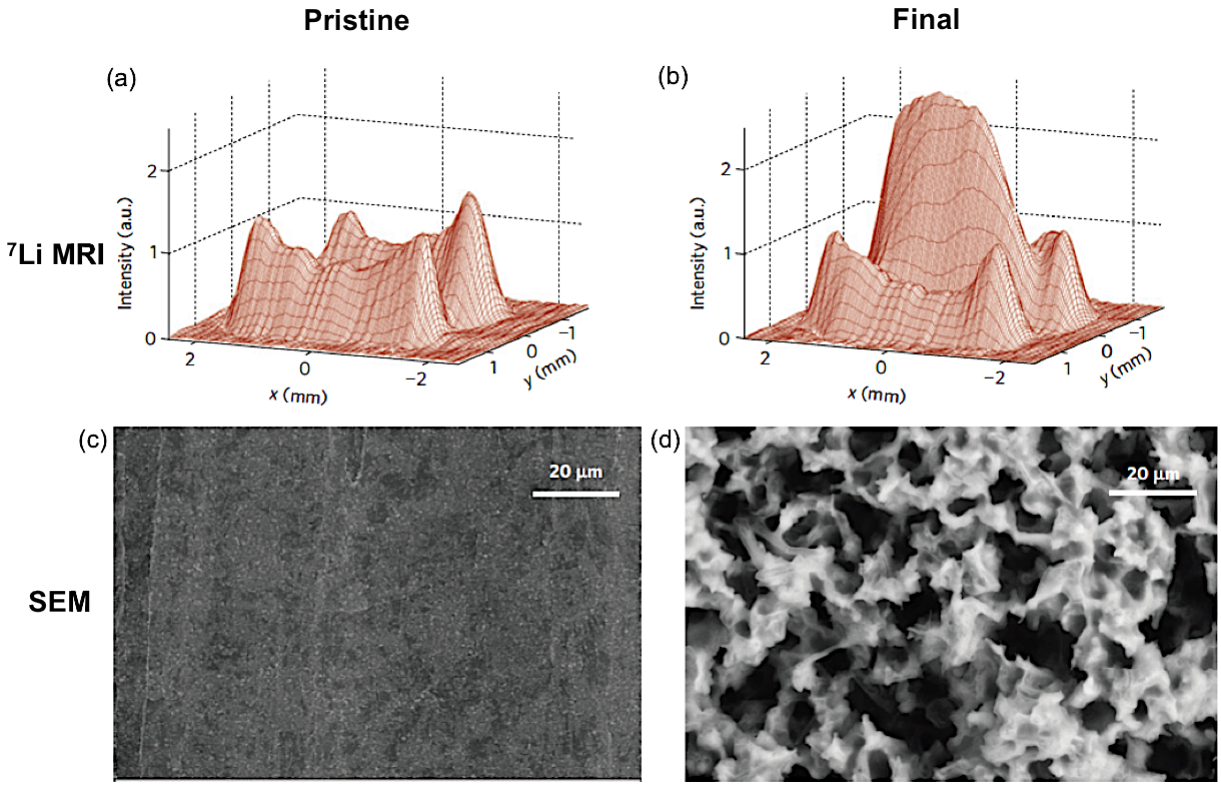

Figure 1.17 ^{7}Li 2D MRI *x*-*y* image (frequency encoding in *x*, phase encoding in *y*) (a) in the pristine state, and (b) after passing current ("charging"). SEM images (c) in the pristine state, and (d) after charging. The spatial directions, as they relate to the orientation of the cell, are depicted in Figure 1.16a.

Figures 1.17a and 1.17b show two-dimensional ^{7}Li MRI images before and after charging the battery, respectively, which show the cumulative signal projected along the *z* direction. Based on the imaging parameters, a resolution of 60 µm x 376 µm was achieved in the *x* and *y* directions, respectively. The image of the charged battery reveals a significant buildup of signal at the negative electrode (~ a factor of 2), indicating the location of microstructural Li. It is also seen that the positive electrode has a decreased signal (-23%) after charging. The SEM images of Figures 1.17c and 1.17d are consistent with the above MRI findings, likewise illustrating the buildup of significant lithium microstructure on the negative electrode after charging. A discernible, and as yet not fully understood, feature in these images is that the electrode signals increase towards the edges of the electrodes. It is possible that this effect is due to slight

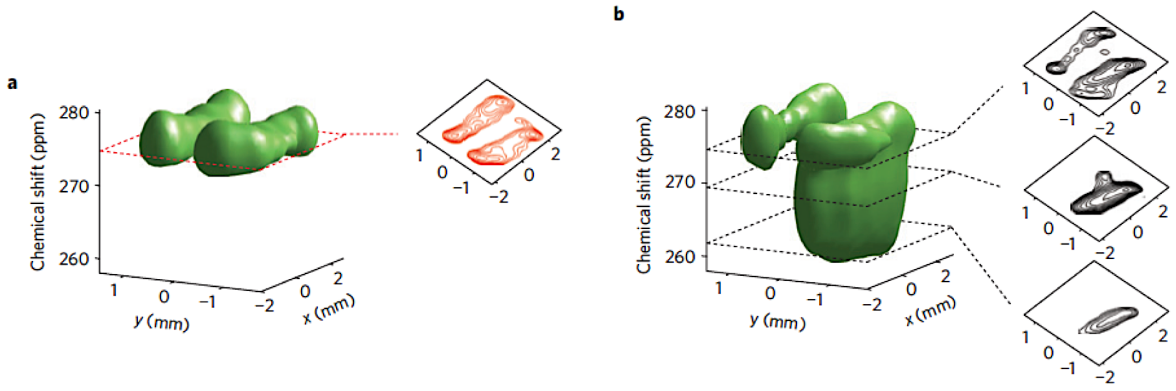

Figure 1.18. ^{7}Li Chemical Shift Image (CSI) of the Li metal resonance in a symmetric Li metal bag cell (phase encoding in *x* and *y*, chemical shift encoding in the directly observed dimension) (a) in the pristine state, and (b) after charging.

misalignment between the electrodes and the rf field orientation, partly enhanced by possible field distortions caused by the proximity of two metal strips.[55]

Figure 1.18 shows CSI images before and after cycling. New signals appear after "charging" the cell (Figures 1.16b) with shifts of < 274 ppm that can be assigned to the newly formed Li microstructures. The relationships between the sizes of the susceptibility induced shifts and the relative orientations and distances of the microstructures from the bulk metal anode are clearly revealed in the CSI images. Microstructures in the vicinity of the electrodes are shifted significantly and span a large frequency range from 274 to more than 262 ppm. Dendrites, furthest removed from the negative electrode, show smaller susceptibility shifts (Figure 1.18b). For example, in Figure 1.18b the 2D image taken from a slice at 269.6 ppm clearly shows a dendrite extending into the space between the electrodes. It is this form of microstructure buildup, which grows into the space between the electrodes and penetrates the separator, which is likely to result in the eventual short-circuiting of the battery.

1.7 X-ray tomography

1.7.1 General Background

The X-ray tomographic method is the most common form of computerized tomography (CT) and was first commercially introduced by Hounsfield and Ambrose for medical use in 1972. It is a nondestructive technique for visualizing interior features in objects and for obtaining their 3D geometric information and properties. The common mechanism of the conventional X-ray tomographic methods is X-ray absorption by the sample in contrast imaging formation. In addition to the absorption mechanism, phase-contrast methods, or refractive imaging methods were developed to create images by use of the refraction of X-rays. These types of methods enable the visualization of objects that barely absorb X-rays as well as enhancement of the visibility of weakly absorbing features in more strongly absorbing object components.

When X-rays pass through an object, the beam interacts with the object and carries structural information about the object (Figure 1.19). The dominant interactions between the object and X-ray beam are photoelectric absorption and scattering, which can be modified by beam intensity and direction. Typically, three different X-ray tomographic configurations are achieved using either a cone beam (lab source), planar fan beam or a parallel beam (synchrotron). While X-ray radiography measures images for a single orientation of the sample, tomography measures images for many different angular positions. This results in a set of projections, which can be used to reconstruct two-dimensional slices through the object. By stacking these slices together, the structure of the sample can be visualized in three dimensions.

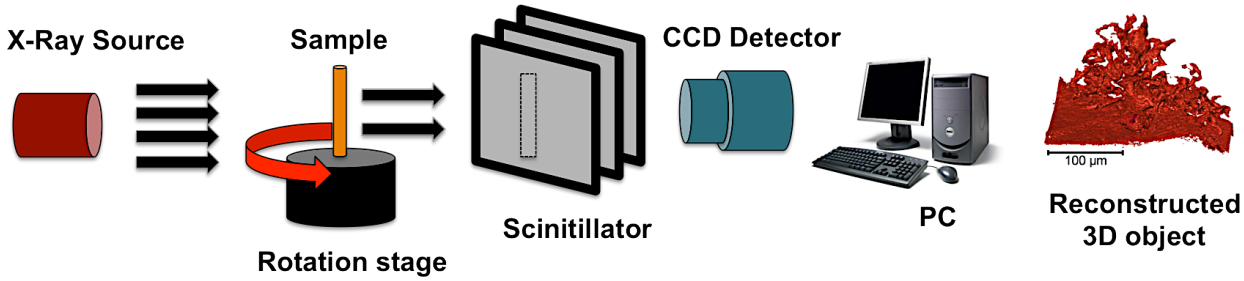

Figure 1.19 Schematic view of X-ray computed tomography system

Synchrotron X-ray tomography is based on the detection of either the attenuation or the phase shift of the beam transmitted through a sample. The advantages of using synchrotron X-ray beams are a very high intensity of the source with a high signal-to-noise ratio on short time-scales, which enables fast radiographic investigations for visualizing images.

1.7.2 X-ray tomography application for Li metal anode

In 2014 we used non-destructive X-ray tomography to perform *in situ* examination of Li microstructures in 3D at high resolution. The technique using a synchrotron beam (Diamond-Manchester Branchline I13I at Diamond Light Source) is applied to bespoke electrochemical cells designed to enable lithium electrodeposition with an unobstructed X-ray path under a 360° rotation.[65] My contribution to this project was preparation of samples and analyzing the data.

Symmetrical cells used lithium metal (Aldrich, 99.9%) electrodes formed around copper wire in 1 mm inner diameter Kapton capillaries. Since lithium is the least dense elemental solid (under standard laboratory conditions) the X-ray contrast is very weak when using conventional laboratory X-ray tubes. Hence, synchrotron radiation sources were used to deliver high flux monochromatic X-ray beam at low energies, optimizing contrast between lithium and the surrounding electrolyte and cell components. The beam was monochromated to 19 keV with a bandwidth of 0.1 eV, enabling in-line phase contrast imaging, where attenuation and refractive effects are decoupled to image interfaces between materials of similar attenuation. Synchrotron in-line phase contrast X-ray imaging was used to characterize different formations of Li microstructures in lithium electrochemical cells.

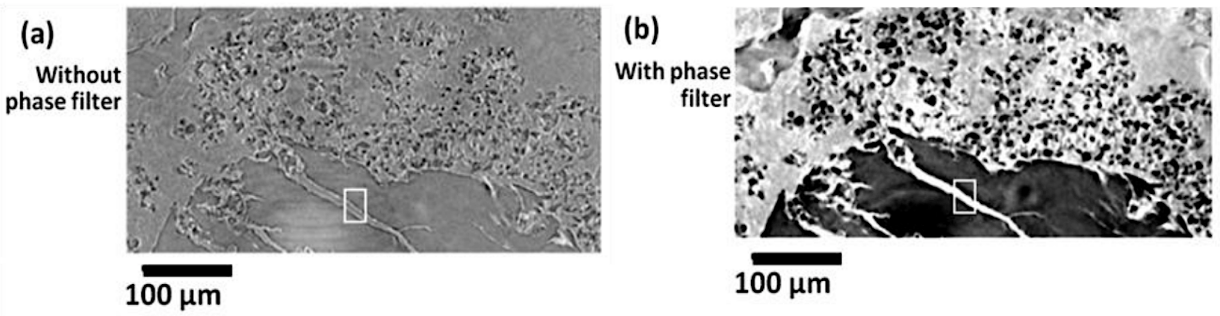

Figure 1.20 A vertical slice through the reconstructed tomographic image of mossy structures formed on metallic lithium metal during constant current, shown (a) without phase backpropagation filtering, (b) after applying a phase backpropagation filter.

The high-resolution 3D X-ray images of a lithium moss formed under constant current are shown in Figure 1.20. Figure 1.20a shows a longitudinal slice through the reconstructed 3D data set with and without application of a phase backpropagation filter that minimizes the bright and dark fringes at material boundaries and, making segmentation of the lithium and electrolyte possible by thresholding the grayscale value. In Figure 1.20b the X-ray projections have been processed using a phase backpropagation filter prior to tomographic reconstruction. The dark region at the base of the image is the low-attenuation bulk lithium metal electrode containing folds formed during cell construction, and the smaller features above with the same grayscale values are mossy metallic lithium, which has electrodeposited on the electrode. The surrounding light grey regions are electrolyte and solvent.

Figure 1.21 provides a comparison of the microstructures formed under constant current (Figure 1.21a and b) and cycled current (Figure 1.21c and d). The full 3D complexity of these different Li microstructures, and their interaction with the bulk lithium electrode, is revealed in the 3D renderings in Figs. 3b and 3d. Comparison of 2D slices (Figure 1.21a and c) reveal differences in both morphology and composition of the dendrites formed under different constant and cycled currents.

Consequently, synchrotron in-line phase contrast X-ray imaging was used to characterize different formations of Li microstructures in lithium electrochemical cells. The improved spatial

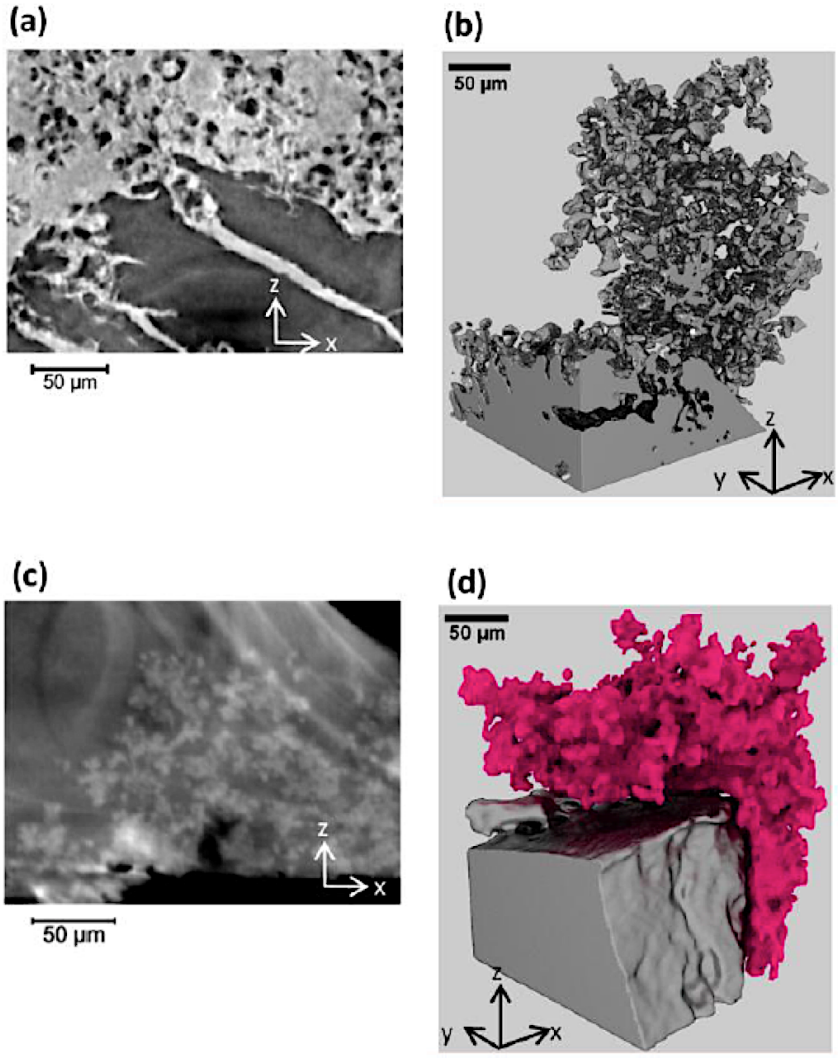

Figure 1.21. Lithium microstructures formed during galvanostatic cycling. (a) 2D slice through metallic lithium microstructures formed under constant current, (b) 3D rendering of the metallic lithium microstructure formed under constant current, (c) 2D slice through higher density microstructures formed under cycled currents, and (d) 3D rendering of the microstructures formed under cycled current.

resolution and density differentiation presented here enables, for the first time, the ability to discriminate between dendrite morphologies and compositions, namely metallic lithium and electrolyte.

1.8 References

1. C. Brissot, M. Rosso, J.-N. Chazalviel and S. Lascaud, *J. Electrochem. Soc.*, 1999, **146**, 4393-4400.
2. J. M. Tarascon and M. Armand, *Nature*, 2001, **414**, 359-367.
3. D. Aurbach, Y. Gofer and J. Langzam, *J. Electrochem. Soc.*, 1989, **136**, 3198-3205.
4. E. Peled, *J. Electrochem. Soc.*, 1979, **126**, 2047-2051.
5. D. Aurbach, I. Weissman, H. Yamin and E. Elster, *J. Electrochem. Soc.*, 1998, **145**, 1421-1426.
6. J. B. Goodenough and Y. Kim, *Chem. Mater.*, 2010, **22**, 587-603.
7. J. B. Bates, *United states patent 5314765*, 1994.
8. P. Arora and Z. M. Zhang, *Chem. Rev.*, 2004, **104**, 4419-4462.
9. P. C. Howlett, D. R. MacFarlane and A. F. Hollenkamp, *Electrochem. Solid-State Lett.*, 2004, **7**, A97-A101.
10. X. W. Zhang, Y. X. Li, S. A. Khan and P. S. Fedkiw, *J. Electrochem. Soc.*, 2004, **151**, A1257-A1263.
11. T. Tatsuma, M. Taguchi, M. Iwaku, T. Sotomura and N. Oyama, *J. Electroanal. Chem.*, 1999, **472**, 142-146.
12. M. Armand and J. M. Tarascon, *Nature*, 2008, **451**, 652-657.
13. M. S. Whittingham, *Proc. IEEE*, 2012 **100**, 1518-1534.
14. M. R. Palacin, *Chem. Soc. Rev.*, 2009, **38**, 2565-2575.
15. C. M. Park, J. H. Kim, H. Kim and H. J. Sohn, *Chem. Soc. Rev.*, 2010, **39**, 3115-3141.
16. N.-m. h. b. Wiki: Lead-acid battery.
17. S. Megahed and B. Scrosati, *J. Power Sources*, 1994, **51**, 79-104.
18. T. Hirai, I. Yoshimatsu and J. Yamaki, *J. Electrochem. Soc.*, 1994, **141**, 611-614.
19. S. I. Tobishima, K. Hayashi, Y. Nemoto and J. I. Yamaki, *Electrochim. Acta*, 1998, **43**, 925-933.
20. M. K. Yuichi Sato, Hirokazu Niki, Mitsushi Ueno, Kenji Murata, Tamotsu Shirogami, Tsutomu Takamura, *J. Power Sources*, 1983, **9**, 147-159.
21. D. Aurbach, E. Zinigrad, Y. Cohen and H. Teller, *Solid State Ionics*, 2002, **148**, 405-416.
22. Y. S. Cohen, Y. Cohen and D. Aurbach, *J. Phys. Chem. B*, 2000, **104**, 12282-12291.
23. S. Shiraishi, K. Kanamura and Z. Takehara, *J. Phys. Chem. B*, 2001, **105**, 123-134.
24. K. Kanamura, S. Shiraishi and Z. Takehara, *J. Electrochem. Soc.*, 1996, **143**, 2187-2197.

25. X. H. Liu, L. Zhong, L. Q. Zhang, A. Kushima, S. X. Mao, J. Li, Z. Z. Ye, J. P. Sullivan and J. Y. Huang, *Appl. Phys. Lett.*, 2011, **98**.

26. F. Orsini, A. Du Pasquier, B. Beaudoin, J. M. Tarascon, M. Trentin, N. Langenhuizen, E. De Beer and P. Notten, *J. Power Sources*, 1998, **76**, 19-29.

27. C. M. Lopez, J. T. Vaughey and D. W. Dees, *J. Electrochem. Soc.*, 2009, **156**, A726-A729.

28. R. E. Hoffman, *J. Magn. Reson.*, 2006, **178**, 237-247.

29. I. Epelboin, M. Froment, M. Garreau, J. Thevenin and D. Warin, *J. Electrochem. Soc.*, 1980, **127**, 2100-2104.

30. M. Arakawa, S. Tobishima, Y. Nemoto, M. Ichimura and J. Yamaki, *J. Power Sources*, 1993, **43**, 27-35.

31. S. H. Bo, F. Wang, Y. Janssen, D. L. Zeng, K. W. Nam, W. Q. Xu, L. S. Du, J. Graetz, X. Q. Yang, Y. M. Zhu, J. B. Parise, C. P. Grey and P. G. Khalifah, *J. Mater. Chem.*, 2012, **22**, 8799-8809.

32. B. Key, M. Morcrette, J. M. Tarascon and C. P. Grey, *J. Am. Chem. Soc.*, 2011, **133**, 503-512.

33. C. P. Grey and Y. J. Lee, *Solid State Sci.*, 2003, **5**, 883-894.

34. R. Bhattacharyya, B. Key, H. Chen, A. S. Best, A. F. Hollenkamp and C. P. Grey, *Nat. Mater.*, 2010, **9**, 504-510.

35. S. Chandrashekar, N. M. Trease, H. J. Chang, L.-S. Du, C. P. Grey and A. Jerschow, *Nat. Mater.*, 2012, **11**, 311-315.

36. N. Schweikert, A. Hofmann, M. Schulz, M. Scheuermann, S. T. Boles, T. Hanemann, H. Hahn and S. Indris, *J. Power Sources*, 2013, **228**, 237-243.

37. J. Wandt, C. Marino, P. Jakes, R. Eichel, H. A. Gasteiger and J. Granwehr, *Energy Environ. Sci.*, 2015.

38. M. Sathiya, J. B. Leriche, E. Salager, D. Gourier, J. M. Tarascon and H. Vezin, *Nat. Commun.*, 2015, **6**, 6276.

39. C. Kittel, *Introduction to Solid State Physics*, New York: Wiley, 1976.

40. J. W. Diggle, A. R. Despic and J. O. M. Bockris, *J. Electrochem. Soc.*, 1969, **116**, 1503-1514.

41. T. Witten and L. Sander, *Phys. Rev. Lett.*, 1981, **47**, 1400-1403.

42. J.-N. Chazalviel, *Phys. Rev. A*, 1990, **A 42**.

43. C. Brissot, M. Rosso, J.-N. Chazalviel, P. Baudry and S. Lascaud, *Electrochim. Acta*, 1998, **43**, 1569.

44. J. Yamaki, S. Tobishima, K. Hayashi, K. Saito, Y. Nemoto and M. Arakawa, *J. Power Sources*, 1998, **74**, 219-227.

45. R. V. Magan and R. Sureshkumar, *J. Phys. Chem. B*, 2003, **107**, 10513-10520.

46. M. Z. Mayers, J. W. Kaminski and T. F. Miller, *J. Phys. Chem. C*, 2012, **116**, 26214-26221.

47. P. Meakin, *Phy. Rev. Lett.*, 1983, **51**, 1119.

48. R. F. Voss and M. Tomikiewicz, *J. Electrochem. Soc.*, 1985, **132**, 371-375.

49. C. Brissot, M. Rosso, J. N. Chazalviel and S. Lascaud, *J. Power Sources*, 2001, **94**, 212-218.

50. J. K. Stark, Y. Ding and P. A. Kohl, *J. Electrochem. Soc.*, 2013, **160**, D337-D342.

51. R. K. Harris, E. D. Becker, S. M. C. De Menezes, P. Granger, R. E. Hoffman and K. W. Zilm, *Solid State Nucl. Magn. Reson.*, 2008, **33**, 41-56.

52. C. P. Slichter, *Principles of Magnetic Resonance*, Springer-Verlag, 1990.

53. N. M. Trease, L. Zhou, H. J. Chang, B. Y. Zhu and C. P. Grey, *Solid State Nucl. Magn. Reson.*, 2012, **42**, 62-70.

54. A. Kubo, T. P. Spaniol and T. Terao, *J. Magn. Reson.*, 1998, **133**, 330-340.

55. A. J. Ilott, S. Chandrashekar, A. Klockner, H. J. Chang, N. M. Trease, C. P. Grey, L. Greengard and A. Jerschow, *J. Magn. Reson.*, 2014, **245**, 143-149.

56. R.E. Gerald II, R. J. Klingler, G. S.́ı, C. S. Johnson, L. G. Scanlon and J. W. Rathke, *J. Power Sources*, 2000, **89**, 237-243.

57. M. Letellier, F. Chevallier and M. Morcrette, *Carbon*, 2007, **45**, 1025-1034.

58. J.M.Tarascon, A.S.Gozdz, C.Schmutz, F.Shokoohi and P.C.Warren, *Solid state Ionics*, 1996, **86**, 49-54.

59. J. Kawamura and Y. Iwai, *Tohoku Univ Takes MRI Images of Li-ion Battery*. http://techon.nikkeibp.co.jp/english/NEWS_EN/20090709/172827/ 2009.

60. R. E. Gerald, R. J. Klingler, G. Sandi, C. S. Johnson, L. G. Scanlon and J. W. Rathke, *J. Power Sources*, 2000, **89**, 237-243.

61. lightboxradiology.com.au., May 2015.

62. M. A. Bernstein, K. F. King and X. J. Zhou, *Elsevier*, 2004.

63. http://mri-q.com/what-is-phase-encoding.html, May 2015.

64. http://neurosurgerysurvivalguide.com/roundy/, May 2015.

65. D.S Eastwood, P. M Bayley, H. J. Chang, O. O. Taiwo, J. Vila-Comamala, D. JL. Brett, C. Rau, P. J. Withers, P. R. Shearing, C. P. Grey and P. D. Lee, *Chem. Comm.*, 2015, **51**, 266-268.

Chapter 2

Investigating Li Microstructure Formation on Li Anodes for Lithium Batteries by *In Situ* ^{6}Li/^{7}Li NMR and SEM

Abstract

The growth of lithium microstructures during battery cycling has, to date, prohibited the use of Li metal anodes and raises serious safety concerns even in conventional lithium-ion rechargeable batteries, particularly if they are charged at high rates. The electrochemical conditions under which these Li microstructures grow have, therefore, been investigated by *in situ* nuclear magnetic resonance (NMR), scanning electron microscopy (SEM) and susceptibility calculations. Lithium metal symmetric bag cells containing $LiPF_6$ in EC: DMC electrolytes were used. Distinct ^{7}Li NMR resonances were observed due to the Li metal bulk electrodes and microstructures, the changes in peak positions and intensities being monitored *in situ* during Li deposition. The changes in the NMR spectra, observed as a function of separator thickness and porosity (using Celgard and Whatmann glass microfiber membranes) and different applied pressures, were correlated with changes in the type of microstructure, by using SEM. Isotopically enriched ^{6}Li metal electrodes were used against natural abundance predominantly ^{7}Li metal counter electrodes to investigate radiofrequency (rf) field penetration into the Li anode and to confirm the assignment of the higher frequency peak to Li dendrites. The conclusions were supported by calculations performed to explore the effect of the different microstructures on peak position/broadening, the study showing that Li NMR spectroscopy can be used as a sensitive probe of the both the amount and type of microstructure formation.

2.1 Introduction

Metallic lithium anodes have been considered as one of the prospective and attractive energy materials due to its high energy density and specific capacity of 3800 mA h g^{-1}. However, the commercial application of the use of lithium metal anodes in secondary lithium ion batteries (LIBs) has not been successful since there are crucial problems related to morphological changes on the lithium metal surface such as uneven growth of microstructure (dendrite or moss) upon cycling and formation and degradation of a solid electrolyte interface (SEI) on the electrodes. Even though diverse modifications Li batteries to prevent the drawbacks have been attempted, a fundamental understanding of the conditions of growth of Li microstructures in a working battery is still needed to improve.

Here we report a phenomenological analysis of the *in situ* NMR spectra of lithium. By constructing cells with natural abundance Li metal (92.5% ^{7}Li, 7.5% ^{6}Li) and isotopically enriched ^{6}Li metal (95%) strips, we are able to observe the deposition of microstructure of one Li isotope onto the bulk metal strip of the other isotope, the method allowing the signals of the microstructure to be definitively assigned and the skin depth effect to be explored. An *in situ* NMR and *ex situ* SEM study was performed on the same cells to assign the different Li metal resonances seen with different stack pressures and separators to different types of microstructure. Two separators were studied: Celgard (a laminate of polypropylene and polyethylene) and a borosilicate glass microfiber. Different types of Li microstructure (dendrites or moss) result in different shifts of the Li microstructure NMR resonances, allowing the formation of different morphologies to be tracked in real time. A model that accounts for the different shifts of the various microstructures is developed based upon results from susceptibility calculations and experimental NMR and SEM data, leading to an increased understanding of the growth of microstructures on Li metal anodes.

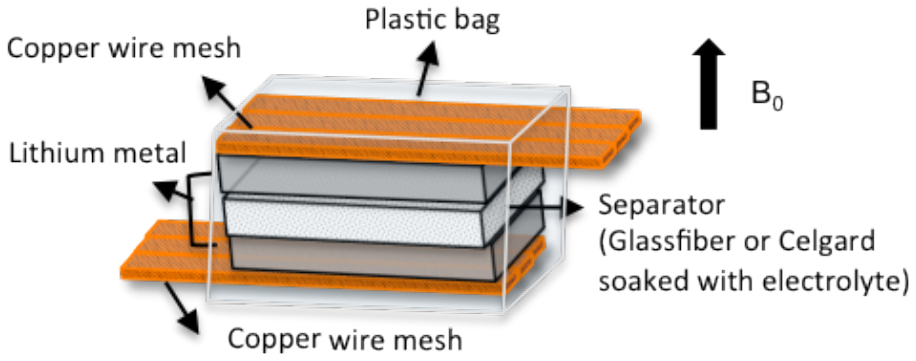

Figure 2.1 Schematic configuration of a bag cell with its orientation, perpendicular to the magnetic field, $\mathbf{B_0}$. Two Li metal strips were used with two types of separators (Glass microfiber, Celgard).

2.2 Experimental

2.2.1 Sample Preparation for NMR and SEM

All Li-Li symmetric cells used in the $^{6/7}$Li NMR and SEM experiments were made with a 1M $LiPF_6$ in EC (ethylene carbonate)/ DMC (dimethyl carbonate) (1:1 by vol.) electrolyte (Novolyte). All sample preparations were carried out in an argon-filled glove box. The lithium metal (Aldrich, 92.5% ^{7}Li and Isotec, 95% ^{6}Li) electrodes were cut to dimensions of 4 mm × 10 mm × 0.38 mm for the ^{7}Li NMR and SEM experiments, and to 6 mm × 15 mm × 0.3(8) mm for the ^{6}Li NMR experiments then cleaned with hexane before attaching them to a copper wire mesh current collector. Two different separators with different porosities and thickness were used; glass (borosilicate) microfiber separator (Whatmann, type GF/B, thickness 0.68 mm, pore size 1.0 μm)[1] and Celgard (2325, thickness 25 μm, pore size 28 nm, porosity 40%)[2]. SEM studies could only be performed on the Celgard cells, since it was difficult to remove all the fibers from the surface of Li microstructures when the glass microfiber separator was used. The bag cells were hermetically sealed and enclosed in a transparent polyester bag (Kapak Corporation type

500-24) (Figure 2.1). The bag cells were then wrapped in Teflon tape to align their position in the NMR coil.

In order to study the effect of pressure on the formation of Li microstructures, bag cells were held between microscope glass slides using two binder clips to provide an increased and homogenous stack pressure. Pressure indicating films (Sensor Products INC.) were used to measure the applied stack pressure of 5.78 ± 0.87 atm with an accuracy of ±15%, by placing the film between the bag cell and the Teflon tape. The stack pressure of a bag cell was also measured in the absence of applied external pressure. The pressure indicating film was placed inside a cell between the electrode and the separator, and then the bag cell was sealed without electrolyte. The pressure was found to be less than 1.9 atm, the lower limit of detection of the pressure indicating film. At the edges of the cell the pressure was 3.9 ± 0.6 atm, this increase is ascribed to extra pressure from the heat sealing procedure and wrapping of the bag cell in Teflon tape.

All electrochemical testing was performed on a Bio-Logic Science Instruments VSP electrochemical cycler. A rate of 1.1 mA/ cm^2 was used for all the experiments in this paper in order to investigate the formation of Li microstructures under consistent electrochemical conditions. In a battery, Li metal acts as the anode and during the charging process Li ions are deposited on the Li metal surface and during discharge they are stripped from the metal surface. In a symmetric Li cell there is no charge/discharge process, thus we use the term "current flow" to describe Li deposition and Li stripping occurring on the negatively and positively charged electrodes, respectively.

In situ $^{6/7}$Li NMR experiments were performed on a Tecmag Redstone spectrometer synchronized with the electrochemical cycler and a 4.7 T magnet. Complete details of the experimental set-up are described elsewhere.[44] All $^{6/7}$Li NMR spectra were referenced to a 1 M LiCl solution at 0 ppm. The lithium cells were oriented perpendicular to the magnetic field, $\mathbf{B}_0$, in a 5 mm (^{7}Li) or 7 mm (^{6}Li) solenoid coil and all spectra were acquired at a resonance frequency of 77.5 MHz for ^{7}Li and 28.9 MHz for ^{6}Li at room temperature. The p/2 pulse lengths (optimized on LiCl) of 1.8 μs and 2.3 μs were used for the ^{7}Li and ^{6}Li experiments, respectively. The recycle delay of 1.0 s was chosen to be greater than the T_1 of ^{7}Li metal (~100 ms)[3]. This

recycle delay is not optimized for observation of the electrolyte (T_1 > 3s) as the focus of this work is on the metal peak. Each spectrum took ~2 min to acquire consisting of 128 transients. The filling factor for the 5 mm coil/bag cell is 0.29 and for 7mm coil/bag cell is 0.22. The filling factor was not optimized for the system due to several other considerations that were more central to the overall viability of the experiments. These include the functionality of the bag cells as electrochemical devices, as well as rf field effects associated with the induced eddy currents in the conducting sample.[44]

In order to find the direct correlation between the Li NMR spectra and SEM images, the cells cycled in the NMR spectrometer were carefully taken out and dissembled in the glove box. The lithium electrodes were washed with DMC to remove the residual electrolyte and dried so as to investigate the microstructures by SEM. For the cross-section SEM images, the sample was carefully cut in the glove box with a razor blade. A LEO1550, Germany SEM, operating at 20 kV with a Robinson backscatter detector was used. The cell was unavoidably exposed to air for one or two seconds during transfer to the SEM chamber.

2.2.2 Susceptibility Calculations Methodology

FFT (fast Fourier transform) susceptibility calculations[4-6] were performed to help confirm the assignment of the Li metal NMR spectra and to explore susceptibility effects associated with microstructure growth on the surface of the bulk metal. The calculations were performed on a 512 × 512 × 512 grid, with a Li metal slab in the center, measuring 400 × 160 × 16 voxels in the x, y and z directions, with $\mathbf{B}_0$ aligned along z. Two different phenomena were considered: (i) changes to the NMR shift of the surface sites in the bulk metal as new Li sites grow on top, and (ii) the shifts of different morphologies of microstructure.

An array of 512^3 points was used for the input grid, representing a cubic cell with 12.775 mm sides, making each point in the array correspond to a 25 μm^3 voxel; of the order of the microstructure size and the effective skin depth of the Li metal. A single Li electrode was represented by a cuboid in the center of the cell measuring 4.0 x 10.0 x 0.4 mm in the x, y, z directions, with B_0 aligned along z, matching the geometry of the NMR experiments. Voxels

inside the cuboid were assigned a volume susceptibility of $\chi_{Li} = 24.1 \times 10^{-6}$ in SI units[7, 8], with the rest of the cell modeled as a vacuum with $\chi = 0.0$.

The formation of microstructure on the electrode was modeled by randomly assigning voxels next to the surface of the major face of the electrode (the 4.0 × 10.0 mm, xy face) as Li metal (i.e. setting $\chi = \chi_{Li}$ in those voxels) and repeating the calculation. This configuration is illustrated in the inset of Figure 2.8 in the main text, where the voxels highlighted in pink correspond to the microstructure. Two effects were investigated: (i) the changes in the spectrum of the microstructure as it was increased from a single voxel in length (a mossy microstructure, Figure 2.8a) to 8 voxels in length (a dendritic microstructure, see also the inset of Figure 2.8b), and (ii) the changes in the ^{7}Li spectrum of the metal making up the original surface layer as the surface coverage increased (Figure 2.3a).

2.2.3 Deconvolutions of NMR spectra

The deconvolution of NMR spectra was performed by a least-square fitting of the recorded lineshapes in 3 different ways (Figure 2.3) in order to explore the sensitivity of the relative intensities to the method used to deconvolute the spectra. The NMR signal within the range of 245 to 280 ppm was fit with a combination of Gaussian/Lorentzian lineshapes and the change in intensity of the bulk metal peak during the *in situ* experiments (i.e., during the formation of Li microstructures) was explored. Fit 1 used a total of 2 peaks, 1 peak for Li bulk metal and 1 peak for Li microstructures. Fit 2 and Fit 3 used a total of 3 peaks, 2 peaks for Li bulk metal and 1 peak for Li microstructures. The addition of a second peak to fit the Li bulk metal is consistent with our earlier work[8] and is ascribed to the different shift from the minor faces of the Li metal strips that are parallel to B_o (the bulk of the signal comes from the major faces perpendicular to B_o). For each of the different fitting procedures, the fit parameters (amplitude, position, FWHM (full width at half maximum) and the ratio of the Gaussian/Lorentzian (G/L) line shape) were initially optimized on the spectra at t = 0 for the bulk metal peak(s) and at t = 240 for the microstructure peak, and were then used as the initial values

for fitting all the *in situ* spectra. Since the shape of the bulk metal could be expected not to change during cycling, constraints were imposed on the fits. In Fit 1 and 2, the parameters were constrained to the initial values for each spectrum, except for amplitude. In Fit 1, only the amplitude of peaks was allowed to vary. For Fit 2, the ratio of the intensity (integrated area) of the 2 bulk metal peaks (blue and red dotted lines) was held constant to account for the intensity of the bulk metal peak decreasing as a function of time. In Fit 2, the peak positions and FWHM were allowed to vary by ±0.5 ppm, and the G/L ratio was constrained between 0.3 and 0.4. In Fit 3 strict constraints were not imposed on the fit parameters, only the peak positions of the 3 peaks were constrained to ensure a 3 peak fit (bulk metal 1: 245 to 246.5 ppm; bulk metal 2: 252 to 254 ppm; microstructure: 258 to 260 ppm).

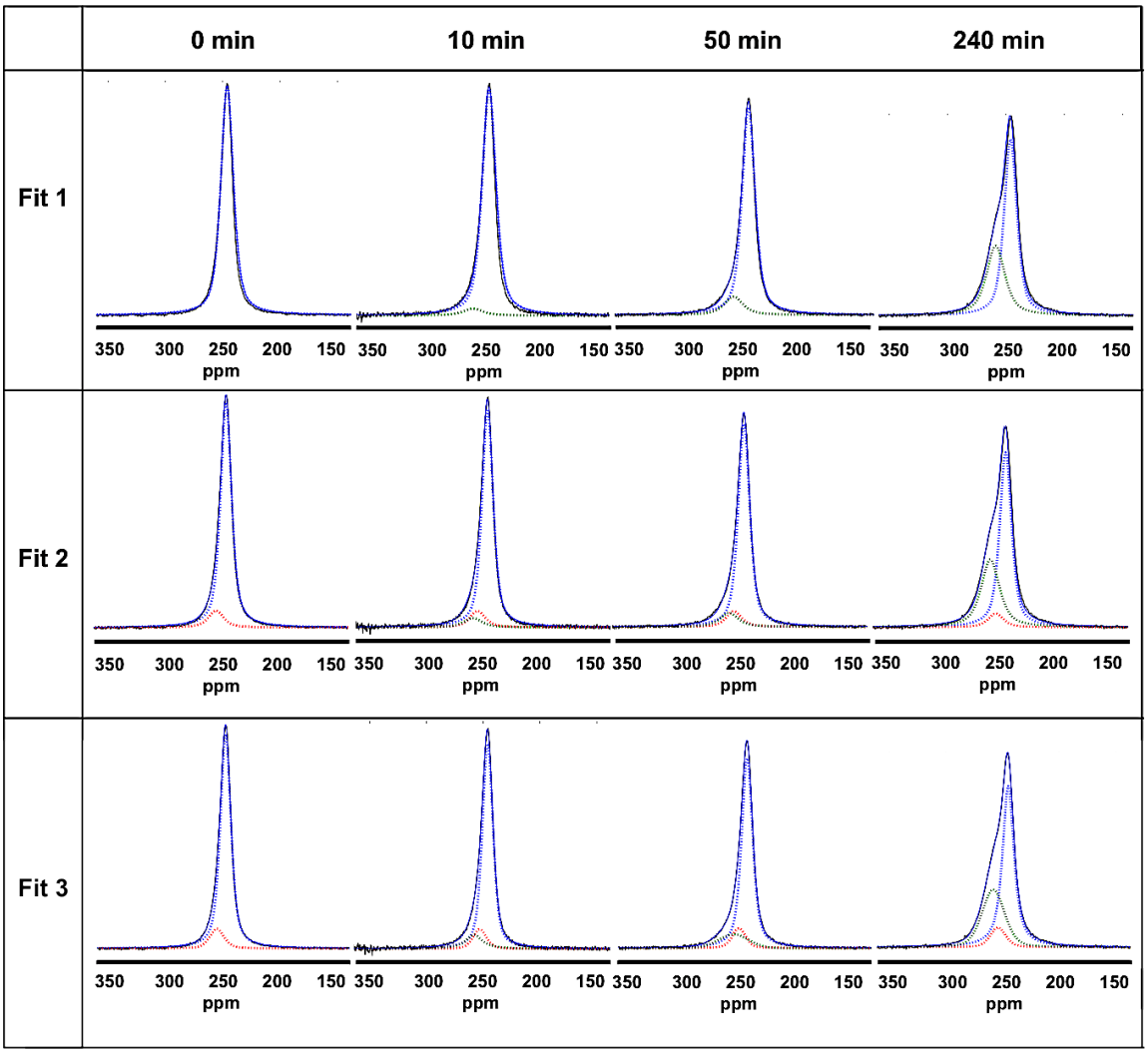

Figure 2.2 Deconvoluted ^{7}Li static NMR spectra of a symmetrical lithium cell with Celgard separator containing $LiPF_6$ in EC/ DMC (1:1 by vol) obtained at 1.1mA/cm^2 for 0 min, 10 min, 50 min, and 240 min. Fit 1 and Fit 2 are performed with constraints on the bulk metal peak, while Fit 3 was performed without constraints. Fit 1 used 1 peak for the bulk Li metal and 1 peak for the microstructures. Fit 2 and Fit 3 used 2 peaks for the bulk Li metal and 1 peak for the microstructures. The fitted peaks are indicated with blue, green and red dotted lines and a thick black and blue line show the experimental spectra and the fit, respectively.

A decrease in the integrated area of the bulk metal peak was observed in all fitting results. Under the freedom from constraints, Fit 3 shows that the reduction in peak amplitude results from peak broadening, which increased by 7%. The results from these fits are shown in Table 2.1.

Peak Fits		Fit 1		Fit 2			Fit 3		
Spectr	Fit Parameters	Bulk	Micro	Bulk	Bulk 2	Micro	Bulk	Bulk 2	Micro
0 min	Amp. (arb. units)	1		0.98	0.07		0.97	0.09	
	Pos. (ppm)	246.1		246.1	254.8		246.1	254.0	
	FWHM (ppm)	13.0		11.3	15.8		11.2	15.1	
	G/L	0.40		0.35	0.35		0.38	0.60	
	Area (arb. units)	17.78		15.40	1.62		14.98	1.69	
10 min	Amp. (arb. units)	0.97	0.03	0.94	0.07	0.04	0.92	0.09	0.04
	Pos. (ppm)	246.1	259.8	246.1	254.8	259.8	246.1	253.1	259.0
	FWHM (ppm)	13.0	18.8	11.3	15.8	18.8	11.0	14.0	17.60
	G/L	0.40	0.30	0.40	0.40	0.40	0.48	0.60	0.00
	Area (arb. units)	17.26	0.79	14.59	1.53	1.01	13.50	1.56	1.74
50 min	Amp. (arb. units)	0.88	0.08	0.88	0.07	0.06	0.84	0.09	0.06
	Pos. (ppm)	246.1	259.8	246.1	254.8	259.8	246.0	253.2	259.0
	FWHM (ppm)	13.0	18.8	11.3	15.8	18.8	11.5	14.0	31.1
	G/L	0.40	0.30	0.40	0.35	0.30	0.38	0.6	0.99
	Area (arb. units)	15.69	2.08	14.14	1.49	1.62	13.44	1.56	2.03
240 min	Amp. (arb. units)	0.76	0.30	0.75	0.06	0.29	0.72	0.09	0.26
	Pos. (ppm)	246.1	259.8	245.7	254.2	259.8	245.7	254.0	259.8
	FWHM (ppm)	13.0	18.8	12.0	15.8	18.8	11.9	16.0	23.43
	G/L	0.40	0.30	0.35	0.35	0.30	0.16	0.60	0.70

Table 2.1 The full *in situ* ^{7}Li NMR spectra of a metallic lithium symmetric cell during multiple cycling with different applied currents. a) Deconvoluted ^{7}Li NMR spectra at four different times (100, 600, 1000, and 1400 min). A total of 3 peaks were used: 2 peaks for Li bulk metal (248 ppm and 258 ppm) and 1 peak for Li microstructures (264 ppm). The deconvoluted peaks are indicated with thin red, blue and green lines and the thick red and blue line (almost invisible under the red line), shows the fit and the experimental spectra respectively. The normalized intensity of microstructures to bulk metal (sum of blue and red line intensity) each of the spectra is 0.00, 0.05, 0.87, and 1.49 respectively. b) Applied current vs. time with currents of 0.11, 0.275, 0.55, 1.1, 5.5, and 11 mA/cm^2 for multiple cycles. Each cycle consisted of 6 min applied positive current then a 2 min rest followed by 6 min applied negative current and 2 min rest. c) Stacked plot of entire *in situ* ^{7}Li NMR spectra.

2.3 Results and Discussion

2.3.1 NMR Studies of Microstructure Formation

In order to correlate the Li NMR observations with specific types of microstructure morphologies a joint SEM/NMR study of a series of cycled lithium electrodes was performed. A symmetric lithium metal cell was used with a Celgard separator. A galvanostatic experiment was performed for a total of 240 min using a constant current of 1.1 mA/cm^2 while spectra were acquired in real time using *in situ* NMR (Figure 2.3). Li^+ in the electrolyte and SEI appear in the chemical shift region expected for diamagnetic salts (-10 to 10 ppm) and hence can be readily separated from the signals due to Li metal.[3, 9] The ^{7}Li NMR signal of the metallic lithium strip is seen at 246 ppm, the major contribution to the shift arising from the Knight shift[10, 11] due to the TIP of the delocalized conduction electrons. An additional Li metal peak at 260 ppm (±3 ppm) begins to appear after 10 min and becomes more noticeable in the spectrum extracted after 50 min (Figure 2.3). The deconvolution was performed to aid in peak assignment and quantification of the Li bulk metal peak.

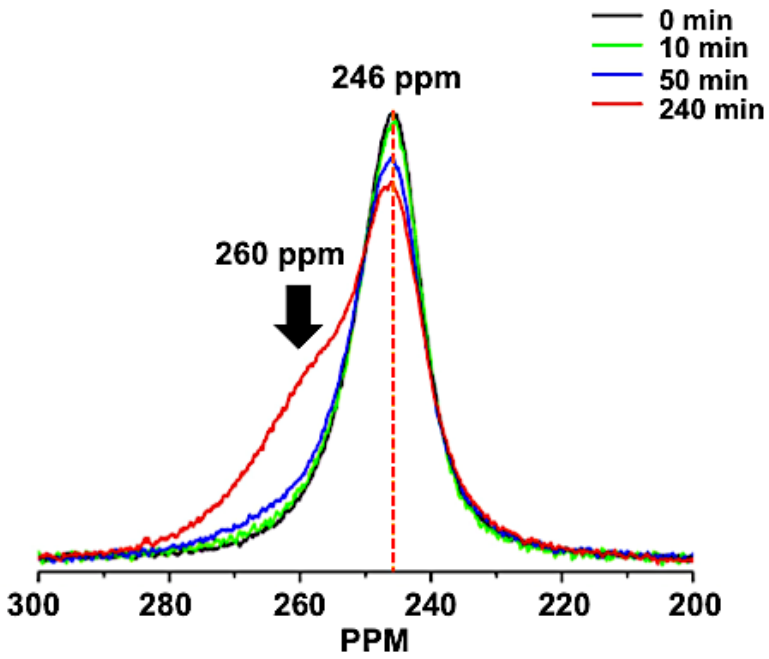

Figure 2.3 Change of ^{7}Li NMR spectra of a symmetrical lithium cell with Celgard separator containing $LiPF_6$ in EC/ DMC extracted from an *in situ* NMR experiment, after 0 minutes (black), and after passing current for 10 min (green), 50 min (blue), and 4 hours (red) at 1.1mA/cm^2. The normalized intensity of each of the spectra is 1.00, 1.00, 1.03, and 1.46 respectively.

Previous studies by Bhattacharya *et al.* showed that a strip of Li metal placed perpendicular to $\mathbf{B}_0$, resonates at ~245 ppm, while it shifts to ~270 ppm when the strip is parallel to $\mathbf{B}_0$.[3] This orientation-dependent shift arises from the bulk magnetic susceptibility (BMS) effect,[3, 6, 9, 12, 13] caused by the TIP of the Li metal. On this basis, the additional (shifted) resonance was ascribed to dendrites and mossy Li growing perpendicularly to the Li metal anode surface.[3, 6, 9, 12, 13] We will explore this proposal below by comparing NMR data with SEM images and the results from susceptibility calculations.

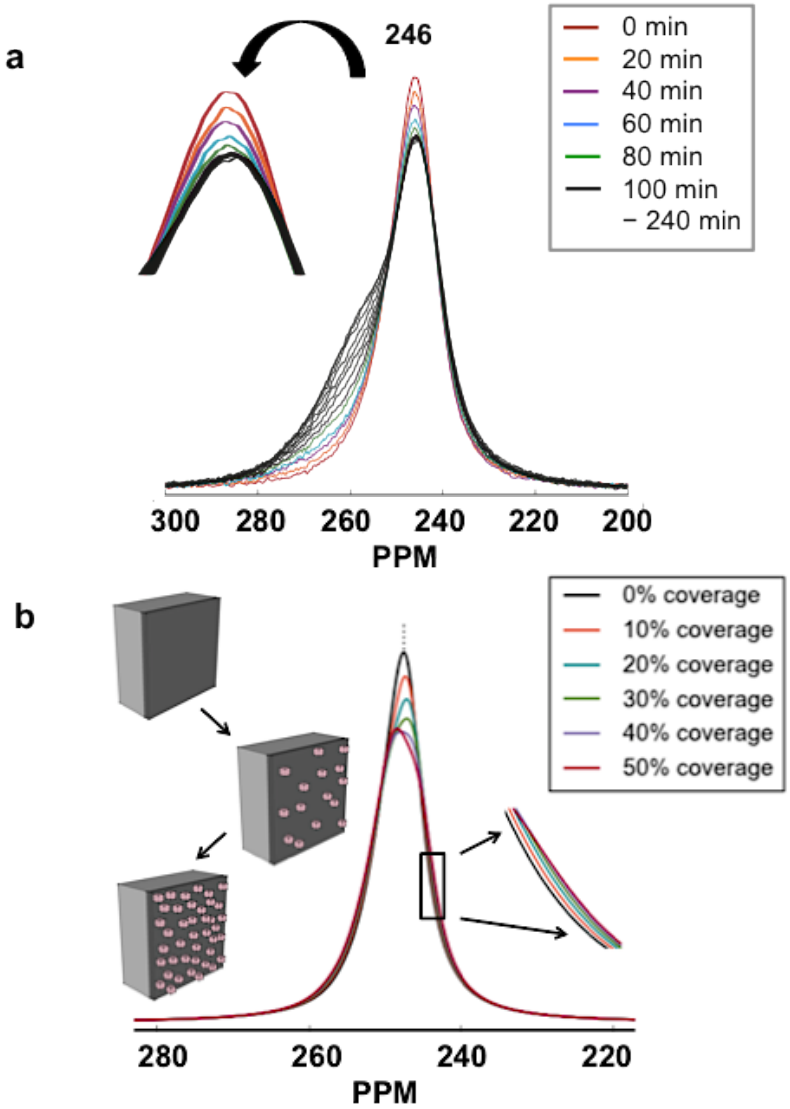

Figure 2.4 (a) Experimental *in situ* ^{7}Li NMR spectra of from the same cell shown in Figure 2.3 (with Celgard separator), but with increased time resolution. (b) Simulated ^{7}Li NMR spectra showing changes in the metal peak as surface microstructure coverage increases. Only Li sites that were originally at the surface of the electrode are included, corresponding to the thin, dark grey region on the inset illustration. The same total number of sites contributes to each spectrum; the integrated intensities of the curves are therefore identical.

A key feature of the series of spectra in Figure 2.3 is that the bulk metal peak at 246 ppm decreases in height over time. This decrease is more clearly observed during the initial stages of the experiment as shown in Figure 2.4a, most of the changes occurring before 80 minutes.

Recently, Indris *et al.* have also reported NMR studies of Li microstructure growth in different electrolytes and have similarly observed a decrease in intensity of the bulk metal peak after the current was applied.[14] However, the origin of the decrease in metal peak intensity with microstructure growth has yet to be clearly addressed. We propose that this decrease can be ascribed to two factors, (i) the build up of microstructure on the surface of the Li metal attenuates the rf, reducing the observable signal from the bulk metal and thus the integrated intensity of the metal peak, and (ii) the microstructures impact the local magnetic field at the surface of the metal, causing inhomogeneous broadening of the Li metal peak. The latter phenomenon is a consequence of the metallic and non-uniform nature of the microstructures, which also display TIP, and is now evaluated using susceptibility calculations. These susceptibility calculations have been described elsewhere and represent a simple method for calculating the variations in the local magnetic field caused by objects with different geometries.[6] The susceptibility calculations are first run on the pristine Li metal cell, and the spectrum is simulated using the calculated shifts for the Li sites at the top surface layer of the electrode only (dark grey region in the illustration inset in Figure 2.4b).

The calculation is then repeated for the same (dark grey) surface sites as increasing coverage of microstructure is randomly added on top of the metal surface. Any attenuation of the rf by the addition of the microstructure is not modeled, so each of the spectra in the series have the same integrated intensity. Figure 2.4b shows the resulting simulated ^{7}Li NMR spectra showing changes in the metal peak as surface microstructure coverage increases. As the coverage of the random microstructure increases at the surface of the electrode, the simulated NMR spectra of the Li metal surface sites (Figure 2.4b) show a clear decrease in peak height as the peak broadens (demonstrated more clearly in the expanded region of the spectra on the right). In practice, it is difficult in the experimental spectra to distinguish between a decrease in the intensity of the main Li metal resonance (due to rf attenuation) and simply peak broadening (from susceptibility effects), because the simultaneous growth of the microstructure peak as a shoulder of the main metal peak, hinders integration and accurate deconvolution of the main resonance. The simulation results, however, clearly show that at least some of the reduction in peak height results from peak broadening. Furthermore, and as discussed above, the

experimental results suggest that significant coverage of the metal surface with microstructures occurs within an hour. After that, additional microstructural growth must occur further away from the Li metal surface and so does not contribute to susceptibility changes that can further broaden the bulk metal peak. In contrast, if rf attenuation by the microstructure layer were the more significant effect, the peak would be expected to continually reduce in intensity throughout the experiment as the microstructure continues to grow, suggesting that rf attenuation is not the main factor influencing the decrease in peak height.

It is of note that Bhattacharya *et al.*[3] did not observe any noticeable decrease in the intensity of the bulk ^{7}Li metal peak during multiple charge-discharge cycles (>28 up to 0.5 mA / cm^2) of a symmetric Li cell cycled with the 1-ethyl-3-methylimidazolium tetrafluoroborate ionic liquid electrolyte, although they did observe an additional peak associated with microstructure growth. They therefore assumed that the rf penetration of microstructures was total, and the intensity of the bulk metal peak during Li deposition/stripping was assumed to be constant. We have repeated their experiment under the same electrochemical conditions but with the EC: DMC electrolyte used here, and have confirmed that there is no noticeable decrease in the intensity of the main bulk metal peak during multiple cycling (Figure 2.5). This is most likely because under multiple cycles at lower current, different morphologies of microstructures are formed and partly removed from both electrodes, thus they do not accumulate with the same thickness and/or density as when a single direction of current flow is applied. The different morphologies formed on the metal surface can be expected to contribute differently to both the rf attenuation and inhomogenous line broadening effects.

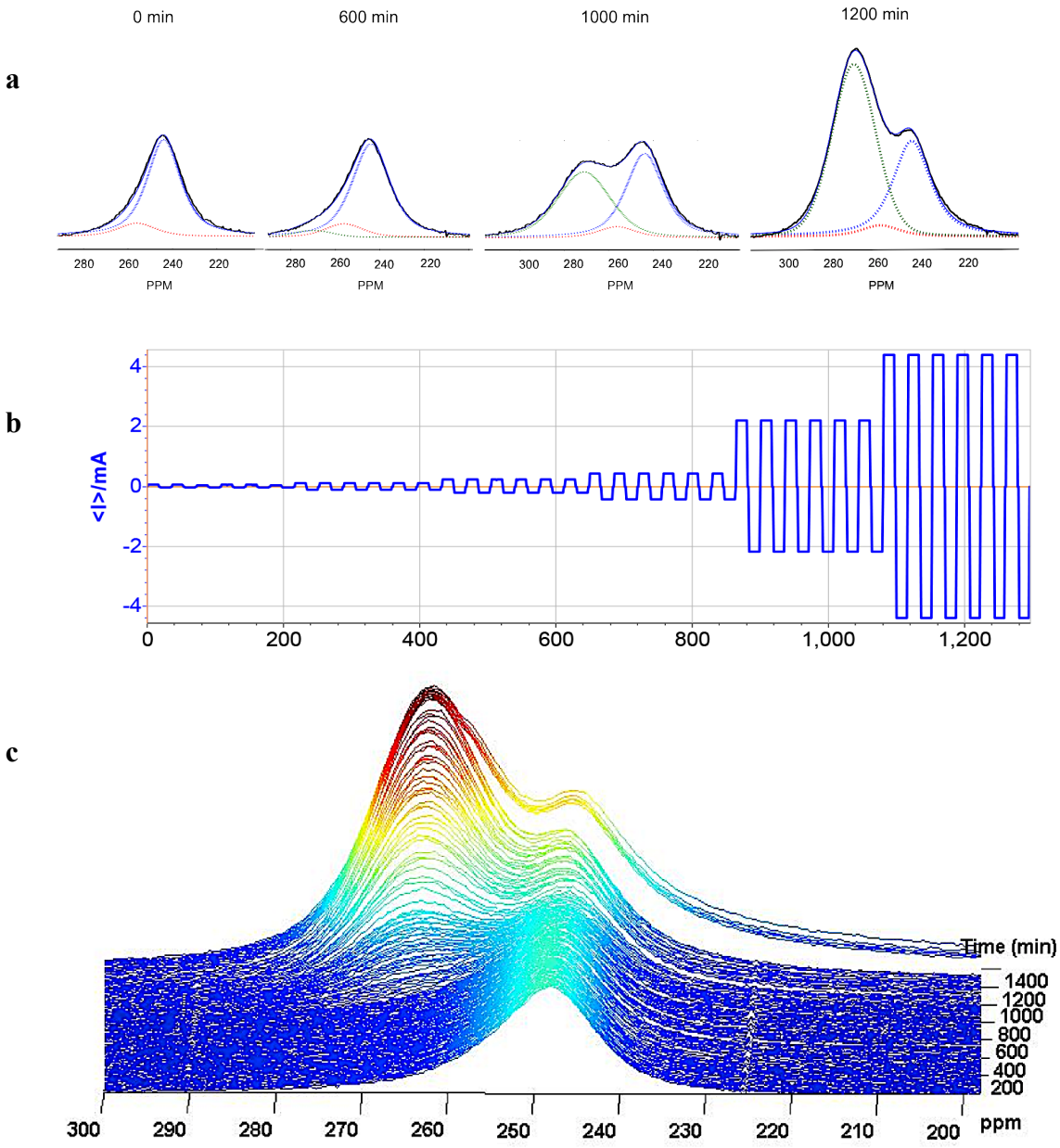

Figure 2.5 The full *in situ* ^{7}Li NMR spectra of a metallic lithium symmetric cell during multiple cycling with different applied currents. a) Deconvoluted ^{7}Li NMR spectra at four different times (100, 600, 1000, and 1400 min). A total of 3 peaks were used: 2 peaks for Li bulk metal (248 ppm and 258 ppm) and 1 peak for Li microstructures (264 ppm). The deconvoluted peaks are indicated with thin red, blue and green lines and the thick red and blue line (almost invisible under the red line), shows the fit and the experimental spectra respectively. The normalized intensity of microstructures to bulk metal (sum of blue and red line intensity) each of the spectra is 0.00, 0.05, 0.87, and 1.49 respectively. b) Applied current vs. time with currents of 0.11, 0.275, 0.55, 1.1, 5.5, and 11 mA/cm^2 for multiple cycles. Each cycle consisted of 6 min applied positive current then a 2 min rest followed by 6 min applied negative current and 2 min rest. c) Stacked plot of entire *in situ* ^{7}Li NMR spectra.

2.3.2 SEM Studies of Microstructure Formation

To determine if the shift of the Li microstructure peak is dependent on the nature of the microstructures, SEM experiments were performed on four symmetric lithium cells under the same conditions as used for the *in situ* NMR studies. Note that all these experiments were performed with Celgard separators rather than with glass microfiber separators due to the Li dendrite growth into the glass microfiber, making it difficult to remove the separator without destroying the Li microstructures. SEM was carried out on the same cell used in the *in situ* NMR study following current flow for 240 min (Figure 2.3 and Figure 2.6d,h,l) and separate cells were prepared so that they could be studied after 0 min, 10 min, 50 min using *ex situ* NMR and SEM studies (Figure 2.6). The SEM image after 10 min clearly shows the formation of a thin Li

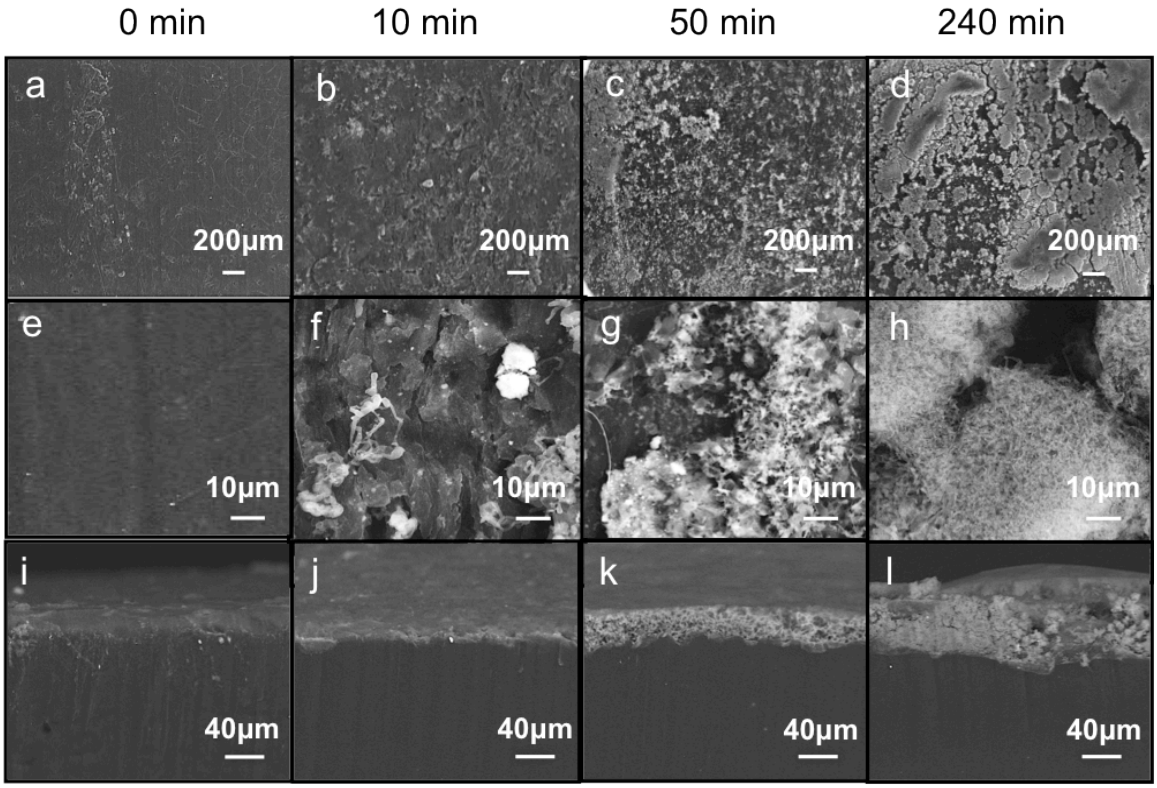

Figure 2.6 Morphological changes on the Li metal surface as a function of time. SEM images of the surface and the cross-section after charging at 1.1mA/ cm^2 for (a,e,i) 0 min, (b,f,j) 10 min, (c,g,k) 50 min, and (d,h,l) 240 min. (a-d) Surface images, (e-h) higher resolution surface images and (i-l) cross-section images.

microstructure layer (<1 μm) sparsely spread over the surface (Figure 2.6j). As current was passed for longer times, larger amounts of Li microstructures were observed, unevenly plated on the Li surface. The cross-sectional images at 50 min show that the microstructure layer thickness is approximately 32.5 μm and increases to 100 μm after 240 min of current flow. The increased thickness of the microstructure layer observed by SEM correlates well with the rapid growth of the additional NMR peak at 260 ppm.

2.3.3 ^{6}Li/^{7}Li Isotope Studies of Microstructure Formation

To separate changes in shift and peak intensity due to microstructure formation from changes in the bulk Li metal intensity, cells with one enriched ^{6}Li electrode and one natural abundance ^{7}Li electrode were studied. As one isotope (^{X}Li) is electrochemically transferred to the other electrode (^{Y}Li), the changes seen in intensity of the ^{X}Li metal peak should be dominated by the signal originating from the microstructures. These experiments also allow the effect of microstructure and/or smooth ^{X}Li deposits on the attenuation of the signal of the ^{Y}Li strip (the ^{Y}Li intensity should decrease) due to the rf skin depth to be explored.[3, 15] Four *in situ* NMR experiments of four cells (two monitoring ^{6}Li and the other two monitoring ^{7}Li during current flow) were used where two experiments transferred ^{6}Li to the natural abundant electrode (referred to here as the ^{7}Li electrode), while the two other experiments transferred Li from the ^{7}Li to ^{6}Li electrode.

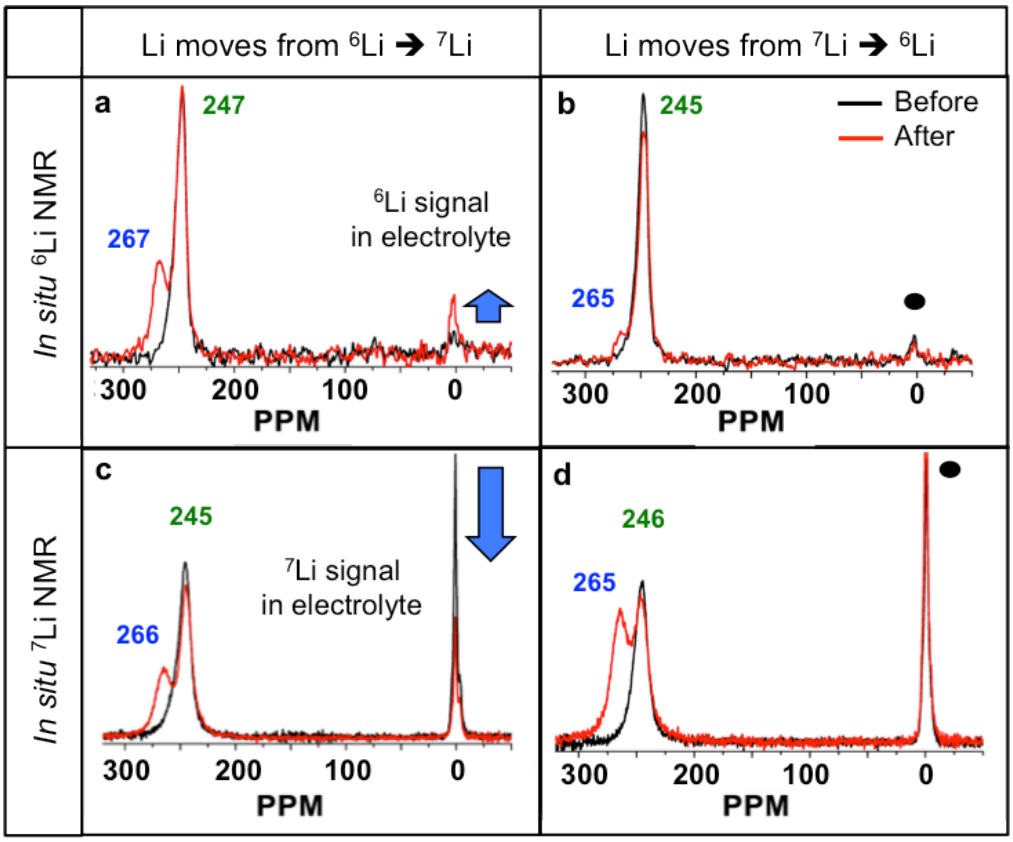

Figure 2.7 The change of ^{6}Li and ^{7}Li NMR spectra before and after growth of microstructures. Comparison of *in situ* (a,b) ^{6}Li and (c,d) ^{7}Li NMR spectra of the cell comprised of a ^{6}Li metal strip against ^{7}Li metal with dimensions 6 mm × 15 mm × 0.4 mm and a glass microfiber separator, after current flow at 1.1 mA/cm^2 for 240 min. In (a,c) Li ions move from the ^{6}Li to ^{7}Li strip and in (b,d) Li ions move from the ^{7}Li to ^{6}Li strip. The black spectra correspond to the pristine state (before passing current) and the red spectra correspond to the final state (after current flow). The arrows refer to the change in intensity of electrolyte and the dots indicate no noticeable change in intensity.

In all of the experiments, the formation of a distinct peak at ~266 ppm, associated with dendritic microstructure formation,[15] is observed in the spectra after current flow (Figure 2.7). When Li is transferred from the ^{6}Li electrode to the ^{7}Li electrode, an intense microstructure peak is observed in both the ^{6}Li and ^{7}Li spectra. The peak at 267 ppm in the ^{6}Li spectra is consistent with the growth of ^{6}Li microstructures on the ^{7}Li electrode (Figure 2.7a). The observation of the peak at 266 ppm in the ^{7}Li NMR spectra (Figure 2.7c) is unexpected, but is ascribed to the use of a natural abundance (92.5% ^{7}Li) electrolyte; as the Li ions diffuse from the ^{6}Li electrode, the first

ions to deposit on the ^{7}Li surface will be the ^{7}Li ions in the electrolyte. This is supported by the noticeable decrease in the intensity of the electrolyte peak in the ^{7}Li NMR spectrum (and increase in the ^{6}Li NMR electrolyte signal) after 240 min of current flow. When the cell was charged with Li ions moving from the ^{7}Li electrode to the ^{6}Li electrode, the ^{7}Li microstructure peak at 265 ppm was observed due to ^{7}Li microstructure formation on the ^{6}Li electrode (Figure 2.7d). Additionally, a small increase of the ^{6}Li metal dendrite peak at 265 ppm was observed (Figure 2.7b) and is ascribed to the naturally abundant ^{6}Li in the ^{7}Li microstructures (7.5%). No changes in the ^{6}Li or ^{7}Li NMR peak intensity in the electrolyte region are observed, as expected, since Li ions are transferred from a natural abundance electrode.

The tendency of the bulk metal peak to decrease in height is consistently observed in the isotope experiments. Changes in the apparent bulk metal intensity are greater in the ^{7}Li spectra compared to the ^{6}Li spectra. This is due to the different rf skin depths for the two isotopes: ^{6}Li has a larger skin depth (28.5 μm) than ^{7}Li (17.1 μm), and so a larger amount of the pristine metal is detected, the microstructure peak becoming a smaller fraction of the overall intensity. When Li is moved from the ^{7}Li electrode to the ^{6}Li electrode and from the ^{6}Li electrode to the ^{7}Li electrode, the bulk metal peak decreases in the ^{6}Li (Figure 2.7b) and in the ^{7}Li (Figure 2.7c) spectra. These decreases can be explained by the susceptibility effects discussed above, and/or by attenuation of the rf by the microstructure and smoothly deposited Li on the metal surface. Both of these effects predict a stronger reduction in the ^{7}Li signal compared to ^{6}Li because of the reduced skin depth; for the susceptibility effects this is because more of the signal comes from closer to the metal surface and so will be more strongly affected by local field changes. It is likely that both of these effects contribute to the apparent reduction in height of the metal peak, as discussed above.

As Li is moved from the ^{7}Li electrode to the ^{6}Li electrode (Figure 2.7d), a (11%) decrease in height of the ^{7}Li bulk metal peak is also observed. This decrease cannot arise from rf attenuation due to microstructure formation since there is no deposition on the ^{7}Li metal surface. Instead, it is possible that the decrease is due to susceptibility changes at the ^{7}Li electrode as the surface morphology changes when Li is stripped from it, and/or more long-range effects from the microstructure formed on the ^{6}Li electrode. The decrease is most pronounced at the beginning of

the experiment suggesting it is not due to formation of dendrites close to the ^{7}Li electrode. However, these proposals require further investigation.

When Li is moved from the ^{6}Li electrode to the ^{7}Li electrode (Figure 2.7a), a slight increase is observed in the bulk ^{6}Li metal peak. This increase may be attributed to smooth deposition of ^{6}Li on the ^{7}Li surface and the possible exchange of the now enriched ^{6}Li electrolyte with the ^{7}Li bulk metal surface after current flow.

Finally, the microstructure peak is better resolved in the spectra presented in this section, in comparison to those presented in the section 2.3.1, which were acquired with borosilicate and Celgard separators, respectively. In the next section we explore the origins of this difference and whether NMR can be used to detect different types of microstructures.

2.3.4 The Effect of Separator and Stack Pressure on Microstructure Formation

To further investigate the dependence of the shift of the additional NMR metal peak on the type of Li microstructure formed and to investigate the effect of pressure on microstructure formation, bag cells with and without the application of an external pressure of 5.8 ± 0.9 atm were studied. An initial stack pressure of 1.9 atm was measured in bag cells with glass microfiber and Celgard separator, the stack pressures being similar for the two separators within the uncertainty of the measurement. In the cell with a glass microfiber separator without external pressure, a sharp peak at 267 ppm is observed after current flow, in addition to the main bulk Li metal peak at 246 ppm (Figure 2.8a), consistent with the results obtained in the isotope studies (section 2.3.3). The ^{7}Li NMR spectrum of the cell with the Celgard separator without external pressure applied shows the growth of a peak at 267 ppm (Figure 2.8c) after current flow. This peak is much less distinct than that observed for the cell with glass microfiber (Figure 2.8a), indicating that the choice of separator affects microstructural growth.

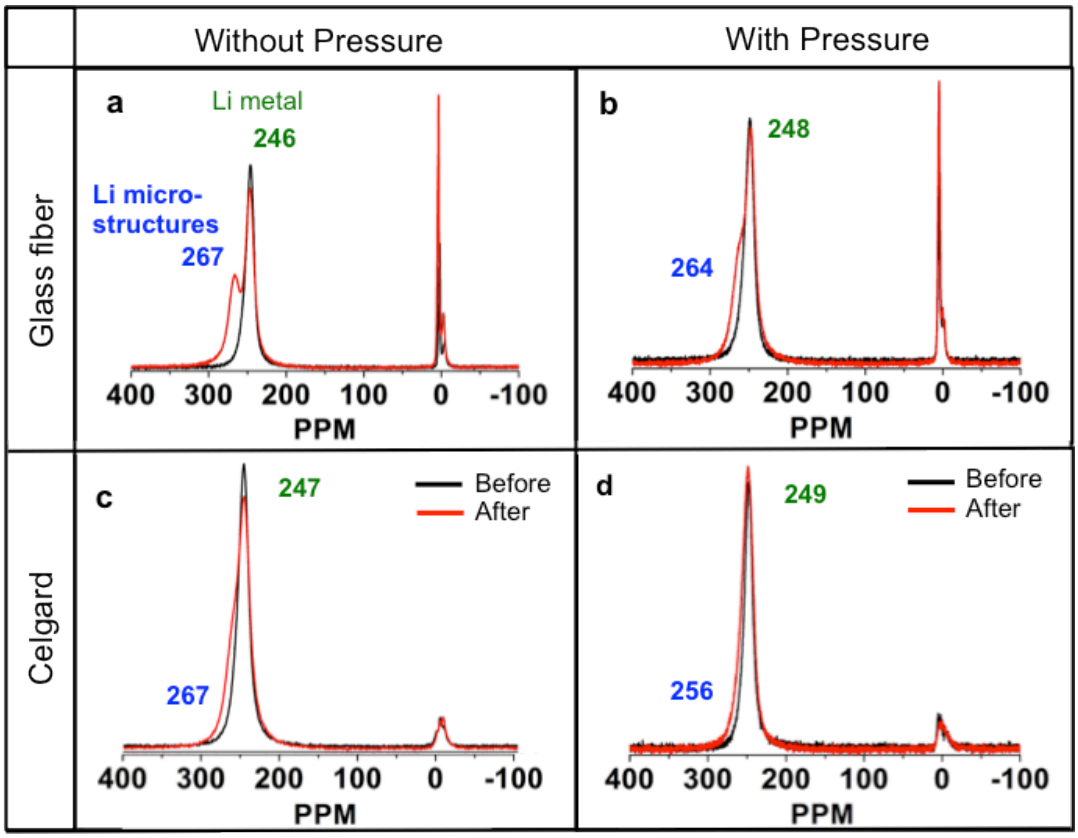

Figure 2.8 The effect of pressure on the formation of microstructures. Comparison of ^{7}Li NMR spectra of a symmetrical lithium cell with (b.d) and without (a,c) an applied pressure of 5.78 kg/ cm^2 (±0.867 kg / cm^2), before and after Li deposition at 1.1 mA/cm^2 for 240 min. Two different separators were studied: (a,b) glass microfiber and (c,d) Celgard. The black line corresponds to the pristine state (before current flow) and the red line corresponds to the final state (after current flow). (Note that slight differences in the line shape, shift and intensity between the before and after current flow spectra of the bulk metal peaks may arise due to uncertainty in the exact alignment of the bag cell perpendicular to $\mathbf{B}_0$ since the pressure experiments were acquired *ex situ*, where the bag cell is removed and reinserted into the NMR coil.)

A resolved peak at around 266-270 ppm was not observed in either of the cells with pressure (Figure 2.8b, 8d) confirming that the external pressure hinders the formation of dendritic type structures, additional intensity now being visible only as a shoulder to higher frequencies of the bulk Li peak at approximately 264 ppm (glass microfiber) and 256 ppm (Celgard). The pressure effect seems more pronounced in the cell with Celgard, resulting in a broadening of the bulk Li metal peak skewed to higher frequencies (Figure 2.8d). We ascribe

these differences to the very different porosities and uniformities of the two membranes, leading to the formation of different Li microstructures. Celgard is a much thinner (25 μm) membrane with a smaller pore size (28 nm)[2] as compared to glass microfiber separator (thickness 0.68 mm, average pore size 1.0 μm).[1] Although the stack pressures are nominally similar, there are likely more open pores within the glass microfiber membrane where the microstructures can continue to grow.

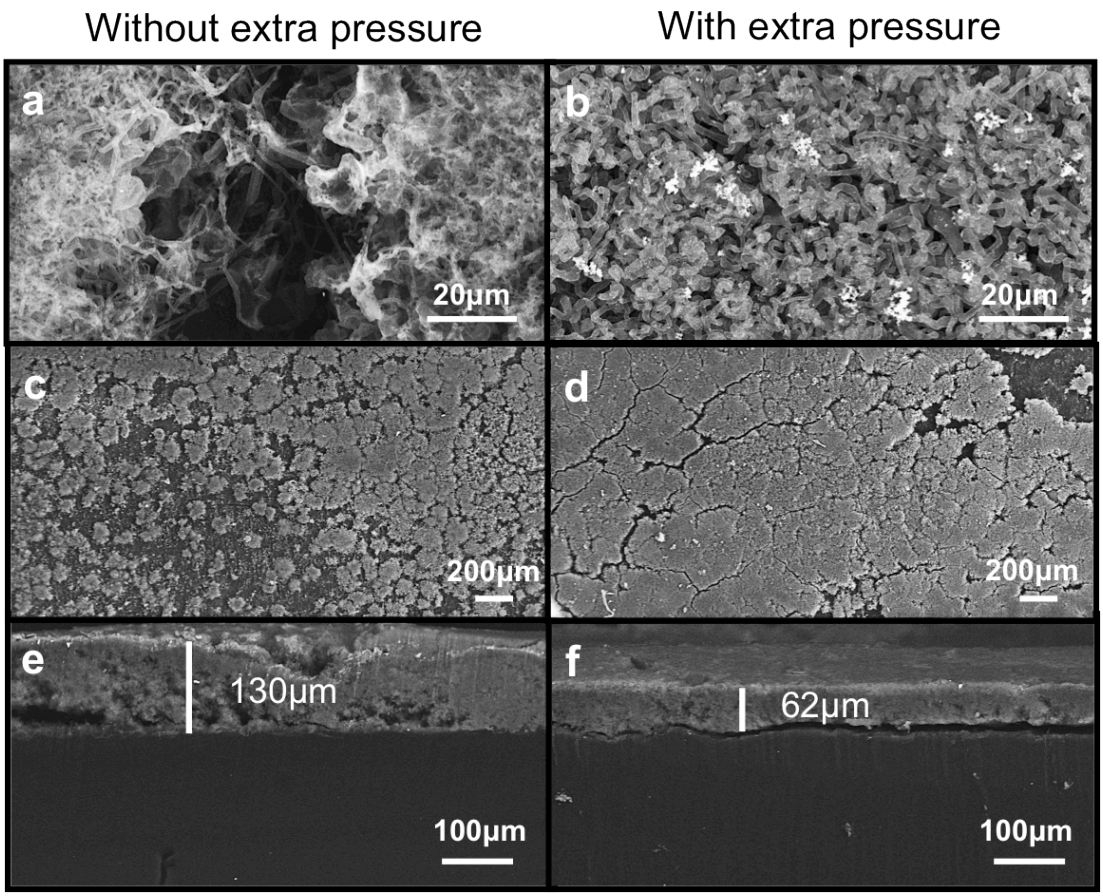

Figure 2.9 SEM images of Li microstructures formed under different external applied pressure. SEM surface and cross-section images of a Li metal electrode after charging at a current density of 1.1mA/cm^2 for 240 min for a cell (a,c,e) without extra pressure and (b,d,f) with extra pressure and using a Celgard separator. SEM images for the (a,b) Li microstructures of the cell, (c,d) Overall surface image and (e,f) cross-section images are shown.

SEM images of the two cells using Celgard with and without external pressure confirm the assignments of the microstructural Li metal peaks observed in the ^{7}Li NMR spectra. Under pressure, a uniform layer of Li deposits was observed (Figure 2.9b, d, and f). Densely packed microstructures (density 0.183 g / cm^3, porosity 65.7 %) with a rounded shape and smooth edges (mossy lithium features) occupy the entire surface. The microstructure density was calculated from the amount of theoretical mass of Li transfer and their volume determined using the thickness of the microstructure layer measured in the SEM cross-section images and the dimensions of the Li metal strip. The porosity of the microstructure layer was calculated from the

ratio of the microstructure density to the bulk Li metal density (0.534 g / cm^3) (1 - r_{micro}/r_{bulk}). These morphological features are correlated to the shoulder (at 256 ppm) on the bulk NMR peak (Figure 2.9b, d, and f). No needle-like dendritic features are observed in the SEM images, further supporting the hypothesis that the application of external pressure to the cell suppresses dendrite growth. A much thicker, less dense (density 0.087 g / cm^3, porosity 83.7%) layer with needle shapes (dendritic features) associated with the NMR peak at 267 ppm (±3 ppm) was detected without applied external pressure (Figure 2.9a, c, and e). The Li microstructure layer in the cell with external pressure is almost two times as dense as the layer in the cell without external pressure. The NMR and SEM results support the hypothesis that a strong peak near 270 ppm indicates microstructural growth perpendicular to the lithium metal surface, i.e., a dendrite. The results are in good agreement with previous MRI experiments that identified two different types of Li microstructures using chemical shift imaging (CSI), CSI providing spatial mapping of chemical shift information.[15] The overall directional growths (parallel or perpendicular to $\mathbf{B}_0$) of Li microstructures result in different shifts, the Li dendritic features protruding into the space in between the bulk metal electrodes having a narrow range of shifts near 270 ppm and microstructures with mossy shapes growing in the vicinity of the bulk metal surface have broad peaks covering a large frequency range (262 ppm to 274 ppm). These results indicate that NMR is a sensitive method for evaluating the type of Li microstructures without disassembling cells.

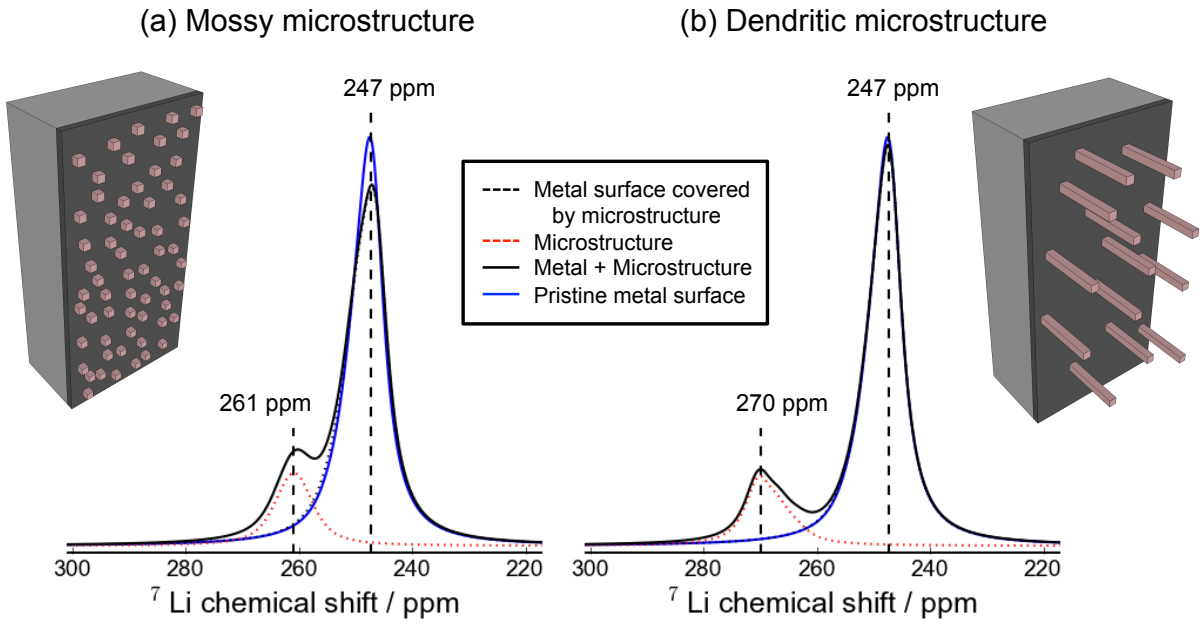

Figure 2.10 Simulated spectra from the FFT susceptibility calculation results for a Li electrode with (a) a mossy type microstructure and (b) a dendritic microstructure covering the surface. The inset Figures illustrate the shape of the microstructure in each case, with pink voxels corresponding to the microstructure and the darker grey section of the electrode representing the surface layer of voxels that are the only ones represented in the spectrum.

To further confirm the assignment of shifts to dendritic or mossy morphologies, two possible morphologies of microstructure were modeled in the FFT susceptibility calculations; mossy microstructure as $1 \times 1 \times 1$ voxels distributed randomly over the *xy* surface of the metal with 20% surface coverage, and a dendritic structure as $1 \times 1 \times 8$ voxels covering 2.5% of the metal *xy* surface (both models contain the same total amount of Li). Schematics of the two models and the resulting simulated NMR spectra of the systems before and after the addition of the microstructure are shown in Figure 2.10. The isotropic chemical shift of the bulk metal peak and the microstructure peak are in good agreement with the experimental values of ~245 ppm and ~260 ppm, respectively. When the spatial extent of the microstructure is increased, the corresponding peak shifts to higher frequency (270 ppm) as shown in Figure 2.10b. This microstructure morphology has a strong resemblance to dendrites that can be expected to grow perpendicular to the surface of the electrode (parallel to $\mathbf{B}_0$). Although these simple models are

limited in their ability to represent the fine structure and densities of different types of Li microstructure growth, they do confirm that higher chemical shifts can be associated with microstructures that grow more anisotropically and perpendicular to the electrode such as dendrites.

2.4 Conclusions

In situ NMR and SEM were performed to identify the Li NMR signatures of different Li microstructures. ^{7}Li NMR spectra show an additional Li metal peak at ~270 ppm, which is shifted from the bulk metal peak at ~245 ppm and is attributed to Li microstructures. The additional peak appeared at the beginning of current flow and rapidly grew from 50 min to the end of the current flow. Results from cells with isotopically (^{6}Li and ^{7}Li) enriched Li electrodes confirm the assignment of this second peak. Under applied external pressures, a condition where dendritic morphologies are not expected to readily form,[16, 17] microstructure peaks are observed in the NMR spectra at shifts that are lower than 270 ppm and even appear as a broadening (skewed to higher frequencies) to the bulk metal peak. SEM images showed that the relative density of the Li microstructure layer was approximately two times greater when an external pressure is applied to the bag cell. These SEM images were used to help assign the additional NMR peaks to different Li morphologies and show that the Li microstructures gradually increase on the surface as a function of time. A dense Li microstructure (or mossy layer) layer gives rise to an additional NMR peak shifted by only 10 ppm from the bulk metal peak, whereas, a thicker but more dendritic microstructure layer correlates with peaks observed at a higher frequency of ~270 ppm. Susceptibility calculations confirmed the assignment of peaks at higher chemical shifts to microstructures that grow perpendicular to the electrode (dendrites). They also show that a significant reduction in the height of the bulk metal peak can occur as the surface coverage increases, arising due to changes in the local magnetic susceptibility in the regions of the metal close to the microstructure that leads to inhomogeneous broadening of the metal peak. The assignments of the NMR peaks enable us to characterize the types of Li microstructures of a functioning battery in a non-destructive way.

The further application of the techniques used in this paper to understand microstructural growth under different electrochemical parameters, such as various currents and different electrolyte salts/ solvents are ongoing and will provide an improved fundamental understanding of the conditions of Li microstructure formation. Furthermore, combining these techniques with the spatial resolution of MRI will provide more insight into the interpretation of the NMR shift

of different microstructure morphologies and details of the mechanisms of microstructure growth.

2.5 References

1. http://www.gelifesciences.com/webapp/wcs/stores/servlet/catalog/en/GELifeSciences-us/products/AlternativeProductStructure_16176/28418346.
2. P. Arora and Z. M. Zhang, *Chem. Rev.*, 2004, **104**, 4419-4462.
3. R. Bhattacharyya, B. Key, H. Chen, A. S. Best, A. F. Hollenkamp and C. P. Grey, *Nat. Mater.*, 2010, **9**, 504-510.
4. R. Salomir, B. D. de Senneville and C. T. W. Moonen, *Concepts Magn. Reson.* , 2003, **19B**, 26-34.
5. J. P. Marques and R. Bowtell, *Concepts Magn. Reson. B* 2005, **25B**, 65-78.
6. A. J. Ilott, S. Chandrashekar, A. Klockner, H. J. Chang, N. M. Trease, C. P. Grey, L. Greengard and A. Jerschow, *J. Magn. Reson.*, 2014, **245**, 143-149.
7. D. Gugan, *Phys. Rev. B*, 1997, **56**.
8. F. T. Hedgcock, *Phys. Rev. Lett.*, 1960, **5**, 420-423.
9. N. M. Trease, L. Zhou, H. J. Chang, B. Y. Zhu and C. P. Grey, *Solid State Nucl. Magn. Reson.*, 2012, **42**, 62-70.
10. R. K. Harris, E. D. Becker, S. M. C. De Menezes, P. Granger, R. E. Hoffman and K. W. Zilm, *Solid State Nucl. Magn. Reson.*, 2008, **33**, 41-56.
11. C. P. Slichter, *Principles of Magnetic Resonance*, Springer-Verlag, 1990.
12. R. E. Hoffman, *J. Magn. Reson.*, 2006, **178**, 237-247.
13. A. Kubo, T. P. Spaniol and T. Terao, *J. Magn. Reson.*, 1998, **133**, 330-340.
14. N. Schweikert, A. Hofmann, M. Schulz, M. Scheuermann, S. T. Boles, T. Hanemann, H. Hahn and S. Indris, *J. Power Sources*, 2013, **228**, 237-243.
15. S. Chandrashekar, N. M. Trease, H. J. Chang, L.-S. Du, C. P. Grey and A. Jerschow, *Nat. Mater.*, 2012, **11**, 311-315.
16. T. Hirai, I. Yoshimatsu and J. Yamaki, *J. Electrochem. Soc.*, 1994, **141**, 611-614.
17. S. I. Tobishima, K. Hayashi, Y. Nemoto and J. I. Yamaki, *Electrochim. Acta*, 1998, **43**, 925-933.

Chapter 3

Effects of different cations via self-healing electrostatic shield (SHES) mechanism on suppression of dendritic Li deposition

Abstract

The self-healing electrostatic shield (SHES) mechanism proposed by Zhang *et al.*[1, 2] was investigated to our system to investigate effects of non-Li^+ SHES additives on growth and suppression of Li electrodeposition by *in situ* nuclear magnetic resonance (NMR) and scanning electron microscopy (SEM). The different additives M^+PF_6 (M= Cs^+, K^+) at the low concentration, give lower reduction potentials than Li were added to the control electrolyte solutions (1M $LiPF_6$ in ethylene carbonate: dimethyl carbonate (EC:DMC) and in propylene carbonate (PC)). Efficient suppression of dendrites is only observed with 0.05 M $CsPF_6$ in PC, although PC-based electrolytes tend to grow more dendrites than the mixtures of EC:DMC-based electrolytes with and without the additives. SEM images exhibited Li microstructure layers with small spherical structures structures in PC with $CsPF_6$, which correlates well with the NMR results.

3.1 Introduction

The SEI layer strongly affects the Li deposition and cycling performance of Li metal batteries.[3, 4] Cohen *et al.* proposed a dendrite growth mechanism in an alkyl carbonate solution (such as EC:DMC or EC:DEC (diethyl carbonate)) based on the inhomogeneous nature of the SEI.[5] They report that the SEI in non-aqueous solutions is intrinsically non-uniform. This causes localized Li deposition and stripping on the surface where the SEI has a higher ionic-conductivity, either due to a thinner layer thickness or due to more ion-conductive compositions. This results in a stress between the shape changing lithium layer and the SEI on top, resulting in dendrite growth. Aurbach *et al.* found successful suppression of dendritic deposition in 1,3-dioxolane (DOL) with $LiClO_4$.[6] This was attributed to the high elastomeric content in the SEI, which makes it flexible enough to withstand the volume changes in the lithium electrode during cycling without cracking, in contrast to other SEI layers formed in different solvents.

Various organic solvents have been investigated to reduce the formation of Li microstructures such as, ethers, DME (dimethyl ether) and DEE (diethyl ether), and esters, PC, EC, DMC and DEC in combination with different lithium salts, such as, $LiClO_4$, $LiPF_6$, $LiAsF_4$ and $LiBF_4$. It is generally believed that binary/multi-solvent mixture electrolytes (i.e. EC:DMC) are more stable than single-solvent systems (i.e. PC), because of the synergistic effect of their physical properties such as dielectric constant, viscosity, and reactivity to electrodes. In non-aqueous alkyl carbonate based electrolytes, various Li salts in a mixture of EC:DMC always show a higher ionic conductivity than in PC. Particularly, in the $LiPF_6$-based electrolytes, which are studied here, the Li salt in EC:DMC (10.7 mS cm^{-1}) has a higher ionic conductivity than in PC (5.8 mS cm^{-1}). Among all possible combinations, the mixture of EC and DMC showed the highest cycling performance using 1M $LiPF_6$ due to high anodic stability of EC on cathode surfaces, high solvation energy of EC toward lithium salts, and low viscosity of DMC to promote ion transport.[7] West *et al.* showed that a low PC content in a PC:DMC based electrolyte with $LiPF_6$ can delay the onset time of first dendrite growth on insulated copper wire, because of the high interfacial resistance of the SEI layer leading slower Li transport thorough the SEI.[8]

Recently, Ding *et al.*[1, 2] have reported the self-healing electrostatic shield (SHES) mechanism to suppress dendrite formation on Li metal anodes. They discovered the effectiveness of the additives of cesium hexafluorophosphate ($CsPF_6$) and rubidium hexafluorophosphate ($RbPF_6$) on suppressing dendrite growth. At low concentration, the reduction potential of Cs^+ or Rb^+ is less than the reduction potential of Li^+ therefore, instead of depositing Li or plating Cs or Rb, the Cs^+ or Rb^+ cations are expected to be attracted preferably towards Li protrusions creating an electrostatic shielding. Accumulation of the additive cations at these protrusions or nucleation points will repel positively charged lithium cations and prevent further Li deposition particularly at the protrusion tip and directs the plating towards recessed and flat areas. Therefore, these authors proposed that the effect of the Cs^+ additive forming an electrostatic shielding layer contributed to the lithium ions being smoothly deposited on the surface with no dendritic shape formed during the charging process.[1, 2] However, in $Li/Li_4Ti_5O_{12}$ coin cell, the average Columbic efficiency of Li deposition is found to be still low (~76% in case of 1 M $LiPF_6$-PC in their study) with dendrite-free morphology of Li deposition. Therefore, there is still a need to fully understand and to improve the effectiveness of SHES mechanism for long-term cycling of the battery.[1]

Here we report the study of the SHES effect on dendrite formation using $CsPF_6$ and KPF_6 as additives with two control electrolytes (1M $LiPF_6$ dissolved in EC:DMC or PC solvent) in a Li symmetrical cell. The investigation was conducted by a combination of ^7Li *in situ* NMR and SEM techniques. The amount of microstructures formed was quantified based on the theory, proposed by Bhattacharyya *et al.*[20]. It is found that the total amount of Li microstructures formed after current flow in PC based electrolytes was always larger than in EC:DMC based electrolytes. Furthermore, 0.05M $CsPF_6$ in PC is the only electrolyte that shows efficient suppression of Li microstructures. We were not able to observe the SHES effect using the additive of KPF_6, although 0.01M KPF_6 has a lower equilibrium reduction potential than Li^+. SEM images exhibited a uniform Li layer with small spherical structures in PC with $CsPF_6$, while more dendritic structures were observed in $LiPF_6$-PC electrolyte and $LiPF_6$-PC with KPF_6.

Cation	Standard reduction potential (V)	Effective reduction potential (V)		
	1 M (= 1 mol L^{-1})	0.001 M	0.01 M	0.05 M
Li+	-3.040			
K+	-2.931	-3.108	-3.049	-3.008
Cs+	-3.026	-3.203	-3.144	-3.103

Table 3.1 Effective reduction potentials of two alkali cations, K and Cs, at different concentrations. The concentrations of the additives that were chosen for the experiments are in red.

3.2 Experimental

3.2.1 Sample Preparation for NMR and SEM

In situ ^{7}Li NMR at 4.7 T with a Tecmag Redstone spectrometer (with a π/2 pulse of 2.5 μs and a recycle delay of 1.0 s) and SEM (LEO1550, Germany) observations of microstructural growth have been performed on symmetric Li-Li (Aldrich) cells separated by glass microfiber separator (Whatmann, type GF/B) for NMR measurements and Celgard (2325) for SEM. Two different additives were used; 0.050 ± 0.004 M $CsPF_6$ (Sigma-Aldrich) and 0.010 ± 0.008 M KPF_6 (Sigma-Aldrich) dissolved with 1M $LiPF_6$ (Sigma-Aldrich) in a mixture of EC:DMC (1:1 by vol.) or PC (Novolyte). The same method reported in Chapter 2 was adopted to prepare all samples for the ^{7}Li NMR and SEM experiments. Six different cells were assembled; 2 cells containing 1M $LiPF_6$ in EC:DMC and PC with no additive, 2 cells containing 1M $LiPF_6$ in EC:DMC and PC with 0.05 M $CsPF_6$, 2 cells containing 1M $LiPF_6$ in EC:DMC and PC with 0.01 KPF_6. Throughout this Chapter the electrolytes, 0.05 M $CsPF_6$ with 1M $LiPF_6$ in EC:DMC and PC, and 0.01 M KPF_6 with 1M $LiPF_6$ in EC:DMC and PC will be referred to as $CsPF_6$-EC:DMC, $CsPF_6$-PC, KPF_6-EC:DMC and KPF_6-PC, respectively. The concentration of the

additives was selected to give a higher effective reduction potential than Li^+ (-3.040 V), 0.01M KPF_6 (-3.049 V ± 0.015 V) and 0.05M $CsPF_6$ (-3.103 V ± 0.002 V), as shown in Table 3.1. However, due to the uncertainty in the effective reduction potential of the KPF_6 electrolytes, reduction potential might be less than Li^+. The cells were charged at a rate of 0.55 mA/cm^2 for 300 min and disassembled for SEM analysis. All experiments in this work were repeated at least once under the same experimental conditions to validate the reproducibility of data. Assignments of NMR peak positions for Li metal and microstructures were determined by the deconvolution method introduced in Chapter 2.

3.2.2 Quantification for Li microstructures

The theory implemented by Bhattacharyya *et al.*[20] was used to quantify the amount of Li microstructures from the Li NMR spectra. Due to the skin depth effect, rf does not penetrate completely into lithium metal, and only a certain thickness, the skin depth (δ), is observed:

$$\delta = \frac{1}{\sqrt{\pi\mu 0}}\sqrt{\frac{\rho}{f\pi\mu r}}, \tag{3.1}$$

where ρ is the resistivity of lithium, f is the Larmor frequency, μ_0 is the permeability of vacuum and μ_r is the relative permeability of lithium. The skin depth for ^{6}Li (28.5 μm) is larger than that of ^{7}Li (17.4 μm) due to its lower Larmor frequency. In their study, Bhattacharyya *et al.* assumed Li microstructures do not experience skin depth effects as they are smaller than the rf skin depth.[20] The NMR signal from the pristine bag cell (t=0) is:

$$S_{bulk}(t) \propto As_o \int_0^c \sin\left[\omega_1(x)\tau_p\right] dx, \tag{3. 2}$$

where $A = 2ab + (a + b)c$ is the surface area of the Li metal, a, b and c are the length, width and thickness of a Li metal strip, respectively, s_o is the signal per unit volume of Li metal and τ_p is the length of the rf pulse.[9] Accounting for the skin depth, d, the rf field, ω_1, decreases exponentially from the surface of the Li metal strip as

$$\omega_1(x) = \omega_1(0)e^{-x/\delta}, \tag{3.3}$$

where $\omega_1(0) = \omega_1$. Using Eq. 3.4, and accounting for thickness of the Li metal strip, c, is greater than the skin depth, Eq. 3.2 becomes:

$$S_{bulk}(t) = As_0 \int_0^{\infty} \sin\left[\omega_1(0)\tau_p e^{-x/\delta}\right] dx. \tag{3.4}$$

Thus, the signal arising from the bulk Li metal strip is approximated as

$$S_{bulk}(t) = 1.7308 As_o \delta. \tag{3.5}$$

As the cell is cycled, the total mass deposited or stripped from the electrode is given by the sum of the smoothly deposited or stripped metal, $M_{SD}(t)$, and the mass of the microstructures, $M\mu(t)$. The mass of metallic Li, $M_{Li}(t)$, is assumed to be constant since the cell is symmetrical,

$$\Delta M_{Li}(t) = M_{SD}(t) + M_{\mu}(t) = 0. \tag{3.6}$$

Equation 3.6 implies that the growth of Li microstructure occurs at the expense of smoothly deposited Li. In addition, it assumes that the lithium metal consumed in forming the SEI is negligible (or that it comes from the Li in the electrolyte only).
The mass of $M_{SD}(t)$ and $M\mu(t)$ can be calculated by:

$$M_{SD}(t) = \rho_{Li}\, a\, b\, c_d(t), \tag{3.7}$$

$$M\mu(t) = \rho Li\, V\mu(t), \tag{3.8}$$

where $c_d(t)$ and $V_\mu(t)$ are the thickness of the smooth deposits and the volume of the microstructures at time t, ρ_{Li} (0.534 g/cm^3 for NA Li and 0.46 for ^{6}Li enriched electrodes[39]). The total NMR signal arising from the bulk metal and the microstructures can be written as:

$$S(t) = S_{bulk}(t) + S_{\mu}(t). \tag{3.8}$$

The signal arising from the microstructures, is

$$S_{\mu}(t) = V\mu(t)s_o, \tag{3.9}$$

and from smooth deposition,

$$S_{SD}(t) = 1.7308abc_d(t)s_o. \tag{3.10}$$

Smooth deposition of Li, by definition, would appear as a bulk Li metal. Note that if the Li is truly smoothly deposited the signal should not change due to the skin depth effect, hence $M_{SD}(t) \propto S_{SD}(t) \approx 0$. In cases where the Li metal is not "smoothly" deposited or removed, changes in $S_{bulk}(t)$ overtime would thus be a result of (1) pitting of the electrode surface increasing or decreasing the surface area, (2) significant removal of Li metal where $c < 2\delta$ or (3) the formation of a thick, dense microstructural layer that rf cannot penetrate. Thus for the above cases,

$$S_{bulk}(t) \approx S_{bulk}(0) + S_{SD}(t) = S(0) + S_{SD}(t). \tag{3.11}$$

Making the NMR signal at time t, is:

$$S(t) = 1.7308\big(A + abc_d(t)\big)s_o\delta + V\mu(t)s_o. \tag{3.12}$$

The change of the NMR signal intensity at time t, normalized to the initial signal intensity is:

$$\Delta I(t) = \frac{S(t)-S(0)}{S(0)} = \frac{abc_d(t)\delta + V_{\mu}(t)}{1.7308A\delta} \tag{3.13}$$

By deconvoluting the NMR peaks, the change in intensity can be calculated as:

$$\Delta I(t) = \Delta I_{bulk}(t) + \Delta I_{\mu}(t), \tag{3.14}$$

where,

$$\Delta I_{bulk}(t) = \frac{S_{bulk}(t) - S(0)}{S(0)} = \frac{abc_d(t)\delta}{1.7308A\delta}, \tag{3.15}$$

and

$$\Delta I_{\mu}(t) = \frac{S_{\mu}(t) - S(0)}{S(0)} = \frac{V_{\mu}(t)}{1.7308A\delta}. \tag{3.16}$$

All parameters can be measured experimentally except $c_d(t)$ and $V_{\mu}(t)$. These two unknown parameters can be calculated from the experimental intensities of the Li NMR spectra.

To verify reliability of quantification results, the total mass of Li microstructures calculated from the NMR spectra intensity was compared to the theoretical Li mass transfer with 100% Coulombic efficiency calculated from electrochemical data,

$$M_{Li,ec}(t) = Cm_{Li}\int_0^t I_C(t)dt, \tag{3.17}$$

where *C* is a Coulomb, m_{Li} is the mass of a lithium atom, and $I_c(t)$ is the current at time t.

3.3 Results and Discussion

The ^{7}Li NMR measurements of symmetric cells (Li/ glassfiber separator/ Li) containing 1M $LiPF_6$-EC:DMC/ PC electrolyte with/ without 0.01M KPF_6 and 0.05M $CsPF_6$ additives were performed. The results reveal that the resonance at around 270 ppm developed after current flow at 0.55 mA cm^{-2} for 300 min (Fig. 3.1). These additional peaks at higher chemical shifts from the bulk metal peak at 245 ppm (± 3 ppm) are attributed to microstructures that grow perpendicular to the electrode (dendrites) as discussed in the previous chapters and shown by previous studies.[9, 10] A significant reduction in the height of the bulk metal peak was observed as the surface coverage by microstructures increases, which is consistent with results presented in the previous chapter. This decrease is ascribed to as discussed in Chapter 2.[10]

The cells in the standard electrolytes 1M $LiPF_6$ in EC:DMC and in PC without additives show growth of the additional peak at 265 ppm (Fig. 3.1a) and 267 ppm (Fig. 3.1b), respectively. In Chapter 2, it was discussed that dendritic Li microstructures in 1M $LiPF_6$-EC:DMC were formed in a cell charged at 1.1 mA cm^{-2}. Even at the lower current density of 0.5mA cm^{-2} being used here, the cell in EC:DMC consistently shows the growth of dendrites (Fig. 3.1a). In comparison to the EC:DMC electrolyte, a more distinguishable (sharp) dendritic peak at 267 ppm is observed in PC (Fig. 3.1b). Quantification of the NMR signal indicates that more microstructures were formed in the PC electrolyte (163.1 μg) compared to the EC:DMC electrolyte (117.7 μg). We ascribe this difference to the formation of a less effective SEI layer in PC compared to EC:DMC. It has been reported that EC-based electrolytes form a homogeneous and stable SEI layer that prevents subsequent electrolyte decomposition as compared to PC-based electrolytes on graphite anodes.[11] Therefore we believe that formation of better SEI layer in EC:DMC electrolytes should have an effect on the prevention of Li microstructure growth.

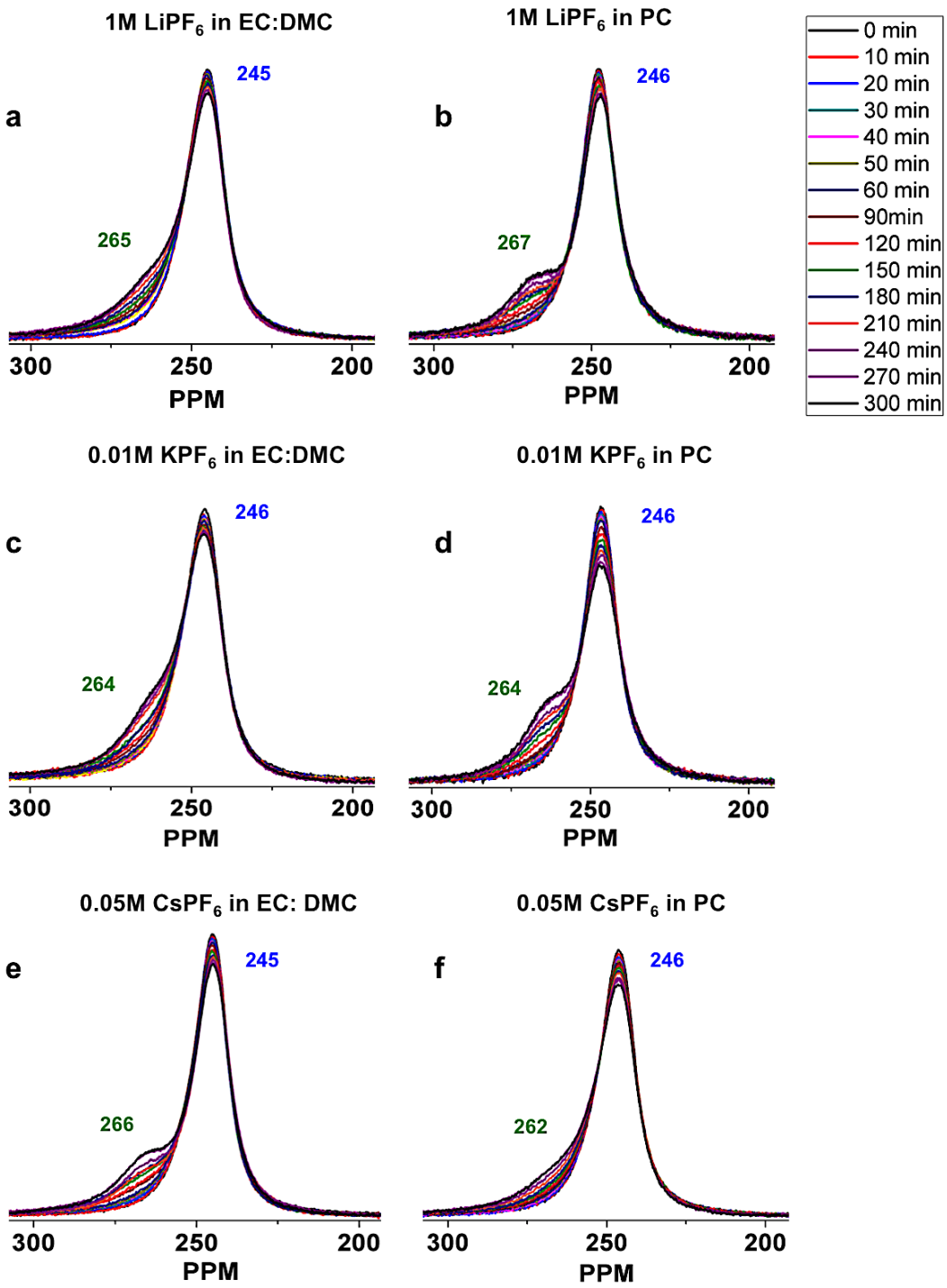

Figure 3.1 *In situ* ^{7}Li NMR spectra of symmetric Li cells (Li/ glassfiber/ Li) with a 1M $LiPF_6$ electrolyte using either EC:DMC (1:1 vol %) or in PC as the solvent, (a,b) without and (c-f) with additives of either 0.01M KPF_6 or 0.05M $CsPF_6$, charged at 0.55mA cm^{-2} for 300 min. The electrolytes used in the cells are (a) 1M $LiPF_6$-EC:DMC, (b) 1M $LiPF_6$-PC, (c) 0.01M KPF_6 in 1M $LiPF_6$-EC:DMC, (d) 0.01M KPF_6 in 1M $LiPF_6$-PC, (e) 0.05M $CsPF_6$ in 1M $LiPF_6$-EC:DMC, and (f) 0.05M $CsPF_6$ in 1M $LiPF_6$-PC.

After current flow, the cell in $CsPF_6$-PC (Fig. 3.1f) shows additional peak growth at 262 ppm, while the cells with KPF_6-EC:DMC (Fig. 3.1c), KPF_6-PC (Fig. 3.1d) and $CsPF_6$-EC:DMC (Fig. 3.1e) show a more distinctive additional peaks at 264, 264 and 266 ppm, respectively. The addition of Cs^+ in PC electrolyte leads to a small dendrite peak with the smallest chemical shift (262 ppm) amongst all the cells. The additional peaks we observed in all the other cells appear at higher resonance. Our results differ from those of Ding *et al.*[1, 2], who observed a dendrite-free surface in Li/Cu and $Li/Li_5Ti_5O_{12}$ cells with 0.05M $CsPF_6$ using multiple-cycling at the current densities ranging from 0.1mA cm^{-2} to 1.0 mA cm^{-2}. In their study, the applied voltage (V_a) was set in between the reduction potential of Li^+ ($E_{Li/Li+}$) and non-Li M^+ ($E_{M/M+}$) cations ($E_{Li/Li+} > V_a > E_{M/M+}$) to avoid reducing M^+ leading to M deposition. In our study, we have controlled the current and monitored the voltage (Fig. 3.2), so it could be possible to reduce M^+ and have M plate on the Li metal surface.

The process of metal dissolution (anodic reaction) or deposition (cathodic reaction) implies movement of charge and thus producing an electric current. Under thermodynamic equilibrium conditions, anodic and cathodic currents are equal with zero net current. Ding *et al.*[1, 2] employed the Nernst equation to calculate the equilibrium potential for the $M^+ + e^- \leftrightarrow M$ reaction for Cs^+ and K^+ ion concentration of 0.05M and 0.01M, respectively. However, if the metal electrode is charged/discharged after applying a current, this equilibrium will be disturbed, and thus no longer at the equilibrium potential. Even though Ding's *et al.* explained the suppression of Li dendrites by setting up the more negative reduction potential of Cs^+ or K^+ than Li+, the equilibrium reduction potential of any M^+, calculated from Nernst equation should not be maintained due to the non-equilibrium process of electroplating. In an actual battery system, when an external current source is applied to a cell, there are a number of resistances causing voltage drops. The difference between the equilibrium voltage (E_{eq}) and resultant voltage (E) is called "overpotential (η) ".

$$\eta = E - E_{eq} \tag{3.18}$$

The major resistance factors leading to the overpotential are the Ohmic drop due to electronic current flow (Ohm's law), the concentration overpotential due to the buildup of electrolyte

concentration gradient in a cell, and the surface overpotential arising from the voltage drop that is needed to drive the reactions.

For a given current density (i), the activation overpotential can be calculated from the Tafel equation, providing a relation between the currents (i and exchange current density= i_0) and the overpotential during the redox reaction. The overpotential (η) can be re-written as,

$$\eta = \left[\frac{RT}{(1-\alpha)nF}\right] \ln i_0 - \left[\frac{RT}{(1-\alpha)nF}\right] \ln i \tag{3.19}$$

where R is the universal gas constant (8.315 J mol^{-1} K^{-1}), T is the absolute temperature in Kelvin (298.15K at RT), F is faraday's constant (96485 C mol^{-1}), and α is the symmetry factor of the energy barrier for anodic and cathodic reactions, nominally 0.5 (when the effect of the change of the potential is identical on both side of the reactions) but can have $0 < \alpha < 1$. From the equation 3.19, the exchange current density for the all cells with different cations can be calculated. The greater the exchange current density, the easier it is for redox reaction to continue due to the lower the activation energy barrier. The smaller the value of i_0, the larger will be the overpotential required to generate a given current. Using the experimentally observed overpotential values from Figure 3.2 in Eq. 3.19, the exchange current density for Li^+ is 0.31 mA cm^{-2} (PC) and 0.71 mA cm^{-2} (EC/DMC), for K^+ is 0.088 mA cm^{-2} (PC) and 0.10 mA cm^{-2} (EC/DMC), and for Cs^+ is 0.23 mA cm^{-2} (PC) and 0.39 mA cm^{-2} (EC/DMC) was calculated. Therefore, it is clear that the cell containing K+ with higher overpotential is the least favorable reaction among all the other cells. Note that calculating the exchange current density for Eq. 3.19, does not account for the current (energy) required to account for resistance or concentration gradients, thus it is a slight overestimation.

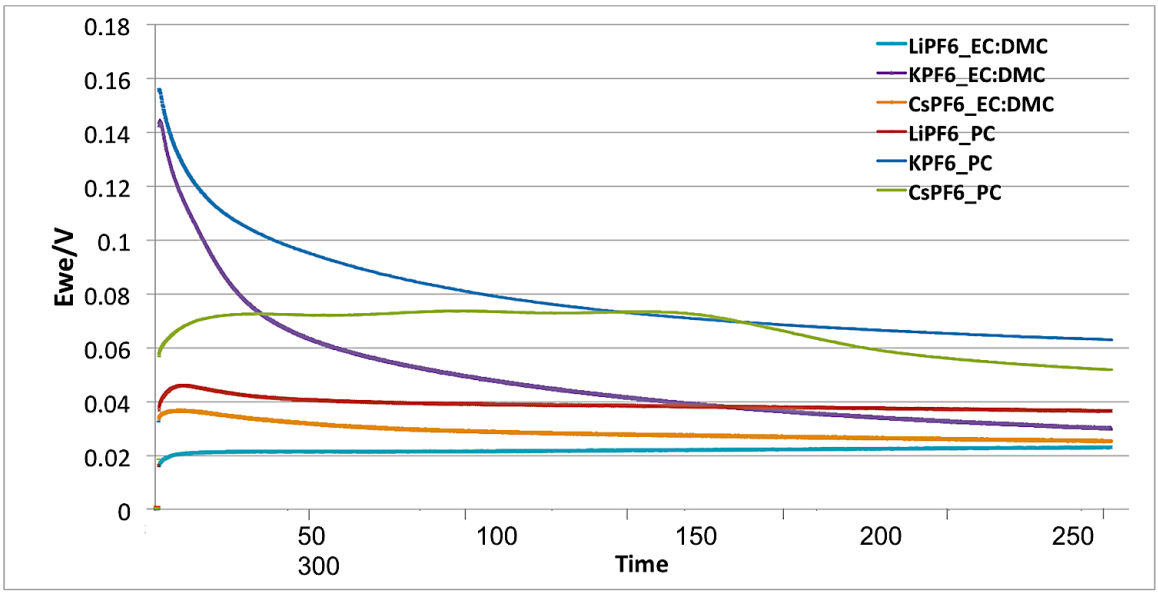

Figure 3.2 The voltage profile of the same cells described in Figure 3.1 as a function of time.

From our observation, we found that actual reduction potential of Li^+ calculated from the experimentally observed overpotential for all the cells with different additives are greater than the standard reduction potential. In other word, M^+ (K^+ and Cs^+) must be plated even in the dilute electrolyte solution due to their less negative standard reduction potential than Li^+. It is a clear indication that increasing in intensity of the dendrite peak at around 270 ppm is a result of the electrodeposition of Li^+ and no SHES effect is observed as in their work[2]. However, the cell overpotential is considered to be composed of a number of independent contributions. The parts of potential are due to Ohmic drop, concentration overpotential, and surface overpotential. Therefore, further work is needed to account for these factors to determine which parameter governs the cell overpotential and how they affect Li deposition process and their morphologies.

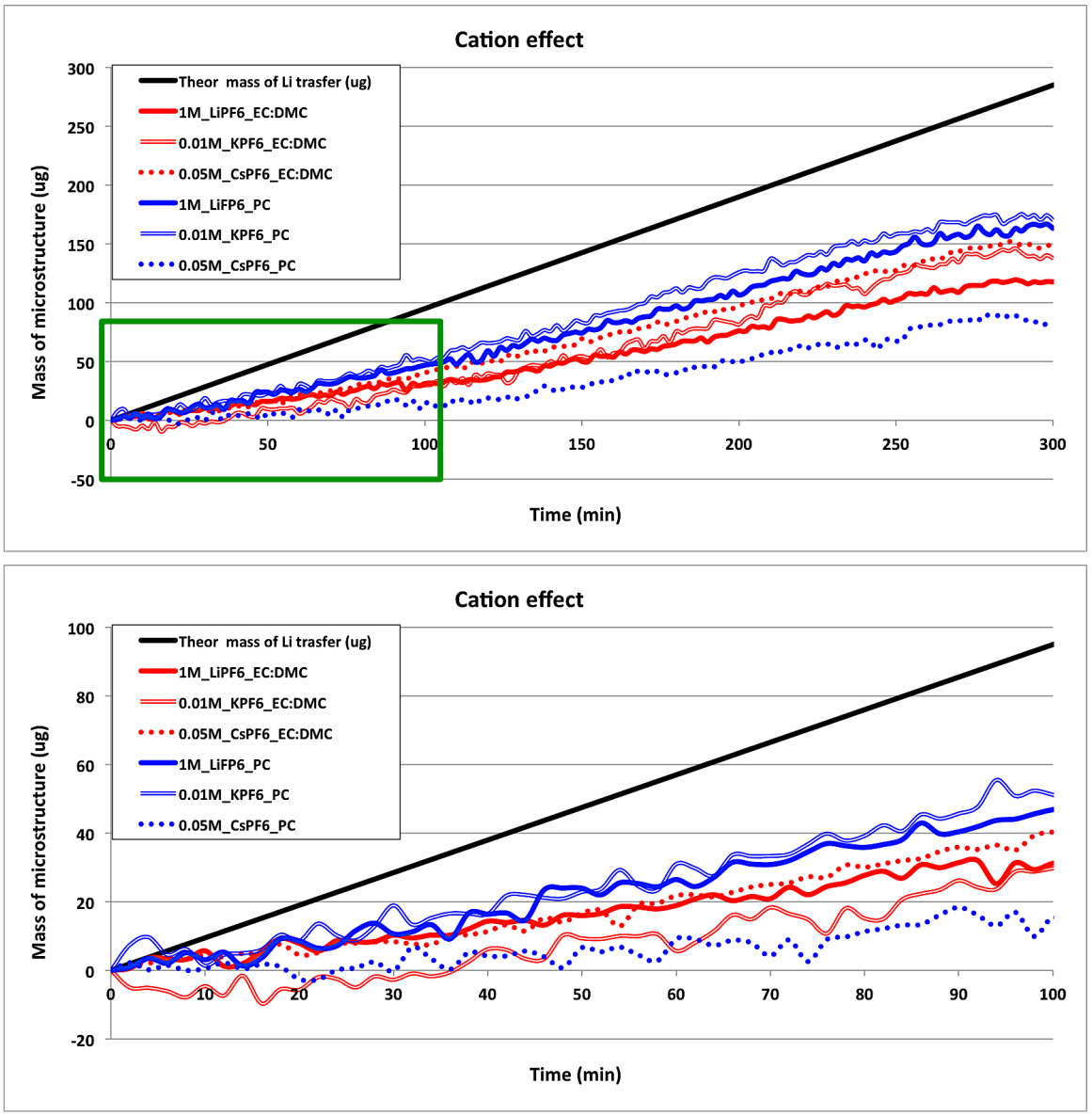

Figure 3.3 Quantification of the ^{7}Li NMR spectra of the cells shown in Fig. 3.1. The cell containing 1M $LiPF_6$ in EC:DMC (1:1 % vol) without additive (red line), 1M $LiPF_6$ in PC without additive (blue line), 1M $LiPF_6$ in EC:DMC with KPF_6 (double red line), 1M $LiPF_6$ in PC with KPF_6 (double blue line), 1M $LiPF_6$ in EC:DMC with $CsPF_6$ (dotted red line), 1M $LiPF_6$ in PC with $CsPF_6$ (dotted blue line), and the theoretical mass transfer of Li during current flow at 0.55 mA cm^{-2} for 300 min (black line). The bottom plot is the enlargement of the region in green rectangular shown in the top figure.

In order to investigate the cation effects in different electrolytes further, quantifications

were carried out based on the change in the NMR signal intensities during current flow.[9] Figure 3.3 shows the comparison of the amount of microstructures of the same cells addressed in Figure 3.1 with respect to the theoretical Li mass transfer (284.8 μg after current flow of 0.55 mA cm^{-2} for 300 min). The total amount of microstructures formed after current passed for 300 min for the cells is: KPF_6-PC (170.3 μg) > $LiPF_6$-PC (163.1 μg) > $CsPF_6$-EC: DMC (149.7 μg) > KPF_6-EC:DMC (137.7 μg) > $LiPF_6$-EC:DMC (117.7 μg) > $CsPF_6$-PC (86.3 μg). As discussed earlier, the amount formed in the PC electrolyte without additives, except $CsPF_6$ was greater than the cells in EC:DMC presumably due to the poor SEI formation. Cells with EC:DMC-based electrolytes with additives formed more microstructures than in the cells without additives after current flow. This suggest that it is possibly due to the stronger SEI layer formed in EC:DMC, compared to PC. The composition of the SEI, thus its properties, can change depending on the different salts, as well as solvents. However, it is not clear whether the SEI formation in the presence of additive is unstable, since it is expected that the M^+ ions should not react to form SEI.[2] Further work is necessary to determine if Cs^+ or K^+ is reacting to form SEI layer (i.e. ^{133}Cs or ^{39}K NMR). As NMR can provide quantitative information of Cs^+ or K^+ in the electrolyte, it should be possible to track the change in intensity of the NMR peak, informing whether the ions are reduced or not during cycling. Although both ^{133}Cs and ^{39}K have a high natural abundance (> 93%), they both are quadrupolar and have very low gyromagnetic ratios, leading to low S/N and requiring special NMR probes to reach their respective Larmor frequencies.

Although NMR has detected the dendrite growth at 265 ppm (± 3 ppm) in all cells, Cs^+ in PC is the only electrolyte/additive combination that shows a significantly smaller amount formed after the current flow. The amount of Li microstructures formed was half that formed in the KPF_6-PC and $LiPF_6$-PC cells. As Ding *et al.*[1] have proposed that Cs^+ ions associate with fewer PC molecules during current flow to create an effective electrostatic shielding of Li^+ from a protrusion of Li metal due to the higher diffusion coefficient ($D= 2.0 \times 10^{-5}$ $cm^2\,s^{-1}$)[12, 13], ionic mobility ($\mu= 7.8 \times 10^{-4}$ $cm^2\,V^{-1}\,s^{-1}$),[12] and lower solvation number of Cs^+ (S.N= 1.6)[14] than Li^+ ($D= 1.2 \times 10^{-5}$ $cm^2\,s^{-1}$, $\mu= 4.7 \times 10^{-4}$ $cm^2\,V^{-1}\,s^{-1}$, S.N.= 3.4)[12, 14] in PC electrolyte. In fact, we expected the $CsPF_6$-EC:DMC to behave similar to the $CsPF_6$-PC electrolyte because of higher diffusion coefficient and solvation number of Li in EC:DMC ($D= 1.2 \times 10^{-5}$ $cm^2\,s^{-1}$, S.N= 4.2)[15]

as well as the more stable SEI formation[11] At this stage, it is not clear why the formation of dendrites in EC:DMC electrolyte is larger. Overall, we presume that the various factors (e.g. diffusion coefficient, solvation number, quality of SEI layer) of the additives in different electrolytes may lead to different results and it needs further work to optimize which parameter is the most important factor in order to suppress Li dendrite formation.

In the case of the KPF_6 additive, we did not observe noticeable inhibition of dendrite growth. Interestingly though, the amount of dendrites formed with KPF_6-EC:DMC is less for the first 100 min after current flow than in 1M $LiPF_6$-EC:DMC. We should point out that negative amount of microstructures for the first 40 min was observed and it is due to the errors in integrations of the spectra (i.e. bad phasing, low signal to noise, etc). However, the overall amount of Li microstructures formed in KPF_6-EC:DMC was larger than in the 1M $LiPF_6$-EC:DMC. The possible explanation is the high overpotential of the cell leading greater reduction potential than the standard reduction potential. As soon as current is applied a relatively high overpotential of 0.15V (Figure 3. 2c and d) is observed in the cells with KPF_6 while the overpotential of the other cells is in the range of 0.02 V to 0.06 V (Figure 3.2). At this overpotential K^+ should be reduced, leading to K plating on the Li metal surface. Although, previous work[16] has shown that metal alloys, with Sn and Al, effectively reduce dendrite formation on the Li metal surface, the phase diagram of Li-K suggest that alloying is unfavorable at room temperature.[17] Thus, despite the similar physical properties of K^+ ($D= 1.9 \times 10^{-5}$ $cm^2\,s^{-1}$, $\mu= 7.6 \times 10^{-4}$ $cm^2\,V^{-1}\,s^{-1}$, S.N=2.4)[12, 14] and Cs^+, we postulate that due to the redox potential of K^+ becomes above that of Li^+ in the KPF_6 electrolytes, leading to no SHES effect, and that K^+ is reduced in the early stages of current flow. The high overpotential caused by unfavorable formation of Li-K alloy supports this hypothesis.

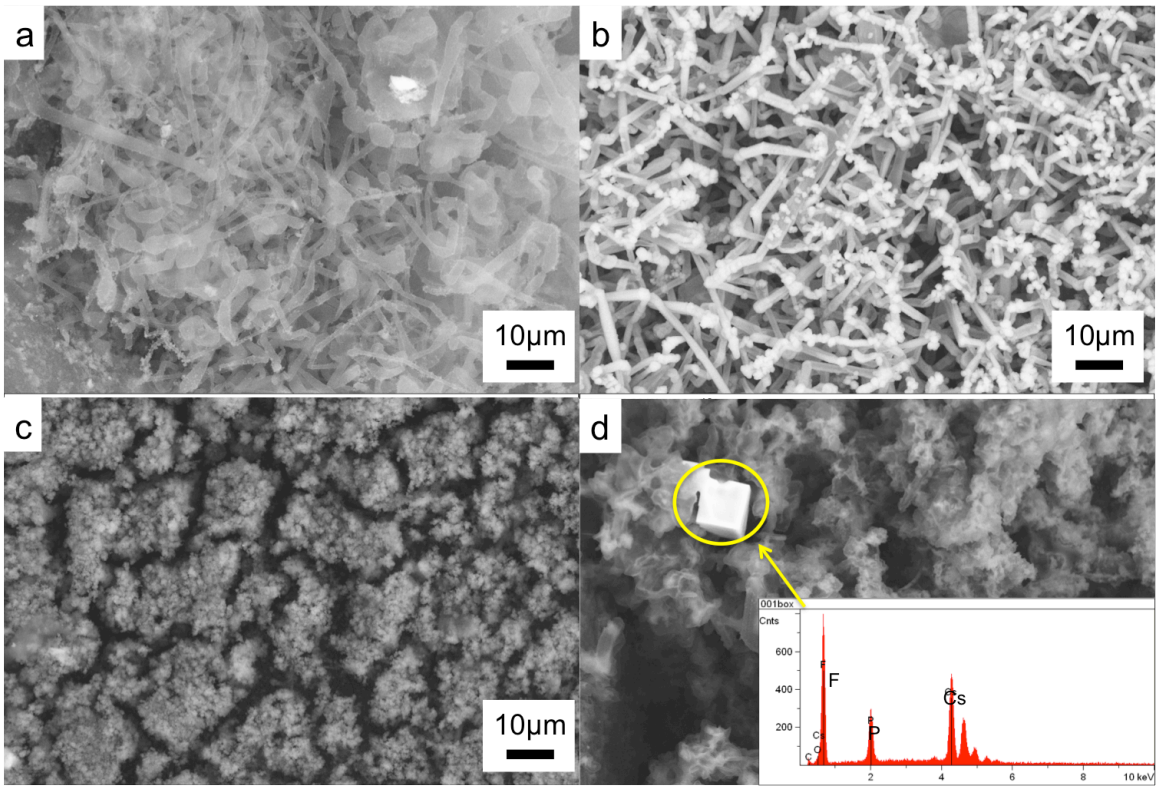

Figure 3.4 SEM images of the microstructures deposited on Li electrodes at 0.55 mA cm^{-2} for 300 min in different electrolyte compositions: a) 1M $LiPF_6$ in PC, b) 1M $LiPF_6$ with 0.01M KPF_6 in PC, c,d) 1M $LiPF_6$ with 0.05M $CsPF_6$ in PC. EDX analysis reveals that $CsPF_6$ salt remains (a square shape in yellow circle) on the surface after current flow.

Figure 3.4 compares the SEM images of the Li electrodes after charge in 1M $LiPF_6$-PC electrolytes with and without additives. The surface morphology of the Li strip varies with the different electrolyte compositions. The Li electrode morphologies obtained in the $LiPF_6$-PC electrolyte (Figure 3.4a) and KPF_6-PC electrolyte (Figure 3.4b) have dendritic structures, while the Li depositions in $CsPF_6$-PC (Figure 3.4c and d) are not dendritic and appear as aggregations with small spherical structures. It is apparent that the morphological features observed with the Cs^+ additive show a decrease in dendrite formation, which is consistent with the NMR results. The EDX analysis shows that $CsPF_6$ salt crystals remain after current flow (Figure 3.4d) suggesting that not all of Cs ions are deposited.

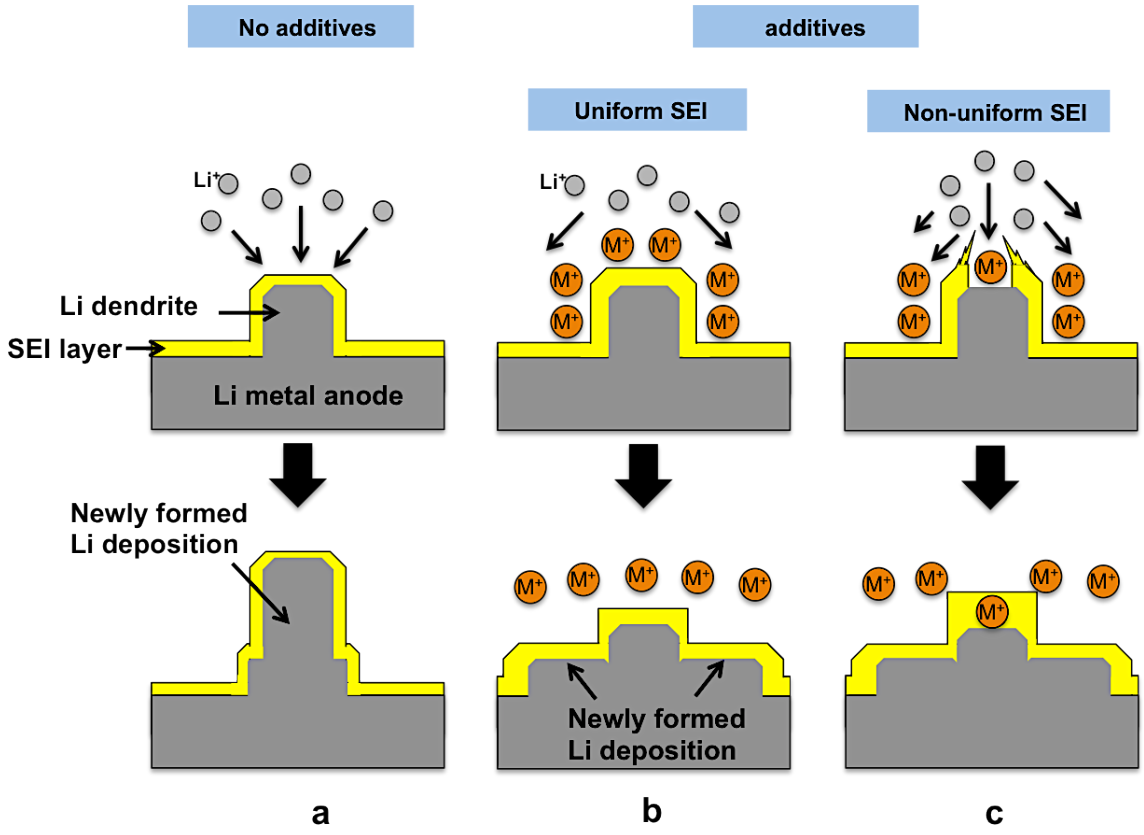

Figure 3.5 Schematic illustration of the Li deposition process on Li metal anodes in cells a) without and b,c) with additives, M^+ (where M = Cs, Rb, K), at concentrations that meet the SHES mechanism conditions. a) SEI layer with no additives. b) Uniform SEI layer with M^+ additive. c) Non-uniform SEI layer with M^+ additive.

Based on our observation and the recent work by Ding *et al.* we correlate the mechanism of Li deposition with the condition of the SEI layer even in the presence of M^+ (M= Cs^+, K^+) additives under the assumption where SHES effect is applicable for the system. Figure 3.5a shows the Li deposition process in the absence of M^+, once a Li protrusion is formed on the surface, due to either the unevenness of the metal surface or any fluctuations (i.e. concentration changes, contaminant surface), a Li dendrite grows from the protrusion. Depending on the stability of the SEI layer, dendrite growth can be either inhibited or accelerated.[18, 19] In the presence of cation additives, M^+ will be adsorbed on the protrusion by an electrostatic attraction force. If a uniform, stable and flexible SEI layer is formed on the metal surface and the

protrusion (Figure 3.5b), the next Li deposition will be repelled by the positively charged electrostatic shield formed by M^+ and will preferably occur at other sites. As a result, growth will not occur from the tip of the dendrite and the SHES mechanism will yield maximum effects on the suppression of dendrites. Under non-uniform SEI conditions, the higher charge density at protrusion may strongly attract not only M^+ but Li^+ as well at the same time. If M^+ shields the protrusion effectively, the SHES effect could work resulting in a dendrite-free morphology on the surface (Figure 3.5c). In contrast, if M^+ cannot shield the highly reactive fresh Li metal protrusion effectively due to the possible reduction of M^+ or limited amount of M^+ to cover, leading to a higher rate of deposition at the protrusion tip than the surface will result in the amplification of Li dendrite growth.

3.4 Conclusion

The SHES mechanism was investigated by the addition of 0.05M $CsPF_6$ and 0.01M KPF_6 to 1M $LiPF_6$ dissolved in EC:DMC or PC solvents in Li symmetrical cells. NMR reveals that the amount of microstructures formed in PC based electrolytes is more than in EC:DMC based electrolytes. These differences are attributed to the different properties of the protective SEI layer produced by different solvents.

Electrolytes containing Cs^+ in PC show the some suppression of dendrite formation. It is a good agreement with Ding's previous report.[1,2] The SEM images show microstructures with small spherical structures that correlate well with the NMR results. However, from the best our knowledge, the SHES effect is not applicable for the system where non-equilibrium deposition process takes place, causing overpotentials in a cell. We postulate that there should be other factor that controls the morphologies of Li microstructures, for instance formation of SEI layer. The SHES effect was not observed with KPF_6 in EC:DMC/ PC and $CsPF_6$ in EC:DMC due to the higher reduction of K^+ and Cs^+ on the Li metal surface. Therefore, we believe the SHES deposition mechanism is not applicable for the system.

We illustrate a possible scenario of the dendrite growth mechanism based on our observations under different SEI layer conditions under the assumption where SHES effect plays a significant role. As the SHES mechanism has suggested the prevention of the formation of a dendritic morphology, we propose that the effectiveness of the mechanism can be maximized with a uniform SEI layer. To gain clear insight into the effectiveness of SEI layer and the role of overpotential with the SHES effect, future work is needed, such as adding the additives (FEC, VC etc.) or using Li-M alloys.

3.5 References

1. F. Ding, W. Xu, G. L. Graff, J. Zhang, M. L. Sushko, X. Chen, Y. Shao, M. H. Engelhard, Z. Nie, J. Xiao, X. Liu, P. V. Sushko, J. Liu and J. G. Zhang, *J. Am. Chem. Soc.*, 2013, **135**, 4450-4456.
2. F. Ding, W. Xu, X. Chen, J. Zhang, Y. Shao, M. H. Engelhard, Y. Zhang, T. A. Blake, G. L. Graff, X. Liu and J.-G. Zhang, *J. Phys. Chem. C*, 2014, **118**, 4043-4049.
3. D. Aurbach, Y. Ein-Ely and A. Zaban, *J. Electrochem. Soc.*, 1994, **141**, L1-L3.
4. K. Xu, *Chem. Rev.*, 2004, **104**, 4304-4117.
5. Y. S. Cohen, Y. Cohen and D. Aurbach, *J. Phys. Chem. B*, 2000, **104**, 12282-12291.
6. D. Aurbach, *J. Power Sources*, 2000, **89**, 206-218.
7. K. Hayash, Y. Nemoto, S. Tobishima and J. Yamaki, *Electrochim. Acta*, 1999, **44**, 2337-2344.
8. O. Crowther and A. C. West, *J. Electrochem. Soc.*, 2008, **155**, A806-A811.
9. S. Chandrashekar, N. M. Trease, H. J. Chang, L.-S. Du, C. P. Grey and A. Jerschow, *Nat. Mater.*, 2012, **11**, 311-315.
10. H. J. Chang, N. M. Trease, A. J. Ilott, D. Zeng, L. S. Du, A. Jerschow and C. P. Grey, *J. Phys. Chem. C (Accepted)*, 2015.
11. R. Fong, U. Vonsacken and J. R. Dahn, *J. Electrochem. Soc.*, 1990, **137**, 2009-2013.
12. S. H. Lee, *J. Phys. Chem.*, 1996, **100**, 1420-1425.
13. S. H. Lee and J. C. Rasaiah, *J. Chem. Phys.*, 1994, **101**, 6964.
14. H. Ohtaki, *Pure & Appl. Chem.*, 1987, **59**, 1143-1150.
15. S. K. Jeong, M. Inaba, Y. Iriyama, T. Abe and Z. Ogumi, *Electrochim. Acta*, 2002, **47**, 1975-1982.
16. Y. Matsuda, M. Ishikawa., S.Yoshitake and M. Morita, *J. Power Sources*, 1995, **54**, 301-305.

17. C. W. Bale, *J. Phase Equilibr.*, 1989, **10**, 262-264.

18. S. S. Zhang, *J. Power Sources*, 2006, **162**, 1379-1394.

19. Z. Li, J. Huang, B. Yann Liaw, V. Metzler and J. Zhang, *J. Power Sources*, 2014, **254**, 168-182.

20. R. Bhattacharyya, B. Key, H. Chen, A. S. Best, A. F. Hollenkamp and C. P. Grey, *Nat. Mater.*, 2010, **9**, 504-510.

Chapter 4

In situ MRI observation of variations in the ionic concentration of the electrolyte during growth of Li microstructures

Abstract

Magnetic resonance image (MRI) has been performed to study the evolution of electrolyte in the vicinity of the electrolyte-electrode interface during current flow. Two different electrochemical conditions (high current density of 1.26 mA/cm^2 and low current density of 0.32 mA/cm^2) were used in symmetric cells containing a mixture of 1M $LiPF_6$ in EC: DMC and 5 wt % polymethyl methacrylate (PMMA). In situ MRI measurement allows us to capture simultaneous changes in the electrolyte concentration around Li microstructures under working conditions. Sand's time theory is adopted to investigate the relationship between dendrite formation and electrolyte concentration.

4.1 Introduction

Over the past 40 years, various models have been proposed to describe the conditions required for the onset and proliferation of dendrite growth in electrochemically grown metal systems. Of note are three models that can be classified by the factors they purport to contribute to the onset, growth rate, and morphology of metal deposition as discussed in Chapter 1: (1) the Barton and Bockris model[1, 2], in which overpotentials are related to surface diffusion, (2) diffusion-limited Brownian simulations[3, 4], where the sticking coefficient and the concentration of particles in the electrolyte solution are considered to predict the morphology of electrodeposition and (3) electromigration-limited models[5] developed by Chazalviel.

In the first two models, dendrite growth is based on the diffusion-controlled mechanism, while the Chazalviel model explores dendrite growth triggered by changes in the electrolyte concentration at the surface of the electrode.[5] Chazalviel predicts two different behaviors in the ionic concentration gradient; at low and high current density. At low current density the concentration gradient in the electrolyte reaches a steady state, resulting in a stationary ion distribution and potential in the cell, with no dendrite growth expected. In contrast, at high current density, the concentration continuously depletes in the vicinity of the negative electrode until eventually the anion concentration drops to zero. The excess of positive charge locally violates charge neutrality producing a large space charge and electric field at the electrode. The large electric field results in initiation and unavoidable dendrite growth.

For a given cell geometry and composition, the Chazalviel model[5] defines a critical current density (J^*) which marks the boundary between low and high current behavior. J^* is determined by the initial electrolyte concentration (C_0), the ambipolar diffusion coefficient (D) and the distance between the electrodes (L), and is given by,

$$J^* = \frac{2eC_0D}{t_{\mathrm{a}}L}, \tag{4.1}$$

where t_a is the transport number for the anion and e is the electronic charge (= 1.60 $\times 10^{-19}$ C). Furthermore, the time required for the anion concentration to drop to zero at the negative electrode for a given current density (J), termed Sand's time (τ_s), is also defined,

$$\tau_s = \pi D \left(\frac{C_0 e}{2Jt_a}\right)^2 \tag{4.2}$$

Brissot *et al.* measured the ionic concentration map experimentally in a symmetric Li cell with a PEO (polyethylene oxide) separator in order to validate the Chazalviel model.[6-8] They demonstrated that the onset time of dendrite growth at high current density is in good agreement with the predicted Sand's time. However, Brissot's later observations showed clear evidence of dendrite growth even at low current densities below J^*.[8, 9] They proposed that the non-uniformity of the electrode surface can cause variations in the local current density in the vicinity of the electrode. Park *et al.* found Sand's time to be inversely proportional to the temperature of the cell (using a Li symmetric cell with $LiPF_6$ electrolyte dissolved in a 1:1:1 volume ratio mixture of EC: DMC: EMC).[10] The dependence of Sand's time on measurable properties of a given cell allows it to be used to predict the onset of dendrite growth. Methods that can directly measure dendrite growth *in situ* can thus provide a route to validate this model and gauge the importance of the changing ionic concentration in governing dendrite growth.

The use of MRI techniques by Chandrashekar *et al.* demonstrated that chemical shift imaging (CSI) in particular could be used to reveal the location of different types of Li microstructures as a result of charging in a Li metal symmetric cell.[11] The extra spatial resolution provided further evidence of the peak assignment, revealing dendritic Li features to have a narrow range of chemical shifts near 270 ppm, while mossy microstructures have broader peaks covering a large frequency range from 262 ppm to 274 ppm. These shift ranges depend on the orientation of the battery, with the quoted ranges specific to batteries oriented with the face of the electrodes perpendicular to the external field. These effects are discussed further in Chapter 1. Recently, *in situ* MRI approaches have been extended to study electrolyte concentration gradients in batteries. Klett *et al.* reported 1D electrolyte concentration gradients in Li symmetrical cells containing 1M $LiPF_6$ in EC: diethylene carbonate (DEC) mixed with 15 wt %

poly(methyl methacrylate)(PMMA).[12] While applying current in the range from 30 μA to 50 μA [0.24 mA cm^{-2} to 0.40 mA cm^{-2}], a gradual buildup in the concentration gradients was observed. They utilized the electrolyte imaging profiles to analyze quantitatively physical constants of diffusivity and Li^+ transport number within an electrochemical transport model. Klamor *et al.* performed *in situ* ^{7}Li NMR imaging to study the formation of the SEI layer in a Li/ nano-Si-graphite composite battery cycled at a constant current of 20 μA [0.07 mA cm^{-2}].[13] They observed local changes in the ionic concentration at the interface between electrode and electrolyte, suggesting partial decomposition of electrolyte components during discharge. The above two studies[12, 13] provide detailed information about the evolution of concentration gradients in the electrolyte during cycling, but did not make any attempt to correlate these with changes occurring at the electrodes, such as those associated with Li deposition and microstructure formation.

Here we demonstrate a combined MRI study of the ^{7}Li electrolyte, ^{7}Li metal, and ^{1}H components of the electrolyte in symmetric Li metal cells charged *in situ* under a range of applied currents. This approach allows us to directly correlate the growth of dendrites and other types of microstructure with changes in the electrolyte concentration gradient. Simple analysis was performed to investigate the accuracy of the theoretical Sand's time and validate the actual impact on the dendrite growth in this system. We demonstrate that accurate estimations of the start time of dendrite growth can be achieved using Chemical Shift Images of the ^{7}Li metal signal, and compare these times to the theoretical Sand's Time along with experimental estimates of the electrolyte depletion from 1D ^{7}Li electrolyte images. Our data shows that Li microstructure grows from the beginning of charge in cells at every current used, although this only develops into dendritic growth at a critical point. The results indicate that Sand's time provides a good estimate of the experimental onset time of dendrites at high current densities but deviate significantly at low currents, suggesting that other mechanisms are more important at low current densities.

4.2 Experimental

4.2.1 Sample preparation

Electrochemical cells were prepared in home-built cells fitted inside of a 15 mm NMR glass tube and consisted of two electrodes of metallic lithium (diameter of 6.5 mm, Aldrich 99.9%) separated by an approximately 8 mm gap filled with electrolyte. The electrolyte is 1 M $LiPF_6$ in 1:1 by volume Ethylene Carbonate (EC): Dimethyl Carbonate (DMC) (Novolyte) mixed with 5 % poly(methyl methacrylate) (PMMA). The PMMA was added in order to reproduce experimental protocol from the literature[12, 13], although 5% was found to be the upper limit before the solution reached saturation under ambient conditions (15% PMMA is reported in the other MRI papers[12, 13]). The addition of PMMA increases the viscosity and decreases the volatility of the electrolyte solution, which reduces the impact of convection effects in the cells without a spacer, and helps prevent leakage of the electrolyte during the experiments. The electrodes were connected to an external copper wire for *in-situ* MRI measurement. All cells were prepared in an argon glove box (O_2 and H_2O < 0.2 ppm), sealed with wax, and immediately transferred to MRI for imaging.

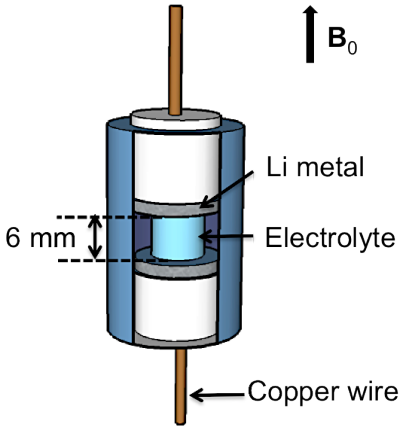

Figure 4.1 Schematic of the cell used for *in situ* MRI.

Electrochemical cycling was performed using a Biologic VSP potentiostat. Six different cells were prepared and each of them was charged at a constant current in one direction. Currents of 50 μA (0.16 mA/cm^2), 100 μA (0.32 mA/cm^2), 160 μA (0.51 mA/cm^2), 240 μA (0.76 mA/cm^2), 320 μA (1.01 mA/cm^2) and 400 μA (1.26 mA/cm^2) were used. These currents were chosen to span either side of the critical current density for the cell, $J^* = 0.63$ mA/cm^2. This value of J^* was calculated based on Eq. 4.1 where $C_0 = 6.02 \times 10^{20}$ cm^{-3}, L = 0.8 cm, D = 1.73×10^{-6} cm^2 s^{-1}, and $t_a = 0.65$. This value for D is taken from the average of the experimentally measured diffusion coefficients for the anion ($D_a = 2.26 \times 10^{-6}$ cm^2 s^{-1}) and the cation ($D_c = 1.20 \times 10^{-6}$ cm^2 s^{-1}), while t_a is calculated from D_a/ D_a+D_c. The current was applied in the direction from the bottom electrode (positive electrode) to the top electrode (negative electrode). Because the Li cells used are symmetric, we use the terms negative electrode (top electrode) and positive electrode (bottom electrode) where Li deposition and Li stripping are occurring, respectively.

4.2.2 MRI

All MRI and NMR experiments were performed on a Bruker Ultrashield 9.4 T Avance I spectrometer containing a Bruker Micro2.5 gradient assembly and operating at 400.13 MHz for ^{1}H and 155.51 MHz for ^{7}Li. A Bruker Micro2.5 imaging probe was used to collect all of the data, with a Bruker WB40 25 mm i.d. ^{1}H^{7}Li coil insert for the ^{7}Li and ^{1}H experiments, and a Bruker WB40 25 mm i.d. ^{1}H^{19}F coil insert for the ^{19}F diffusion experiments.

The cells were aligned in the magnet such that B_0 (and the z axis of the gradients) was aligned perpendicular to the face of the electrodes (as illustrated in Figure 4.1). The cells were centered in the coil, the excitation profile of which was found to be approximately 15 mm, thus ensuring uniform excitation over all of the components in the cell. Imaging experiments could be performed separately on the ^{7}Li metal and electrolyte signals because of their significant chemical shift difference, arising from the 261 ppm Knight shift of ^{7}Li metal.[14, 15]

Three types of images were collected during the cycling of the cells: a 1D ^{7}Li z-projection image of the electrolyte to give information on the concentration profile, a ^{7}Li metal chemical shift image (CSI) to observe changes in the bulk Li metal, and a 2D ^{1}H projection image of the

organic species in the electrolyte to give further information on the changes occurring in the electrolyte region of the cell. The 1D ^{7}Li electrolyte image was acquired with a spin echo sequence in the *z* direction, with a field of view (FOV) of 4 mm and a nominal resolution of ca. 16 μm. A total echo time (TE) of 3.5 ms was used with a repetition time (TR) of 8 s and 128 averages collected, giving a total experiment time of ca. 17 mins. For the metal spin echo CSI, the chemical shift information was preserved during the readout while spatial encoding was performed with 32 phase increments in the *z* direction with a FOV of 30 mm and nominal resolution of 940 μm. With TR = 200 ms, TE = 0.65 ms and 192 transient averages collected, the total experiment time was ca. 21 mins. We note that although the spatial resolution in the metal CSI is not particularly high, it is sufficient to serve the purpose of separating the signal from each electrode in the cell while allowing images with high signal to noise ratio to be collected in a short amount of time, making the experiment amenable to *in situ* measurements. The 2D ^{1}H spin echo projection image was collected with 32 phase encode points along the *x* direction with a FOV of 15 mm and nominal resolution of 470 μm. A readout gradient was used in the *z* direction with a FOV of 40 mm and nominal resolution of 78 μm. With TR = 10 s, TE = 6.08 ms and a single scan collected, the total experiment time was ca. 5 mins.

The diffusion coefficients of the cation (^{7}Li) and anion (^{19}F) in the electrolyte were measured using a spin echo diffusion experiment with a fixed echo time. The ^{1}H T_1 and T_2 relaxation times of the EC and DMC solvent molecules in the electrolyte were measured using inversion recovery and cpmg pulse sequences, respectively. The measurements were repeated on samples with and without Li salt and were measured at room temperature (RT, ≈20°C) and at 40°C.

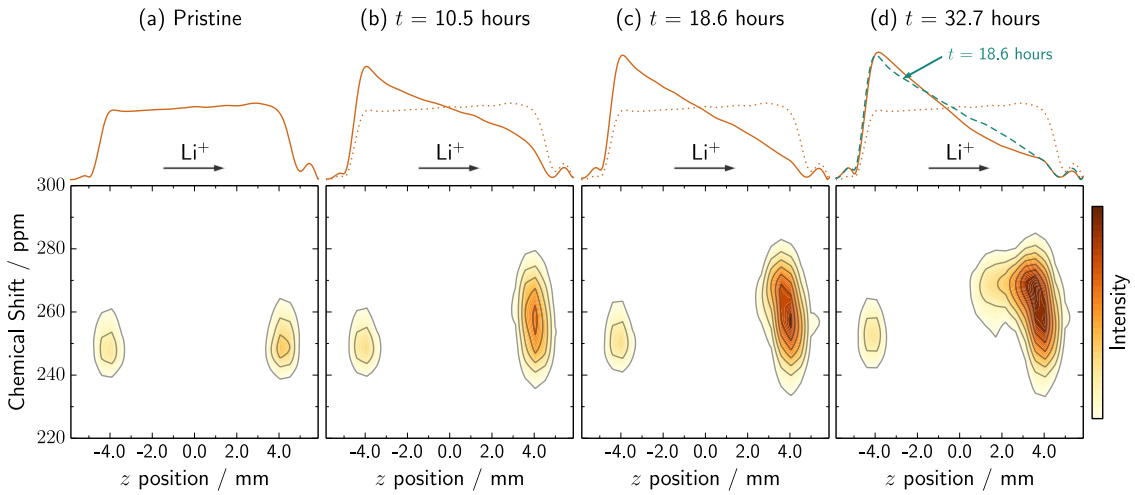

Figure 4.2 Time series showing evolution of the ^{7}Li electrolyte concentration profile (top) and the ^{7}Li chemical shift image of the metal (bottom) for the series cycled at 240 μA.

4.3 Results and Discussion

Figure 4.2 shows examples of the ^{7}Li images acquired during the charge process of the cells, with the ^{7}Li electrolyte concentration profile (top) from the series of z projection spin echo images, and the chemical shift images of the ^{7}Li metal (bottom), from the cell charged with a current of 240 μA (0.76 mA/cm^2) for 32.7 hours. Before applying current, the lithium concentration profile at equilibrium shows an almost rectangular shape, associated with a uniform distribution of Li ions across the cell (Figure 4.2a). We observe that the salt concentration at the top electrode is slightly higher. This has previously been ascribed to convection effects.[12] In principle the edges of the electrolyte profile may be expected to be perfectly rectangular but susceptibility effects near the surface of the Li metal,[16] difficulties ensuring the Li metal electrodes remain completely flat (as discussed later), and inhomogeneities in the B_1 field near the electrodes[16-18] can lead to this non-ideal shape. The associated CSI image of the pristine cell (Figure 4.2a, bottom) shows peaks for the Li metal electrodes at the top (right) and the bottom (left) of the cell, with approximately equal intensities and a chemical shift of ca.

250 ppm. This large chemical shift is typical of Li metal oriented perpendicular to $\boldsymbol{B}_0$,[11, 16, 19] and is caused by a combination of the Knight shift (261 ppm in ^{7}Li metal) associated with the conducting electrons in the metal, and orientation-dependent bulk magnetic susceptibility effects[16, 20] caused by the large paramagnetic susceptibility of Li metal ($\chi_{volume} = 24.1 \times 10^{-6}$).[21]

After the current has been applied for 10.5 hours (Figure 4.2b), the concentration profile decreases noticeably in the vicinity of the negative electrode and increases at the positive electrode. The metal CSI shows a simultaneous increase in intensity over a broad range of shifts centered at ca. 260 ppm at the negative (top) electrode. This peak, upfield from the bulk metal peak, is associated with mossy-type microstructures[11] that have formed at the surface of the Li metal electrode during the initial stages of charging. This is in stark contrast to the case where the Li plates smoothly on the surface of the electrode, where no change in the metal peak should be observed due to the skin effect, as discussed previously.

The linear decrease of the electrolyte signal across the cell continues after the charge passed for 18.6 hours, while the microstructure peak at 260 ppm also continues to grow in intensity (Figure 4.2c). However, a new signal at 270 ppm also emerges in the metal image, becoming much more pronounced and extending out appreciably (by 2-3 mm) from the surface of the electrode by the end of charging (Figure 4.2d). The chemical shift[11] and spatial extent of this new environment prove that it corresponds to dendritic Li metal, growing into the space between the electrodes. There is a corresponding drop in the Li^+ salt concentration in the region that the dendrites grow into (as shown by the difference with the overlay of the $t = 18.6$ hours data).

These results show that the chosen MRI experiments are able to track changes in both the Li salt concentration profile and the growth of different types of Li microstructure on the surface of the electrode. It can be seen that the concentration of the salt drops in the vicinity of the negative electrode as the Li metal microstructures form, first as a mossy-type structure with a characteristic shift at 260 ppm, and then as dendritic structures that extend out appreciably from the surface of the electrode, with a 270 ppm shift.

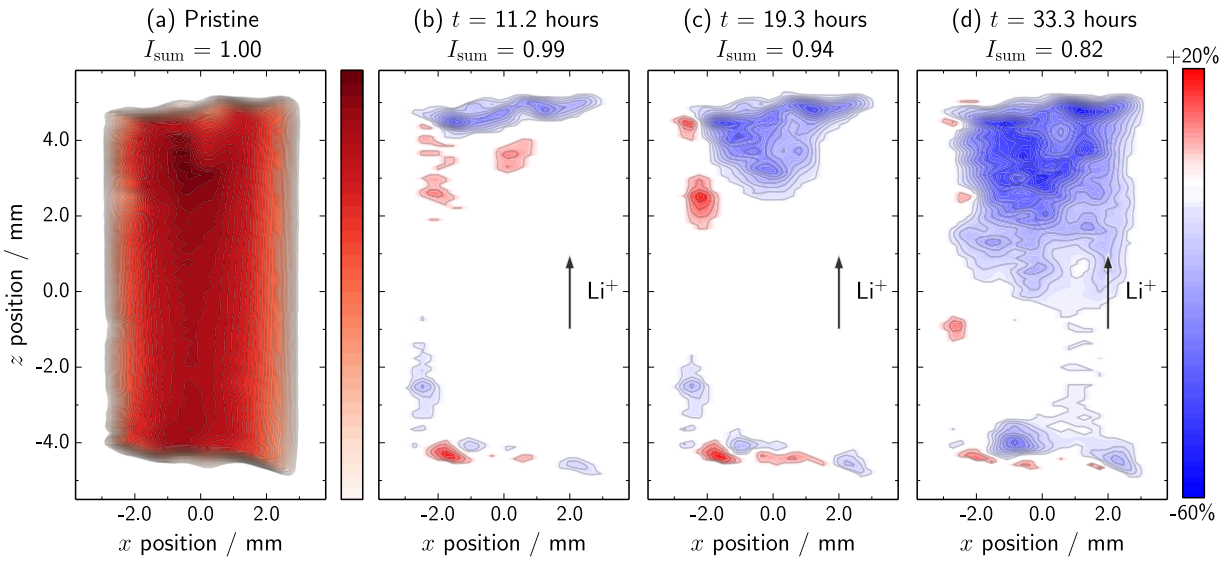

Figure 4.3 ^{1}H Images from the cell cycled with a current of 240 µA. (a) The 2D spin echo image of the pristine cell and (b-c) difference plots between the images acquired at later times in the cycling and the pristine image. Red regions show an increase in intensity while blue show a decrease. The normalized integrated signal intensity of each image, I_{sum}, is also shown.

The 2D ^{1}H MRI experiments conducted on the same cell as shown in Figure 4.2 track the ^{1}H signal from the solvent components in EC and DMC, showing the impact that the microstructure growth has on the electrolyte region in the cell. To investigate the variation of ^{1}H signal more clearly, the 2D images acquired at different charge stages were subtracted from the pristine image. The ^{1}H image shows there to be a uniform distribution of electrolyte across the pristine cell (Figure 4.3a), although some regions of fluctuating intensity are visible on the edge of the cell at x = -3 mm that can be associated with poor wetting of the walls of the Teflon cell. When a constant current of 240 µA is applied, the ^{1}H image profile displays a significant reduction of the signal intensity (blue) at the top electrode (Figure 4.3b-c). After application of the current for 33.3 hours, the regions with reduced intensity develop further towards the positive electrode, matching well with the region where Li dendrites form (Figure 4.3d). There is extensive depletion in the electrolyte once a significant amount of dendrites has grown (Figure 4.3c-d). There is a corresponding, but smaller decrease in the ^{7}Li salt signal (for the equivalent times in 4.3b,c,d they are at 1.00, 0.98 and 0.92 fractions of the pristine signal), although the role of the Li is more complicated as it is being simultaneously plated and stripped from the

respective electrodes. In addition, increased ^{1}H intensity (red) is observed at some locations in the electrolyte and we assume that this is caused by regions of the electrolyte that contained bubbles that are later filled.

We ascribe the reduced ^{1}H intensity to four effects: (i) changes in the proton T_1 and T_2 relaxation times due to changes in the Li^+ concentration and/or temperature leading to some saturation of the MR signal in the fixed-TR experiments, (ii) spatial displacement of the electrolyte by the microstructure, (iii) local inhomogeneities in the radiofrequency (rf) field around the lithium microstructure and dendrites that reduce the excited/detected signal intensity, and (iv) consumption of the electrolyte through formation of SEI layer at the electrode surface. Strong magnetic susceptibility effects are expected in the regions around the microstructure[22] but the induced chemical shift differences should be refocused in the spin echo sequence used and so these effects can be ignored.

Measurements of the proton relaxation times in EC and DMC (Table 4.1) show the quantities to increase by a factor of approximately 1.5 on increasing the temperature from room temperature to 40°C. Likewise, when the concentration of $LiPF_6$ in the EC:DMC mixture is reduced from 1M to zero, the proton relaxation times increase by a factor of approximately 2. These increases, especially those in T_1, are expected to have a significant effect on the acquired image intensity (results from signal calculations based on the experimental conditions used are shown in Table 1). While the cells are cycling, the temperature in the regions around the electrodes will increase[23], and there is a simultaneous change in the Li^+ concentration in those regions, as shown by the Li electrolyte images in Figure 4.2. These combined changes can therefore explain the reduced ^{1}H image intensity in the vicinity of the top electrode in Figure 4.3b.

	Room temperature			40°C		
	T_1	T_2	Signal*	T_1	T_2	Signal*
1M LiPF6			**0.98**[#]			**0.94**[#]
EC	2.00	1.78	**0.99**	2.94	2.71	**0.96**
DMC	2.80	2.55	**0.97**	3.92	3.74	**0.92**
EC:DMC			**0.82**[#]			**0.73**[#]
EC	5.61	5.02	**0.83**	7.58	6.67	**0.73**
DMC	5.92	5.40	**0.81**	7.64	7.11	**0.73**

Table 4.1 Measured T_1 and T_2 relaxation times for EC and DMC in $LiPF_6$/EC:DMC mixture and in EC:DMC alone.*Calculated relative signal intensity for spin echo experiment with TE=6.08ms and TR= 10.00s. [#]Average of EC and DMC.

The reduced ^1H intensity can also arise from the spatial displacement of electrolyte by the microstructure, although this change can only lead to local variations and should not result in the global decrease in the ^1H image intensity that is observed. However, inhomogeneities in the rf field in the vicinity of the microstructure are also expected to play an important role, and will reduce the total observed signal in the spin echo experiment. These factors explain why the region of reduced ^1H signal intensity is well matched with the region of dendrites extending out about 2~3 mm from the top electrode in Figures 4.3c,d.

The final contributing factor to the reduction in ^1H image intensity is the consumption of the EC and DMC carbonate molecules due to the formation of the SEI layer[24] (if the carbonate molecules move from being in the liquid to solid phase they will not be observed fully in the image). Because of the other factors affecting the ^1H image intensity, it is difficult to assess this

contribution. Further work is required to completely quantify the other effects in order to separate effects due to SEI formation.

Overall, it is interesting to note that the 2D ^{1}H images do reveal the changes in intensity of electrolyte, but also the location of Li microstructures. In this manner, ^{1}H images can be a potential tool for *in situ* battery NMR to investigate changes in the electrolyte and electrodes under different conditions.

Returning to the analysis of the ^{7}Li electrolyte and metal images, simple metrics have been developed in order to allow a comparison between the behavior of the electrolyte concentration gradient and the onset times of dendritic growth for the samples charged at different rates. For the metal, the signal for the top electrode in the CSI was deconvoluted into peaks at 250, 260 and 270 ppm, approximately corresponding to pristine Li metal, mossy microstructure and dendritic microstructure, respectively.[22] The time-dependence of the integrated area of the 270 ppm peaks were used as the metric for dendrite growth. To quantify the electrolyte depletion, a single position in the electrolyte profile close to the top electrode was selected and the intensity followed as a function of time.

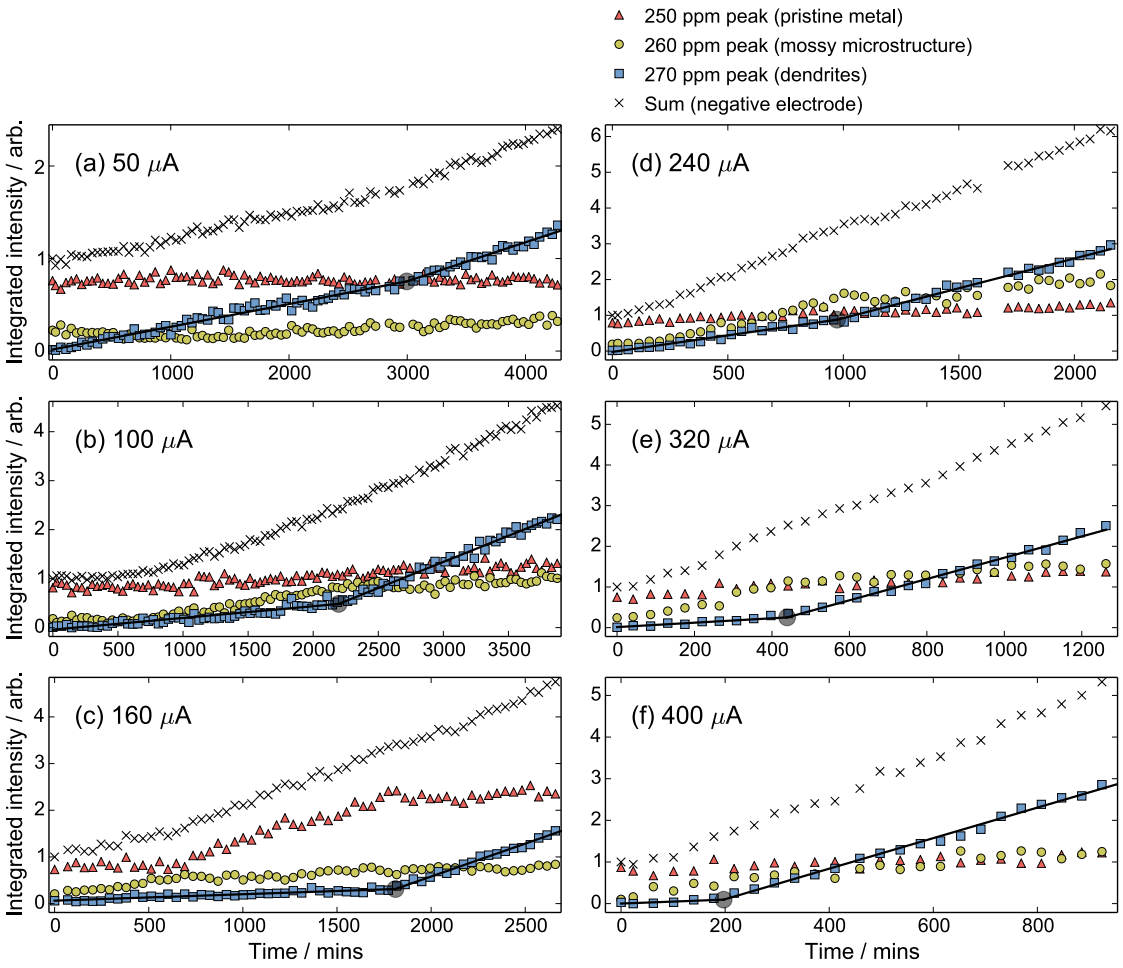

Figure 4.4 Plots showing changes in the integrated intensity of the metal peak used to quantify dendrite growth and Sand's time from the chemical shift images. The signal from the top electrode is deconvoluted into three peaks at 250 ppm for Li bulk metal, 260 ppm for mossy structures, and 270 ppm for dendritic structures, with the integrated intensity of the fitted peaks plotted here. Each series is normalized to the sum of the integrated area of peaks at t=0. The integrated intensity of the peak at 270 ppm was fit to two straight lines for the points above and below the discontinuity in the slopes, with the intersection of those lines circled in each plot.

Figure 4.4 and 4.5 depict the result of the signal quantifications for the dendritic growth and electrolyte depletion as a function of time. Figure 4.4 shows changes in the integrated area of the deconvoluted metal peaks at 250 ppm, 260 ppm and 270 ppm, and their sum, for the top electrode in the cells charged each current rate. The change in intensity of the bulk metal peak at

250 ppm in every cell stays almost constant, except for the cell charged at 160 μA, where the 250 ppm peak increases from the start of charge. In this case the chemical shift of the growing microstructure must be close to the bulk metal peak and so not easily distinguished from it. In each cell, the intensity of the dendrite and mossy microstructure peaks (and the total intensity) start to increase as soon as the current is applied. This increase is ascribed to the growth of mossy microstructure on the surface of the Li electrode, which always starts from the beginning of cycling, it being difficult to completely separate the contributions from the broad peaks at 260 ppm and 270 ppm. Nevertheless, at some discrete time in each of the series there is a steep increase in the growth of the fitted 270 ppm peak, marking the switch from the growth of mossy to dendritic structures (we have confirmed that this also correlates with an increase in the spatial extent of the electrode in CSI, consistent with the onset of dendrite growth but estimates based on this observable are far less robust). The intersection (circular marker) of lines fit to the data points above and below this discontinuity gives an accurate and robust estimate of the time when the first dendrites grow in each of the cells. It is interesting to note that prior to this time in the curves, the rate of microstructure growth (gradient of the lines) does not correlate with the applied current, whereas afterwards, when dendrites are growing, the rate of growth is proportional to the applied current. This indicates that once dendrites form, that most, or all of the deposited lithium is plating in dendritic forms. When only microstructure is growing, smooth deposition may also be occurring and it seems the exact proportion of each type (and therefore the relative increase in signals at different chemical shifts) may depend on the cell construction and conditions rather than just the applied current.

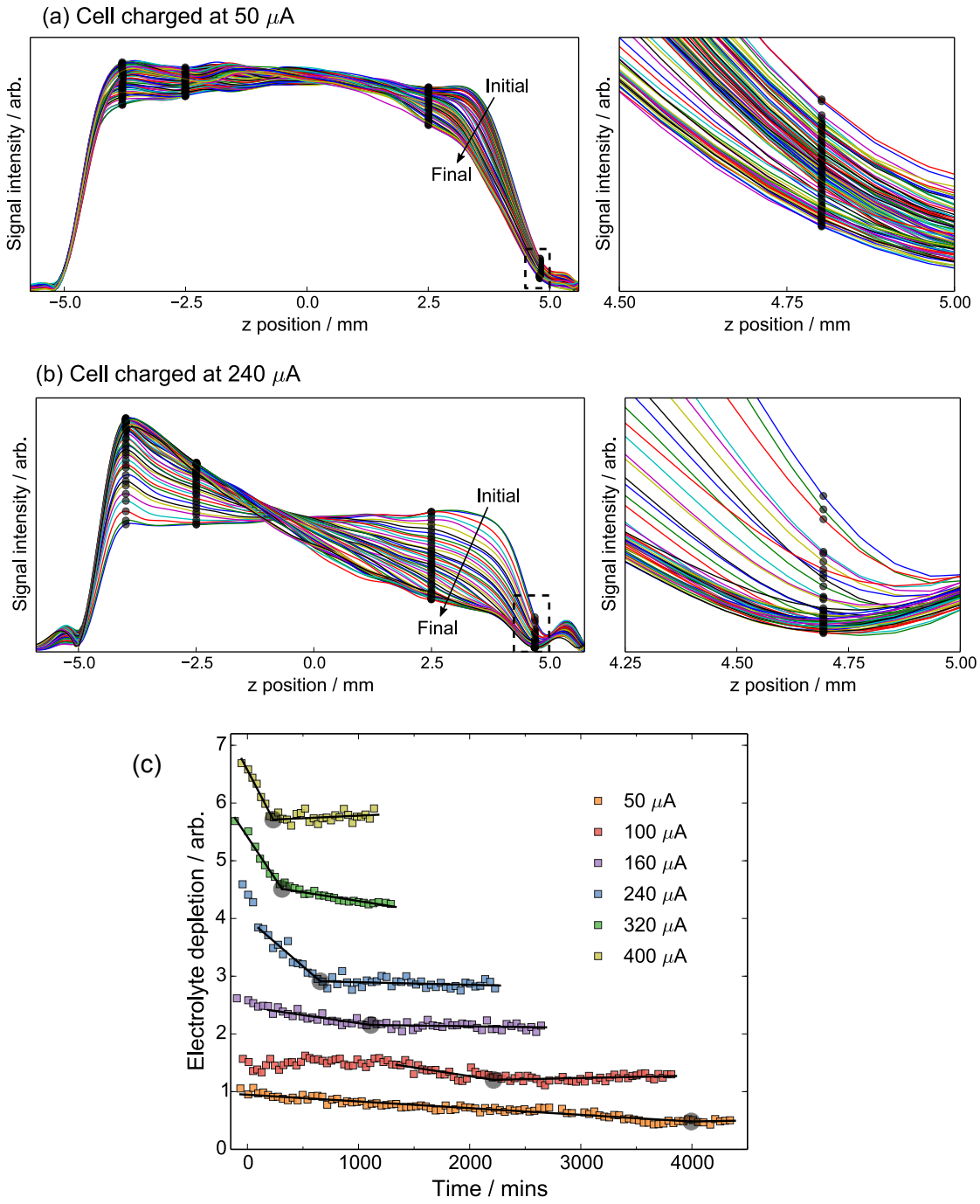

Figure 4.5 Quantification results for electrolyte depletion (as described in main text) measured from the ^{7}Li electrolyte imaging for cells charged at (a) 50 μ A, (b) 240 μ A. The positions of several positions are marked near the bottom (ca. -5 mm) and top electrodes (ca. 5 mm) with the expanded region on the right hand side showing the region closest to the top electrode. (c) Extent of electrolyte depletion for the cells charged at each current. Straight-line fits were made to the points above and below the discontinuity in the slopes, with the intersection of those lines circled in each plot.

The Figure 4.5 shows depletion of the electrolyte characterized by the time evolution of the

intensity of a signal point in the image close to the top electrode. A position approximately 250 μm from the top electrode was chosen in Figure 4.5a and b. The point shown at ca. 4.75 mm in each series is enlarged and shown on the right hand side). The curves following the metric of electrolyte depletion also show a discontinuity; this is interpreted as the point where the electrolyte has been fully depleted near at least some part of the electrode. The Li electrolyte signal never becomes zero, this is because the ^{7}Li electrolyte image along *z* is a projection of the *x* and *y* directions and although the Li^{+} concentration may be completely depleted locally in some regions near the electrode, this does not occur over the full cross sectional area of the electrode which has a ca. 6 mm diameter. Full 3D imaging of the $^{7}Li^{+}$ in the electrolyte would be needed to observe local depletion in the electrolyte, but this is currently unfeasible due to the poor signal to noise ratio of these experiments. Furthermore, the curves in Figure 4.5c show that this metric is somewhat less effective at lower currents, where the discontinuity is far less distinctive.

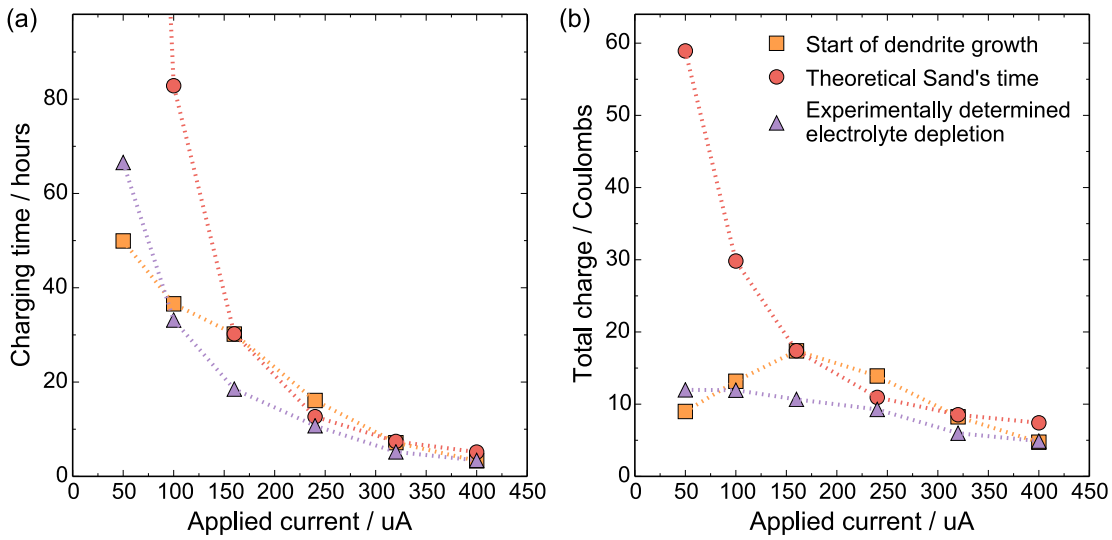

Figure 4.6 (a) Plot of the theoretical Sand's time and the experimentally measured start of dendrite growth and electrolyte depletion (b) the same data, now plotted against the total charge applied during the cycling.

The two sets of metrics are compared in Figure 4.6, plotted alongside the theoretical Sand's time calculated for the cells, following Eq. 4.2. It can be seen that there is a reasonable agreement between the values for the cells charged at currents above 240 μA, while at lower currents dendrite growth is initiated long before the theoretical Sand's time, and before electrolyte depletion is measured in the cell at 50 μA (Figure 4.6a). While we acknowledge the considerable uncertainty in the measured electrolyte depletion, the deviation from the theoretical value of Sand's time is significant and neither metric follows the J^2 dependence of the theoretical Sand's time. This deviation is further amplified when comparing the total charge applied to each cell (i.e. charge = current applied x time) at the time indicated by each metric (Figure 4.6b). On this scale it is clear that experimentally we observe a maximum dendrite-free charging capacity of the cell at intermediate currents around 160 μA. In cells charged above this value the onset of dendrite growth correlates reasonably well with the theoretical and experimentally observed time at which the electrolyte is depleted at the surface of the negative electrode, suggesting that this is the dominant mechanism triggering dendrite growth at high currents. At low currents, the experimentally determined onset of dendrite growth deviates not only from the theoretical Sand's time values, but, more significantly, from the overall prediction

from the theory that at lower currents a higher charge should pass before dendrites start to grow in the cell. This is a strong indication that there is a second mechanism for the initiation of dendrite growth that dominates at low currents that is not directly related to the depletion of the electrolyte at the surface of the electrode.

Our observations would seem to preclude mechanisms involving the surface roughness of the electrode because in every case we observe microstructure growth from the beginning of charge and this rough structure would provide the necessary nucleation point for further dendrite growth if this was the important mechanism for the onset of runaway dendrite growth. Alternatively, the nucleation point for the dendrites could be on the original surface of the metal, but the roughness of this surface should remain unchanged during the experiment and so a reasonable explanation is still needed to explain why there is a sudden change in the type of microstructures being grown. The Barton and Bockris model[1] can explain why the mossy-type microstructure continues to grow once it forms initially as this is when the diffusion behavior of the cations in the regions close to the tips of the microstructure becomes spherical. However, this does not explain why there is a sudden switch from mossy to dendritic growth. To form parallels with the diffusion-limited Brownian simulations[3, 4], this switch can be interpreted as moving from high to very low-density microstructures. It would therefore signal a sudden decrease in the penetration of the cations into the existing microstructure before they deposit, caused by either an increase in the effective "sticking coefficient", or a reduction in the local diffusion rate or cation concentration. The latter two are influenced by the local composition of the electrolyte and will behave in a manner similar to the anion depletion described by Chazaviel's model. Meanwhile, the sticking coefficient depends on the material properties of the surface and the overpotential.[25] While the properties of the Li metal itself cannot change, the SEI properties can, and any variation could influence the deposition of the cations on the surface, or the effective "sticking coefficient" of the system. The SEI is a passivating 5-50nm layer[26, 27] that forms on the surface of the electrode, acting like a solid electrolyte layer, permitting ion conduction from the bulk electrolyte region to the electrode surface. It is formed through spontaneous reactions of the different electrolyte components at the electrode surface, and its properties are thus sensitive to the electrolyte composition.[28-30] It is thought that a desirable SEI should be uniform and

homogeneous and that this can result in dendrite-free, smooth Li deposition on the metal surface. We do not observe appreciable periods of smooth Li deposition in the cells studied, but the SEI layer must also form at the surface of the growing microstructure (which is of the order of 1 μm in diameter, so around two orders of magnitude thicker than the SEI layer). As this is a continuous process, it is inevitable that the reaction will deplete the SEI ingredients in the electrolyte over time, eventually compromising SEI formation and it's beneficial properties. This could lead to a sudden change in the growth behavior of the microstructure and the initiation of dendritic growth, which will then propagate exclusively to the detriment of mossy-type growth. In this manner, the eventual growth of lithium dendrites on the Li metal anode is inevitable and will occur regardless of the charge rate due to continuous, irreversible SEI formation.

4.4 Conclusions

In situ ^{7}Li MRI is performed on both the electrolyte and lithium metal electrodes in symmetric lithium cells, allowing the behavior of the electrolyte concentration gradient to be studied and correlated with the type and rate of microstructure growth on the surface of the electrode. For this purpose, chemical shift images of the metal electrodes are particularly sensitive, enabling a clear distinction to be made between different types of microstructural growth occurring at the electrode surface and the eventual unidirectional dendrite growth between the electrodes. The chemical shift imaging shows that mossy types of microstructure grow close to the surface of the anode from the beginning of charge in every cell studied, while dendritic growth is triggered much later. The 2D ^{1}H images reveal the changes in intensity of electrolyte as well as the location of Li microstructures. It is interesting to point out that ^{1}H images can be used as a tool for *in situ* battery NMR. Simple metrics have been developed to interpret the different MRI data sets and compare results from a series of cells charged at different rates. The results show that at high charge rates, there is a strong correlation between the onset time of dendrite growth and the local depletion of the electrolyte at the surface of the electrode observed experimentally and by theoretical Sand's time models. A different mechanism of dendrite growth is observed at low currents and we postulate that this phenomenon is related to the depletion of components of the electrolyte that form the surface electrolyte interphase layer, preventing the formation of an effective SEI layer at the surface of the electrode and triggering runaway dendrite growth.

4.5 Reference

1. J. W. Diggle, A. R. Despic and J. O. M. Bockris, *J. Electrochem. Soc.*, 1969, **116**, 1503-1514.
2. J. L. Barton and J. O. M. Bockris, *Proc. R. Soc. London, Ser. A*, 1962, **268**, 485.
3. R. V. Magan and R. Sureshkumar, *J. Phys. Chem. B*, 2003, **107**, 10513-10520.
4. T. Witten and L. Sander, *Phys. Rev. Lett.*, 1981, **47**, 1400-1403.
5. J.-N. Chazalviel, *Phys. Rev. A*, 1990, **A 42**.
6. C. Brissot, M. Rosso, J.-N. Chazalviel and S. Lascaud, *J. Electrochem. Soc.*, 1999, **146**, 4393-4400.
7. C. Brissot, M. Rosso, J.-N. Chazalviel, P. Baudry and S. Lascaud, *Electrochim. Acta*, 1998, **43**, 1569.
8. C. Brissot, M. Rosso, J. N. Chazalviel and S. Lascaud, *J. Power Sources*, 2001, **94**, 212-218.
9. C. Brissot, M. Rosso, J. N. Chazalviel and S. Lascaud, *J. Power Sources*, 1999, **81**, 925-929.
10. H. E. Park, C. H. Hong and W. Y. Yoon, *J. Power Sources*, 2008, **178**, 765-768.
11. S. Chandrashekar, N. M. Trease, H. J. Chang, L.-S. Du, C. P. Grey and A. Jerschow, *Nat. Mater.*, 2012, **11**, 311-315.
12. M. Klett, M. Giesecke, A. Nyman, F. Hallberg, R. W. Lindstrom, G. Lindbergh and I. Furo, *J. Am. Chem. Soc.*, 2012, **134**, 14654-14657.
13. S. Klamor, K. Zick, T. Oerther, F. M. Schappacher, M. W. and and G. Brunklaus, *Phys. Chem. Chem. Phys.*, 2015, **17**, 4458-4465.
14. H. S. Gutowsky and B. R. McGarvey, *J. Chem. Phys.*, 1952, **20**, 1472-1477.
15. J. P. Marques and R. Bowtell, *Concepts Magn. Reson. B* 2005, **25B**, 65-78.

16. A. J. Ilott, S. Chandrashekar, A. Klockner, H. J. Chang, N. M. Trease, C. P. Grey, L. Greengard and A. Jerschow, *J. Magn. Reson.*, 2014, **245**, 143-149.

17. M. M. Britton, *Chemphyschem : a European journal of chemical physics and physical chemistry*, 2014, **15**, 1731-1736.

18. M. M. Britton, P. M. Bayley, P. C. Howlett, A. J. Davenport and M. Forsyth, *J. Phys. Chem. Lett.*, 2013, **4**, 3019-3023.

19. N. M. Trease, L. Zhou, H. J. Chang, B. Y. Zhu and C. P. Grey, *Solid State Nucl. Magn. Reson.*, 2012, **42**, 62-70.

20. A. Kubo, T. P. Spaniol and T. Terao, *J. Magn. Reson.*, 1998, **133**, 330-340.

21. D. Gugan, *Phys. Rev. B*, 1997, **56**.

22. H. J. Chang, N. M. Trease, A. J. Ilott, D. Zeng, L. S. Du, A. Jerschow and C. P. Grey, *J. Phys. Chem. C (Accepted)*, 2015.

23. N. Sato, *J. Power Sources*, 2001, **99**, 70-77.

24. D. Aurbach, E. Zinigrad, Y. Cohen and H. Teller, *Solid State Ionics*, 2002, **148**, 405-416.

25. M. Z. Mayers, J. W. Kaminski and T. F. Miller, *J. Phys. Chem. C*, 2012, **116**, 26214-26221.

26. E. Peled, *J. Electrochem. Soc.*, 1979, **126**, 2047-2051.

27. S. K. Jeong, M. Inaba, Y. Iriyama, T. Abe and Z. Ogumi, *Electrochim. Acta*, 2002, **47**, 1975-1982.

28. D. Aurbach, Y. Gofer, M. B. Zion and P. Aped, *J. Electrochem. Soc.*, 1992, **339**, 451-471.

29. D. Aurbach, E. Zinigrad, H. Teller and P. Danb, *J. Electrochem. Soc.*, 2000, **147**, 1274-1279.

30. D. Aurbach, *J. Power Sources*, 2000, **89**, 206-218.

Chapter 5

Time-resolved 2D and 3D x-ray imaging of lithium microstructure growth, removal and pitting on lithium metal electrodes

Abstract

The 3D structure of electrodeposited lithium dendrites in lithium metal symmetrical cells with liquid electrolytes has been characterized using time-resolved, non-destructive synchrotron X-ray tomography. Electrodeposited lithium microstructures, described as dendrites, moss or high surface area lithium (HSAL) have been observed. The image sequences demonstrate that the growth of newly formed lithium microstructures occurs from both the base and the tip of the microstructures. Under reverse current the lithium microstructures are only partially removed before pitting of the bulk lithium occurs. The combination of NMR and SEM techniques also supports the tomography results; that there are always Li microstructures remaining on the surface even after the same amount of Li was transferred under the reverse current.

5.1 Introduction

Dendrite growth in Li batteries has been observed in many studies and there are two different growth models that have been proposed; tip-controlled growth and base-controlled growth. As discussed in Chapter 1.significant differences in the preferential growth location have been described in mechanical models such as the Barton and Bockris surface-tension model,[1] the Brownian statistical simulation model,[2] the Chazalviel and Rosso model[3, 4] and Yamaki model.[5] The Barton and Bockris model[1] describes the preferential growth location is at the tip of existing protrusions, where there is enhanced spherical diffusion around the tip as compared with the linear diffusion at the planar surface of the substrate. In the Brownian simulation model[2], when the deposition probability is low, there is an increased chance of forming dense structures while a high deposition probability results in the possibility of deposition at the tip of the existing protrusions, leading to dendritic structures. The Chazalviel and Rosso model[3, 4] states that the change in the electrolyte concentration triggers the onset of dendrite growth from the base.[6, 7] However, their mechanism is not clear to explain the observed growth at the base of Li dendrite. Yamaki *et al.*[5] suggested stress-assisted dendrite growth at the base due to cracks in the protective SEI layer on the surface of the Li anode. When the stress that caused by the accumulation of Li depositions underneath the protective layer is built up large enough, growth of dendrites will be initiated at the cracks.

Beside the proposed mechanical models, Kohl *et al.* experimentally observed dendrite growth from the tip, as well as from the base using *in situ* optical microscopy and *ex situ* SEM experiments.[8, 9] They explain the growth at the tip takes place due to the electrochemically active site of tips while the extrusion-based growth is thought to be a surface tension mechanism, which is suggested by Yamaki *et al.*[5] earlier indicating built-up stress caused by the solid electrolyte interface (SEI) layer. The deposition rate at the tip is significantly higher than at the sidewalls or base.

Electron microscopy has been used for 2D characterization of lithium microstructures but has usually required their prior removal from their as-grown environment.[10-14] NMR and MRI have been applied to explore dendrite growth *in situ*, quantifying and differentiating between

mossy and dendritic Li growth based on the shifts and intensities of the NMR signals.[15-17] However the resolution of MRI is typically limited to 100 μm, which does not allow for the elucidation of structural information for individual microstructures.[16] Recently, the 3D structure of energy materials such as carbon, lithium, solid oxide fuel cell electrodes has been characterized using synchrotron X-ray tomography.[18, 19, 20] Harry *et al.*[20] have reported the detection of Li microstructures in symmetric lithium-polymer-lithium cells cycled at 90°C using 3D synchrotron imaging. They observed that small crystalline contaminants were found underneath every growing dendrites in a lithium polymer cell indicating that contaminants may act as catalysts for dendrite growth. The majority of the tree-like dendrites were formed within the electrode, not the electrolyte, in the early stages of cycling. Only after subsequent cycling did the dendrites form in the electrolyte region and short-circuit the cell at the end of cycling. Also, a more recent study by Eastwood *et al.* characterized microstructures in Li symmetrical cells using the parallel-beam x-ray microtomography setup with an 0.45 μm effective pixel size and ~1 μm spatial resolution.[19]

In this study we apply non-destructive X-ray phase contrast tomography to characterize electrochemical Li cells using lithium metal (Aldrich, 99.9%) electrodes in 1 mm inner diameter Kapton capillaries, designed to enable electrodesposition of lithium with an unobstructed x-ray path under a 360° rotation. *In situ* X-ray tomography allows examination of microstructure growth in 3D at high resolution for the first time. The 3D, time-resolved direct imaging confirms that multiple growth locations occur both from the base and the top of the microstructures. Also, a pitted metal surface was observed after partial removal of the microstructures under reverse current. NMR and SEM results also show that there is always incomplete removal of Li microstructure after the same amount of Li was transferred under the reverse current. We propose that the multiple growth and removal mechanisms reflect the complexity of the lithium electrodeposition and dissolution process in Li batteries.

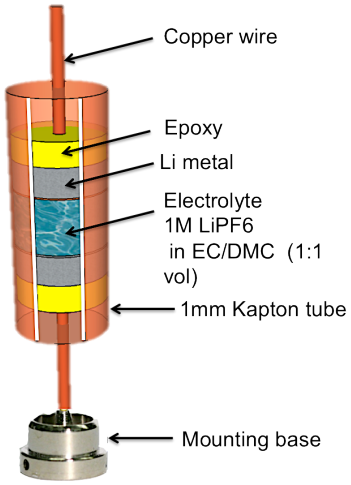

Figure 5.1 Schematic picture of the lithium symmetric cell, containing 1 M $LiPF_6$ dissolved in EC and DMC (1:1 %vol) electrolyte in a 1 mm Kapton tube mounted on the mounting base.

5.2 Experimental

5.2.1 Preparation for X ray tomography

Electrochemical cell samples were prepared inside a 1 mm diameter Kapton tube and consisted of two electrodes of metallic lithium (diameter of 650 µm) separated by an approximately 1.5 mm (±0.5) gap filled with electrolyte (1 M $LiPF_6$ in 1:1 by volume Ethylene Carbonate (EC): Dimethyl Carbonate (DMC), supplied by Novolyte), shown in Figure 5.1 All cells were prepared in an argon glove box (O_2 and H_2O < 0.1 ppm), sealed with an epoxy, and immediately transferred to the beamline for imaging.

Electrochemical cycling was performed using a Biologic VSP potentiostat. Two symmetrical cells (Sample 1 and Sample 2) were assembled to investigate growth mechanism. Sample 1 was plated with increasing current densities of 1, 2, 4, 8 mA cm^{-2} for 60 min, 15 min, 15 min, 30 min respectively. Sample 2 was plated at a constant current density of 0.5 mA cm^{-2} for 120 min. To study removal mechanism, Sample 3 was charged at 1mA cm^{-2} for 60 min then discharged at

2mA cm^{-2} for 30 min. The current was applied in one direction from the bottom electrode to the top electrode. The current densities were calculated using the cross-sectional area of the Kapton tube as the denominator, providing a lower bound on the total lithium surface area exposed to electrolyte on the working electrode. Even though there is no charge/discharge process in a symmetric Li cell, we use term "charge" and "discharge" to describe Li deposition process and stripping process occurring on the negatively and positively charged electrodes, respectively.

The specially designed lithium symmetrical cell was imaged at the Diamond-Manchester Branchline I13 at the Diamond Light Source. An unmonochromated filtered pink beam spectrum of x-rays produced by the undulator in the synchrotron storage ring illuminated the field of view. Such a broader spectrum provides an increased flux whilst maintaining an element of phase contrast in resulting images, reducing scan times. We found that reducing the scan time provided the best mitigation for beam damage and gas evolution suggesting that the degradation process may be limited by diffusion or chemical processes rather than solely x-ray ionization events.

Tomographic reconstruction of the 3D structure was performed after obtaining a series of either 1200 or 1500 projections during a 180 rotation of the sample about the axis parallel to the Kapton tube length. The projections were reconstructed using a filtered back projection algorithm, which minimizes the bright and dark fringes at material boundaries and, making segmentation of the lithium and electrolyte possible by thresholding the grayscale value to produce 3D tomographic image sets with sub-micron resolution. To generate the 3D rendering of the native lithium surface, a single-distance phase retrieval algorithm was used to enhance contrast between the lithium metal (lower x-ray attenuation) and electrolyte (higher attenuation).

5.2.2 Preparation for NMR and SEM experiment

Symmetrical Li metal cells with a 1M $LiPF_6$ dissolved in EC/DMC (1:1 % vol) were prepared to investigate the removal mechanism. The cells were charged at 1.1 mA cm^{-2} for 240 min and discharged at 0.11mA cm^{-2} for 2400min. The average dimension of a Li metal strip is 4 mm x 10 mm x 0.38 mm for the ^{7}Li NMR and SEM experiments. A LEO1550, Germany, SEM

operating at 20 kV with a Robinson backscatter detector was used. A Bio-Logic Science Instruments VSP electrochemical cycler was used to cycle the cells. Electrochemical parameters for charge and discharge are chosen to make the net Li transfer zero. Since the NMR signal is collected from both electrodes, it is impossible to separate the signal of microstructures on the electrode where initial growth is being removed and where Li microstructures are newly formed on the opposite electrode. To reduce the amount of newly formed microstructures, we used a lower current for discharging that is not expected to readily form microstructures. All experiments were performed in real time with the same parameters, previously reported in Chapter 1 and 2.

5.3 Results and Discussion

5.3.1 X-ray tomography study of dendrite formation

In order to study the electrodeposition mechanism of Li metal, symmetric Li-metal cells were prepared (Figure 5.2). The Sample 1 was galvanostatically charged with increased current densities of 1, 2, 4, and 8 mA cm^{-2} for 60 min, 15 min, 15 min, and 30 min, respectively (Sample 1). Radiographic scans of the top electrode were collected every 30 sec during charging and 3D tomographic images of the electrode were taken for 30 min at the beginning of charge. The 3D rendering of the pristine Li metal (Figure 5.2e) shows that the surface is flat with a piece of Li metal sitting at the right edge. At the lower currents of 1, 2 and 4 mA cm^{-2} the growth of Li microstructure was not observed, (not shown in this paper). When the current was increased to 8 mA cm^{-2} multiple nucleation sites occur simultaneously. After current is passed for 90 min, Li starts to plate on the metal and the microstructures have grown dramatically, shown in the 2D slices (Figure 5.2b-d). A large amount of Li microstructures are formed in tree-like structures on the Li electrode.

The Li microstructures evolve mainly in two places, depositing not only at the surface, which is the shortest distance from the opposite electrode, but also on the side of the Li metal

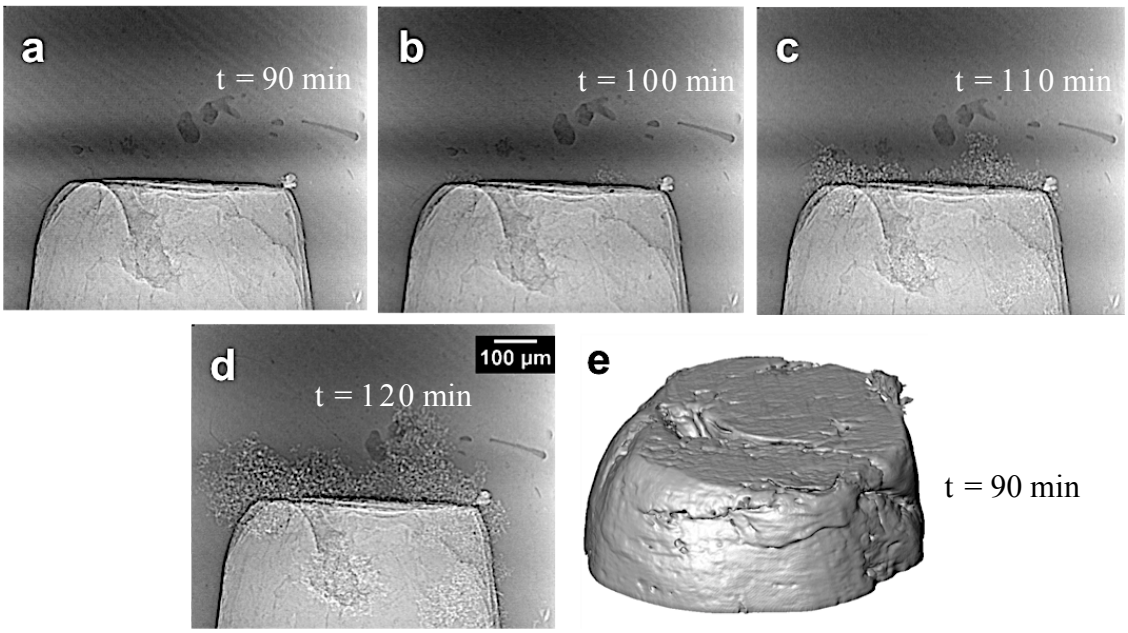

Figure 5.2 Evolution of dendrite growth (Sample 1) on the bottom electrode charged at increased current densities of 1, 2, 4, 8 mA cm^{-2} for 60 min, 15 min, 15 min, 30 min, respectively (a-d) Radiography scan slices of the lithium metal showing the growth of Li microstructure at 8 mA cm^{-2} after 90 min of charge transfer. 2D slice of Li metal captured (a) at 90 min, (b) at 100 min, (c) at 110 min, (d) at 120 min (e) 3D reconstructed surface of Li metal (a) showing the smooth surface with a piece of Li metal sitting on the edge before current flow.

body, between the Li metal and the inner side of the Kapton tube. The nucleation sites at the surface and on the side of the metal are created almost at the same time. Subsequent electrodeposition occurred at the same nucleation sites with no subsequent nucleation events suggesting that transport of lithium ions to the growth regions is a limiting process.

It is still not clear whether the Li microstructures grow from the base of the bulk Li metal, from the tip of existing microstructures or from both of them for Sample 1. To further understand the growth mechanism of Li microstructure, X-ray micro-tomography of a segment of Li microstructure on the bottom electrode plated at 0.5mA cm^{-2} for 120 min (Sample 2) was reconstructed into 3D images with the aid of the phase back-propagation filter. Figure 5.3 shows

2D X-ray tomography captured every 30 min during charging (Figure 5.3a-d) and the 3D reconstructions of the same images (Figure 5.3e-h).

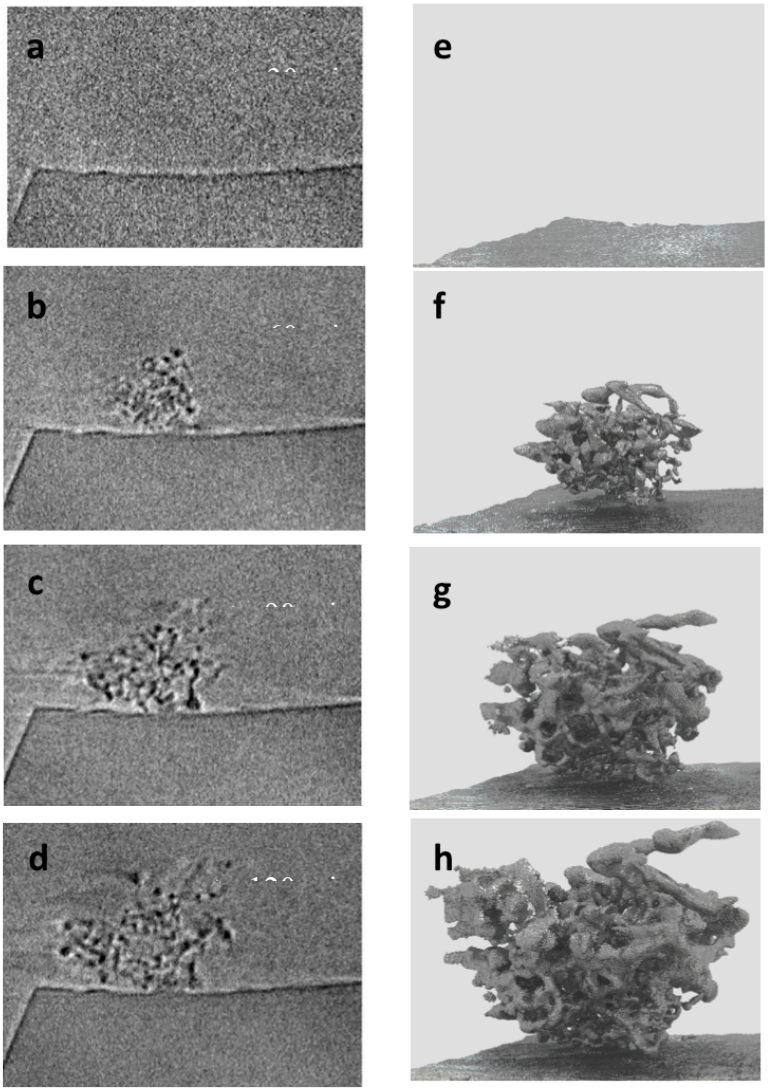

Figure 5.3 X-ray microtomography of Li microstructure growth steps segmented with the aid of the phase back propagation filter. A current density of 0.5mA cm-2 was applied for 120 mins to a Li symmetrical cell (Sample 2). (a-d) 2D X-ray longitudinal tomography slices showing the evolution of Li microstructures. (e-f) 3D reconstructed volumes of 2D images of a-d.

The segment of Li microstructure in 2D slices and 3D reconstructed images shows growth behavior as a function of time (Figure 5.3). The structures near the base of Li metal vary, as well as the tip of the dendrites became thicker and longer (most noticeable in the dendrite protruding at the top right of Figure 5.3f-h). The observation seems in a best agreement with Kohl's results[8,

[9] among various growth mechanical models discussed in the introduction. According to Kohl's mechanism, dendrite growth takes place both at the tip and the base. The growth at the tips of dendrites are electrically active sites for nucleation and the base growth is a phenomenon that may be controlled by mechanical stress from SEI layer and electromigration in vicinity of the electrode where plating occurs. [8, 9]

Even though X-ray tomography data did not show direct proof of the proposed reasons for preferential growth positions, we were able to observe some of them from MRI experiments discussed in Chapter 4. MRI data revealed the depletion zone in the electrolyte near the electrode during formation of microstructures regardless of current densities. In addition, continuous bubble formation was observed during cycling. Reportedly, the possible gases generated from Li metal in EC-DMC electrolyte with $LiPF_6$ salt, were composed mainly of C_2H_4, H_2O, CO, CH_3OH, and CO_2.[21] Presumably, it indicates continuous breaking and reforming of the SEI layer causing an increase in the surface roughness leading to deformation of Li deposition and to release build-up stress underneath the SEI layer.

In conclusion, we observed that nucleation events occurred at multiple sites, at the surface as well as on the side of the Li metal body. After the initiation of microstructure growth, no subsequent nucleation site was observed. Li microstructures were formed from both the base and the tips at the same time after the initiation of protrusions.

5.3.2 X-ray tomography study of dendrite removal mechanism

To investigate the dendrite removal mechanism, x-ray phase contrast tomography images were taken after charging at 1 mA cm^{-2} for 60 min and then after discharging at 2 mA cm^{-2} for 30 minutes a Li symmetrical cell (Sample 3). The amount of Li mass transfer (as determined from the potentiometry) during charging and discharging was kept constant and *in situ* radiographic images were taken every 30 sec. After charging, 2D vertical radiographic scans (5.4a) and slides (5.5b, c) show that Li microstructures were formed on the surface and the growth of a tree-like feature was observed as a function of time.

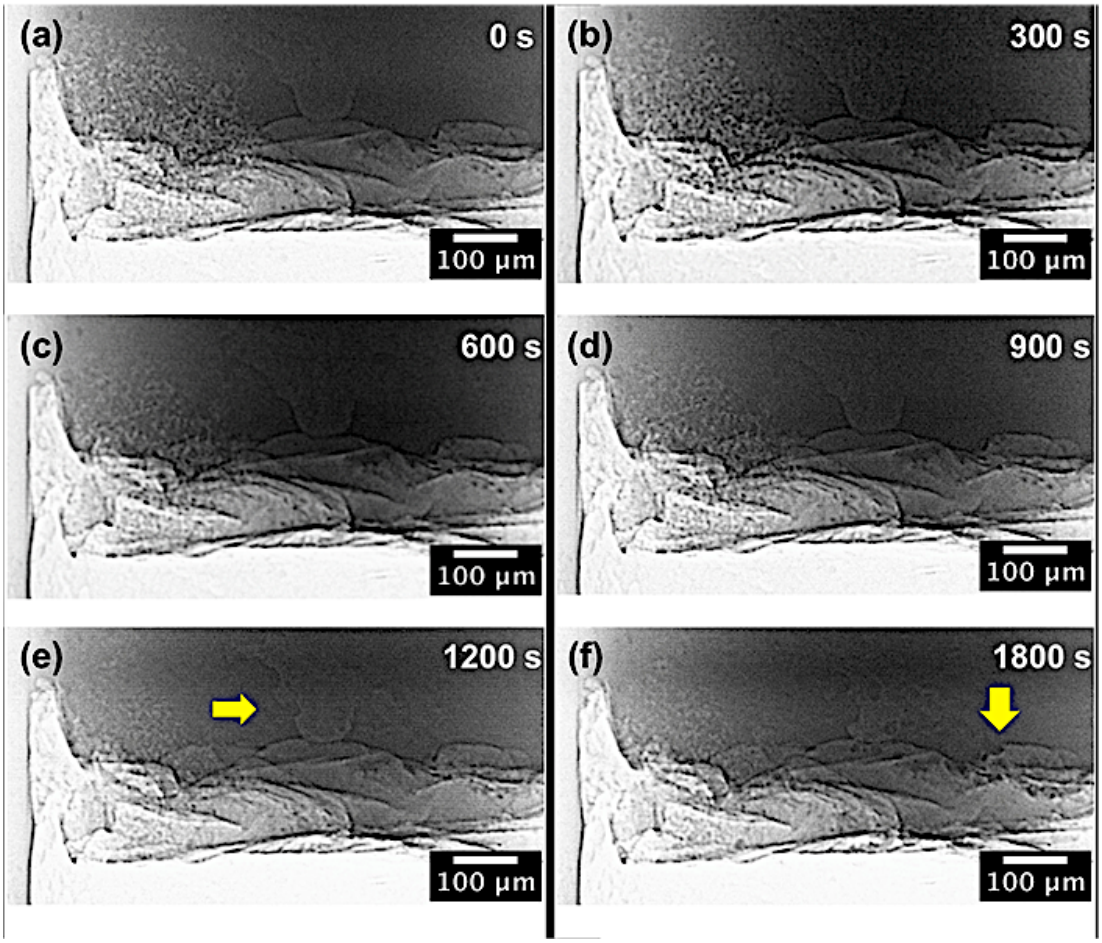

Figure 5.4 Radiographic scans of Li metal showing removal mechanism in two steps, dissolution and pitting under reverse current of 2 mA cm^{-2} applied for 30 min. (a) Li microstructures formed on the rough Li metal surface after charging at 1 mA cm^{-2} for 60min (left side in the scan). (b-e) Li microstructure being removed as a function of time. (f) Significant pitting occurs on Li metal surface and Li metal sticking to the inner wall of Kapton tube. The arrows in yellow refer to change in Li metal surface where the pitting occurs.

The Figure 5.4 displays changes in the lithium surface morphology during discharging only. For the first 20 min of discharge, noticeable removal of the Li microstructures was observed. Even though the scan images are not clear enough to see the individual structures of the microstructure tree, we were able to monitor that they were removed equally in all directions. After 20 min of current passed, a pitting process takes place at the surface of Li metal as soon as the removal of the microstructures ended (Figure 5.4e and f). It is interesting to note that the

preferred stripping location of Li has changed from Li microstructures to bare Li metal. Overall, the consequence of discharging is incomplete removal of the microstructure when net Li transfer is equal to zero.

Pitting process is characterized by the formation of pits that penetrate into the metal resulting in local mass loss. The nucleation of such a pit on metal electrode is a known localized phenomenon, initiated by the SEI layer breakdown.[22, 23] It has been reported that any fatigue cracks where a cyclic loading is applied to below its yield strength in an aging material tend to trigger nucleation and propagation of the pitting.[22] The vertical 2D slices also display the remains of Li microstructures and pitting sites (Figure 5.5d-e). The cross-sectional image of one of the pits (5.5f) at the surface shows a semi circular shape with 39 mm in diameter and 22 mm in depth.

At the end of discharging it was clearly seen that the microstructures could not be removed completely even though the same Li mass is transferred. Also, subsequent nucleation occurs in the vicinity of pits leading the pits in bigger and larger size. The results are in good agreement with the NMR experiments that will be discussed in the following section.

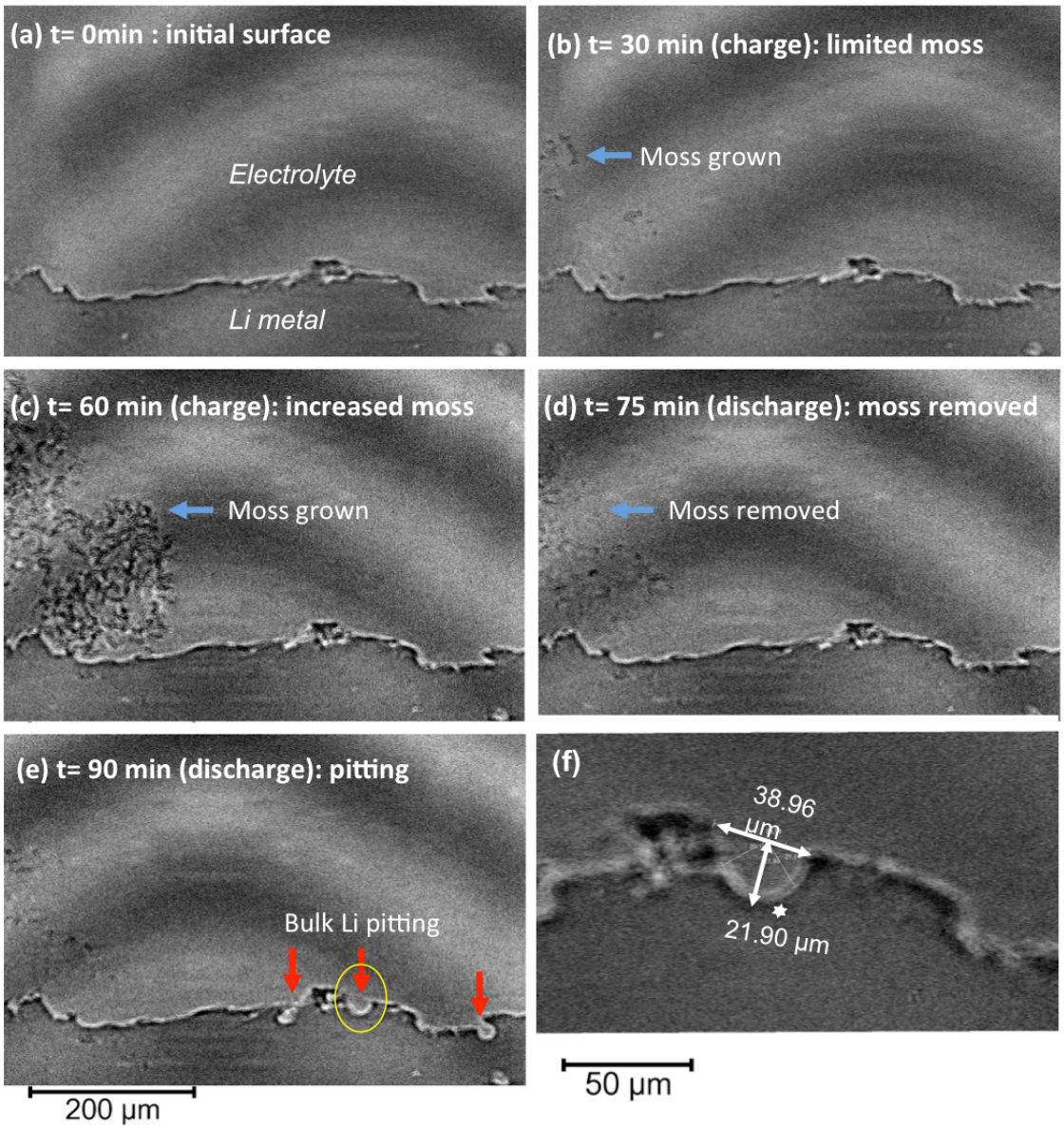

Fig. 5.5 Tomographic slices through reconstructed volumes during 5 stages of lithium microstructure deposition, removal and pitting. The cell was charged first at 1mA cm^{-2} for 60 min and discharged at 2mA cm^{-2} for 30 min. Bulk Li is at the bottom of the image, electrolyte at the top. (a) Initial surface before current flow. (b) After first 30 min of charging showing the Li microstructures formed (c) After charging completed showing development of the microstructures. (d) After first 15 min of discharging showing microstructure removal (e) After discharging is completed showing the remains of the Li microstructures and pitting sites (red arrows) at the surface. (f) Magnified image of the pit shown in (e), where the red arrow in the middle is point at (yellow circle).

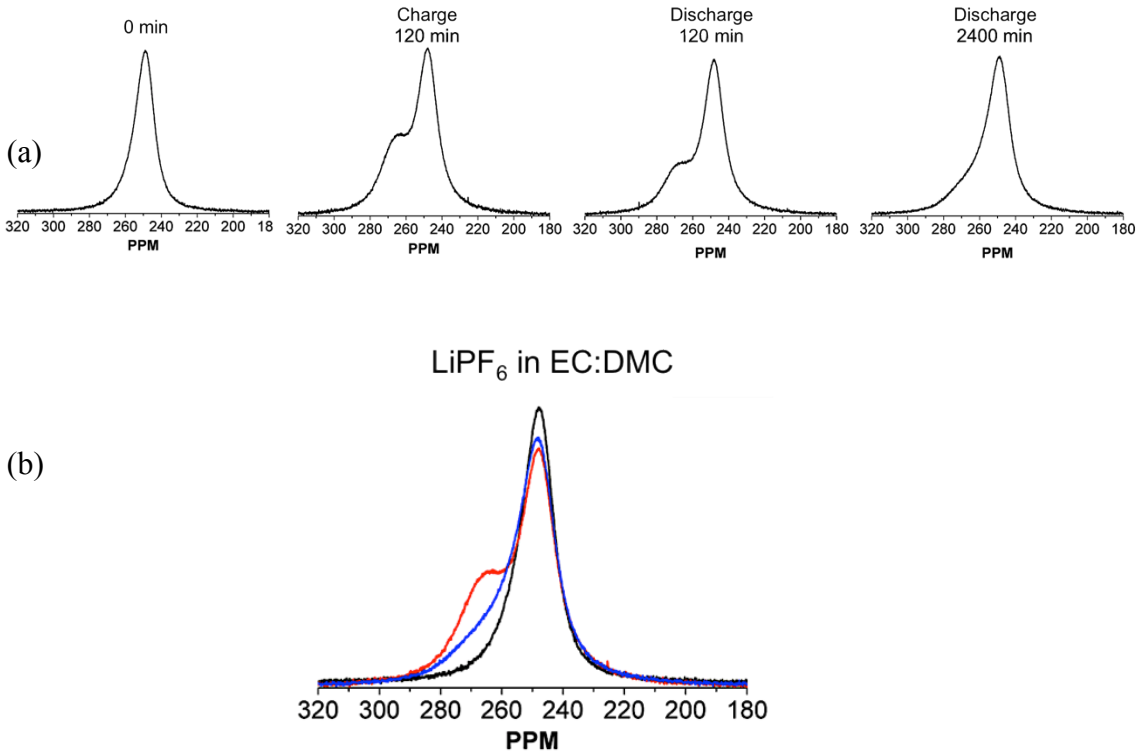

Figure 5.6 The change of ^{7}Li NMR spectra before current flow, after charging and after discharging in a Li symmetric cell containing different electrolytes of $LiPF_6$ dissolved in EC/DMC (a) The evolution of ^{7}Li NMR of the cell charged at 2.2 mA cm^{-2} for 120 min and discharged at 0.11 mA cm^{-2} for 2400 min. (b) The superposed spectra of (a). One of the spectra is obtained before applying current (black line), after charging (red line), and at the end of the discharge (blue line)

5.3.3 NMR and SEM studies of dendrite removal mechanism

NMR technique allows researchers to monitor changes in surface region of metals in real time due to the skin-depth effect with lithium metal. As discussed in Chapter 2, bulk Li metal electrodes appear at a single resonance of 245 ppm in the NMR spectra before current flow. During current flow, an additional Li metal resonance appears at approximately at 265 ppm (± 10 ppm) is observed.

Figure 5.6a shows a series of ^{7}Li NMR spectra of the cell charged at 2.2 mA cm^{-2} for 120

min and discharged at 0.11 mA cm^{-2} for 2400 min in a Li cell containing electrolyte 1M $LiPF_6$ dissolved in EC/DMC, which are collected at different time steps. Figure 5.6b displays the same data of (a) to show clear changes of the spectra. A single spectrum was acquired before current flow (black line), after charging at (red line) and after discharging (blue line). Following the charging process, an additional peak at 270 ppm develops, which associated with the formation of Li dendrite. During cycling, changes in the additional resonance are observed that can be readily explained by the dissolution of microstructural lithium formed during charging, indicating morphological changes are occurring at the surface. Under reverse current, the intensity of this peak is significantly decreased at the end of current flow. Although there was a noticeable decrease in intensity of the peak at 270 ppm, the peak did not disappear completely. The residual intensity of the microstructure peak can be attributed to either the incomplete removal of microstructural lithium or to the formation of microstructures on the opposite electrode.

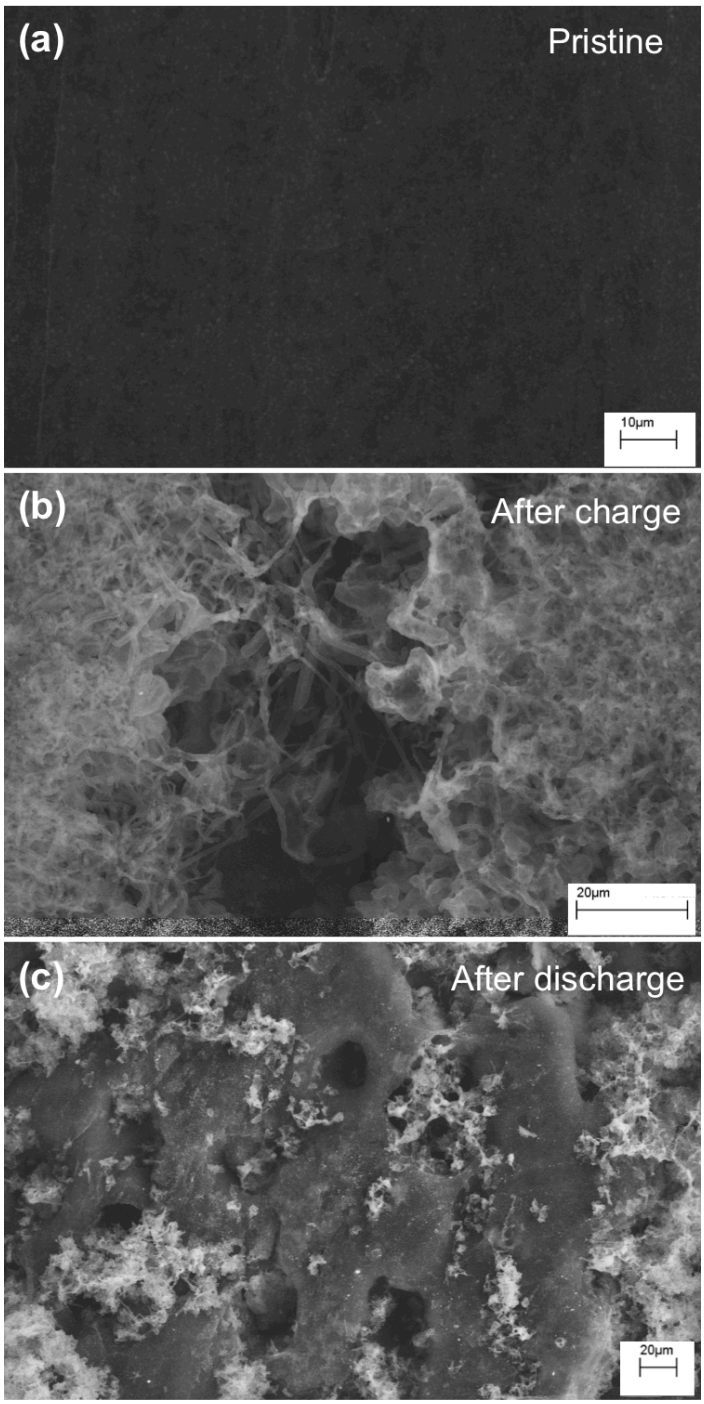

Figure 5.7 SEM images of Li metal in Li/Cegard/Li cells containing 1M $LiPF_6$ in EC: DMC. (a) Pristine, (b) After charging at 1.1 mA cm^{-2} for 240 min, (c) After discharging at 0.11 mA cm^{-2} for 2400 min.

Figure 5.7 depicts SEM images of the lithium metal in a cell with a 1M $LiPF_6$ in EC/DMC electrolyte with different magnifications. The morphology of the metallic lithium surface appears to be significantly different before and after cycling. The SEM image after 240 min of charging clearly shows the formation of a large amount of Li microstructure sparsely spread over the surface (Figure 5.7b). The microstructure observed by SEM correlates well with the growth of the additional NMR peak at 270 ppm. As current was passed in the reverse direction for longer times, small amounts of Li microstructures remains were observed and circular pits on surface of Li metal were also captured, shown in Figure 5.7c.

In conclusion, after applying the reverse current, transferring a same total mass of Li, Li microstructures cannot be removed completely and the pitting process takes place on the surface. The results are in good agreement with the X-ray tomography results. However, it is difficult to capture when pitting starts to occur by NMR and SEM. The combination of NMR and X-ray tomography should be a practical tool to investigations microstructural changes in real time.

5.4 Conclusions

Synchrotron in-line phase contrast x-ray imaging has been used to investigate electrodeposition and dissolution mechanisms of Li microstructures in Li electrochemical cells. The improved spatial resolution and density differentiation presented here enables the ability to discriminate between microstructure morphologies, metallic lithium and electrolyte. During the plating process, we confirm that multiple growth locations occur both from the tip and the base of the microstructures.

The removal mechanism of microstructures occurs in two different steps. Changes in lithium surface area during dissolution can be attributed: to (1) microstructure dissolution, and (2) pitting of bulk Li. The dissolution from the Li microstructures occurred prior to pitting events. We suggest the tips of Li microstructures are fresh metal exposed and electrochemically active sites with high surface area leading to preferential plating/ dissolution other than the surface of bulk Li. Complete removal of microstructures seems impossible at the end of cycling. The NMR and SEM results also support the tomography results that there are always Li microstructures remaining on the surface even after the same amount of Li was transferred.

The cross-section image of pits at the surface shows a semi circular shape indicating spherically shaped pits. We confirmed the pitting events occur at the surface of the bulk Li metal. After the initiation of pits, Li metal in the vicinity of those pits are preferential sites for subsequent nucleation resulting in the growth of pits in bigger and larger size.

Finally, the insights gained from the X-ray tomography obtained in this study indicate that it will be possible to monitor the changes of other LIB electrodes as a function of state of charge of the intact battery. The method could also be helpful in the study of overcharge effect on electrodes such as carbon and silicon.

5.5 References

1. J. W. Diggle, A. R. Despic and J. O. M. Bockris, *J. Electrochem. Soc.*, 1969, **116**, 1503-1514.
2. R. F. Voss and M. Tomikiewicz, *J. Electrochem. Soc.*, 1985, **132**, 371-375.
3. C. Brissot, M. Rosso, J.-N. Chazalviel and S. Lascaud, *J. Electrochem. Soc.*, 1999, **146**, 4393-4400.
4. J.-N. Chazalviel, *Phys. Rev. A*, 1990, **A 42**.
5. J. Yamaki, S. Tobishima, K. Hayashi, K. Saito, Y. Nemoto and M. Arakawa, *J. Power Sources*, 1998, **74**, 219-227.
6. C. Brissot, M. Rosso, J. N. Chazalviel and S. Lascaud, *J. Power Sources*, 1999, **81**, 925-929.
7. C. Brissot, M. Rosso, J.-N. Chazalviel, P. Baudry and S. Lascaud, *Electrochim. Acta*, 1998, **43**, 1569.
8. J. K. Stark, Y. Ding and P. A. Kohl, *J. Electrochem. Soc.*, 2013, **160**, D337-D342.
9. J. K. S. Goodman and P. A. Kohl, *J. Electrochem. Soc.*, 2014, **161**, D418-D424.
10. C. M. Lopez, J. T. Vaughey and D. W. Dees, *J. Electrochem. Soc.*, 2009, **156**, A726-A729.
11. F. Orsini, A. Du Pasquier, B. Beaudoin, J. M. Tarascon, M. Trentin, N. Langenhuizen, E. De Beer and P. Notten, *J. Power Sources*, 1998, **76**, 19-29.
12. M. Dolle, L. Sannier, B. Beaudoin, M. Trentin and J. M. Tarascon, *Electrochem. Solid-State Lett.*, 2002, **5**, A286-A289.
13. L. Gireaud, S. Grugeon, S. Laruelle, B. Yrieix and J. M. Tarascon, *Electrochem. Commun.*, 2006, **8**, 1639-1649.
14. K. Nishikawa, T. Mori, T. Nishida, Y. Fukunaka, M. Rosso and T. Homma, *J. Electrochem. Soc.*, 2010, **157**, A1212.

15. R. Bhattacharyya, B. Key, H. Chen, A. S. Best, A. F. Hollenkamp and C. P. Grey, *Nat. Mater.*, 2010, **9**, 504-510.

16. S. Chandrashekar, N. M. Trease, H. J. Chang, L.-S. Du, C. P. Grey and A. Jerschow, *Nat. Mater.*, 2012, **11**, 311-315.

17. N. Schweikert, A. Hofmann, M. Schulz, M. Scheuermann, S. T. Boles, T. Hanemann, H. Hahn and S. Indris, *J. Power Sources*, 2013, **228**, 237-243.

18. P. R. Shearing, L. E. Howard, P. S. Jørgensen, N. P. Brandon and S. J. Harris, *Electrochem. Commun.*, 2010, **12**, 374-377.

19. D.S Eastwood, P. M Bayley, H. J. Chang, O. O. Taiwo, J. Vila-Comamala, D. JL. Brett, C. Rau, P. J. Withers, P. R. Shearing, C. P. Grey and P. D. Lee, *Chem. Comm.*, 2015, **51**, 266-268.

20. K. J. Harry, D. T. Hallinan, D. Y. Parkinson, A. A. MacDowell and N. P. Balsara, *Nat. Mater.*, 2013, **13**, 69-73.

21. D. Aurbach, E. Zinigrad, Y. Cohen and H. Teller, *Solid State Ionics*, 2002, **148**, 405-416.

22. A. Kolios, S. Srikanth and K. Salonitis, *Procedia CIRP*, 2014, **13**, 230-236.

23. G. S. Frankel, *J. Electrochem. Soc.*, 1998, **145**, 2186-2198.

6. Conclusion and Remarks

Li metal, having the highest energy density, represents the ultimate anode material for lithium ion batteries and its use is integral to the functioning of new high energy density technologies such as Li/S and Li/air. However, there are still critical safety issues preventing the commercialization of Li metal secondary batteries, caused by the growth of Li microstructures, specifically dendrites, that can result in short-circuits and lead to cell failure. Although various techniques have been used to probe the electrochemical mechanisms of dendrite formation, they are generally limited to qualitative information about the microstructure morphology.

In situ NMR has a demonstrated ability to capture real time structural changes that are not obtainable via *ex situ* studies, such as the formation of metastable states and microstructural Li. This work provides the first assignments of the Li metal NMR shifts to the different microstructure morphologies observed by SEM, and supported by susceptibility calculations. The results are critical in the development of a method to monitor cell failure *in situ*. The ability of NMR to distinguish different types of Li microstructures lays the groundwork aimed at identifying the conditions (e.g., additives, applied current) where microstructural formation is minimized.

A combined MRI study of the ^{7}Li electrolyte and ^{7}Li metal allows us to directly correlate the growth of dendrites (and other types of microstructure) with changes in the electrolyte concentration gradient. The accurate estimations of the start time of dendrite growth can be achieved using Chemical Shift Images of the ^{7}Li metal signal and the electrolyte depletion from 1D ^{7}Li electrolyte images. Also, ^{1}H images can be used for *in situ* battery NMR to investigate changes in the electrolyte and electrodes under different conditions.

Synchrotron x-ray imaging has monitored the deposition/dissolution of Li microstructures in real time. The improved spatial resolution and density differentiation enables discrimination between microstructure morphologies, metallic lithium and electrolyte. The insights gained from the x-ray tomography study make it a promising approach for the study of other LIB electrode

materials such as carbon and silicon. The method could also be helpful in the study of overcharge effects on the surface of electrodes.

Visualizing small changes on the surface of the batteries' electrodes allows one then, in principle, to test many different battery designs and materials under normal operating conditions (charging and discharging cycles). New electrode and electrolyte materials are constantly being developed, and these noninvasive NMR, MRI and X-ray tomography technologies could provide indispensible insights into the microscopic processes inside batteries, which hold the key to eventually making batteries lighter, safer, and more versatile. Both electrolyte and electrode surfaces can be visualized with the techniques, thus providing a comprehensive picture of the batteries' performance-limiting processes.

7. References

Chapter 1

1. C. Brissot, M. Rosso, J.-N. Chazalviel and S. Lascaud, *J. Electrochem. Soc.*, 1999, **146**, 4393-4400.
2. J. M. Tarascon and M. Armand, *Nature*, 2001, **414**, 359-367.
3. D. Aurbach, Y. Gofer and J. Langzam, *J. Electrochem. Soc.*, 1989, **136**, 3198-3205.
4. E. Peled, *J. Electrochem. Soc.*, 1979, **126**, 2047-2051.
5. D. Aurbach, I. Weissman, H. Yamin and E. Elster, *J. Electrochem. Soc.*, 1998, **145**, 1421-1426.
6. J. B. Goodenough and Y. Kim, *Chem. Mater.*, 2010, **22**, 587-603.
7. J. B. Bates, *United states patent 5314765*, 1994.
8. P. Arora and Z. M. Zhang, *Chem. Rev.*, 2004, **104**, 4419-4462.
9. P. C. Howlett, D. R. MacFarlane and A. F. Hollenkamp, *Electrochem. Solid-State Lett.*, 2004, **7**, A97-A101.
10. X. W. Zhang, Y. X. Li, S. A. Khan and P. S. Fedkiw, *J. Electrochem. Soc.*, 2004, **151**, A1257-A1263.
11. T. Tatsuma, M. Taguchi, M. Iwaku, T. Sotomura and N. Oyama, *J. Electroanal. Chem.*, 1999, **472**, 142-146.
12. M. Armand and J. M. Tarascon, *Nature*, 2008, **451**, 652-657.
13. M. S. Whittingham, *Proc. IEEE*, 2012 **100**, 1518-1534.
14. M. R. Palacin, *Chem. Soc. Rev.*, 2009, **38**, 2565-2575.
15. C. M. Park, J. H. Kim, H. Kim and H. J. Sohn, *Chem. Soc. Rev.*, 2010, **39**, 3115-3141.
16. N.-m. h. b. Wiki: Lead-acid battery.
17. S. Megahed and B. Scrosati, *J. Power Sources*, 1994, **51**, 79-104.
18. T. Hirai, I. Yoshimatsu and J. Yamaki, *J. Electrochem. Soc.*, 1994, **141**, 611-614.
19. S. I. Tobishima, K. Hayashi, Y. Nemoto and J. I. Yamaki, *Electrochim. Acta*, 1998, **43**, 925-933.
20. M. K. Yuichi Sato, Hirokazu Niki, Mitsushi Ueno, Kenji Murata, Tamotsu Shirogami, Tsutomu Takamura, *J. Power Sources*, 1983, **9**, 147-159.

21. D. Aurbach, E. Zinigrad, Y. Cohen and H. Teller, *Solid State Ionics*, 2002, **148**, 405-416.

22. Y. S. Cohen, Y. Cohen and D. Aurbach, *J. Phys. Chem. B*, 2000, **104**, 12282-12291.

23. S. Shiraishi, K. Kanamura and Z. Takehara, *J. Phys. Chem. B*, 2001, **105**, 123-134.

24. K. Kanamura, S. Shiraishi and Z. Takehara, *J. Electrochem. Soc.*, 1996, **143**, 2187-2197.

25. X. H. Liu, L. Zhong, L. Q. Zhang, A. Kushima, S. X. Mao, J. Li, Z. Z. Ye, J. P. Sullivan and J. Y. Huang, *Appl. Phys. Lett.*, 2011, **98**.

26. F. Orsini, A. Du Pasquier, B. Beaudoin, J. M. Tarascon, M. Trentin, N. Langenhuizen, E. De Beer and P. Notten, *J. Power Sources*, 1998, **76**, 19-29.

27. C. M. Lopez, J. T. Vaughey and D. W. Dees, *J. Electrochem. Soc.*, 2009, **156**, A726-A729.

28. R. E. Hoffman, *J. Magn. Reson.*, 2006, **178**, 237-247.

29. I. Epelboin, M. Froment, M. Garreau, J. Thevenin and D. Warin, *J. Electrochem. Soc.*, 1980, **127**, 2100-2104.

30. M. Arakawa, S. Tobishima, Y. Nemoto, M. Ichimura and J. Yamaki, *J. Power Sources*, 1993, **43**, 27-35.

31. S. H. Bo, F. Wang, Y. Janssen, D. L. Zeng, K. W. Nam, W. Q. Xu, L. S. Du, J. Graetz, X. Q. Yang, Y. M. Zhu, J. B. Parise, C. P. Grey and P. G. Khalifah, *J. Mater. Chem.*, 2012, **22**, 8799-8809.

32. B. Key, M. Morcrette, J. M. Tarascon and C. P. Grey, *J. Am. Chem. Soc.*, 2011, **133**, 503-512.

33. C. P. Grey and Y. J. Lee, *Solid State Sci.*, 2003, **5**, 883-894.

34. R. Bhattacharyya, B. Key, H. Chen, A. S. Best, A. F. Hollenkamp and C. P. Grey, *Nat. Mater.*, 2010, **9**, 504-510.

35. S. Chandrashekar, N. M. Trease, H. J. Chang, L.-S. Du, C. P. Grey and A. Jerschow, *Nat. Mater.*, 2012, **11**, 311-315.

36. N. Schweikert, A. Hofmann, M. Schulz, M. Scheuermann, S. T. Boles, T. Hanemann, H. Hahn and S. Indris, *J. Power Sources*, 2013, **228**, 237-243.

37. J. Wandt, C. Marino, P. Jakes, R. Eichel, H. A. Gasteiger and J. Granwehr, *Energy Environ. Sci.*, 2015.

38. M. Sathiya, J. B. Leriche, E. Salager, D. Gourier, J. M. Tarascon and H. Vezin, *Nat. Commun.*, 2015, **6**, 6276.

39. C. Kittel, *Introduction to Solid State Physics*, New York: Wiley, 1976.

40. J. W. Diggle, A. R. Despic and J. O. M. Bockris, *J. Electrochem. Soc.*, 1969, **116**, 1503-1514.

41. T. Witten and L. Sander, *Phys. Rev. Lett.*, 1981, **47**, 1400-1403.

42. J.-N. Chazalviel, *Phys. Rev. A*, 1990, **A 42**.

43. C. Brissot, M. Rosso, J.-N. Chazalviel, P. Baudry and S. Lascaud, *Electrochim. Acta*, 1998, **43**, 1569.

44. J. Yamaki, S. Tobishima, K. Hayashi, K. Saito, Y. Nemoto and M. Arakawa, *J. Power Sources*, 1998, **74**, 219-227.

45. R. V. Magan and R. Sureshkumar, *J. Phys. Chem. B*, 2003, **107**, 10513-10520.

46. M. Z. Mayers, J. W. Kaminski and T. F. Miller, *J. Phys. Chem. C*, 2012, **116**, 26214-26221.

47. P. Meakin, *Phy. Rev. Lett.*, 1983, **51**, 1119.

48. R. F. Voss and M. Tomikiewicz, *J. Electrochem. Soc.*, 1985, **132**, 371-375.

49. C. Brissot, M. Rosso, J. N. Chazalviel and S. Lascaud, *J. Power Sources*, 2001, **94**, 212-218.

50. J. K. Stark, Y. Ding and P. A. Kohl, *J. Electrochem. Soc.*, 2013, **160**, D337-D342.

51. R. K. Harris, E. D. Becker, S. M. C. De Menezes, P. Granger, R. E. Hoffman and K. W. Zilm, *Solid State Nucl. Magn. Reson.*, 2008, **33**, 41-56.

52. C. P. Slichter, *Principles of Magnetic Resonance*, Springer-Verlag, 1990.

53. N. M. Trease, L. Zhou, H. J. Chang, B. Y. Zhu and C. P. Grey, *Solid State Nucl. Magn. Reson.*, 2012, **42**, 62-70.

54. A. Kubo, T. P. Spaniol and T. Terao, *J. Magn. Reson.*, 1998, **133**, 330-340.

55. A. J. Ilott, S. Chandrashekar, A. Klockner, H. J. Chang, N. M. Trease, C. P. Grey, L. Greengard and A. Jerschow, *J. Magn. Reson.*, 2014, **245**, 143-149.

56. R.E. Gerald II, R. J. Klingler, G. S.́ı, C. S. Johnson, L. G. Scanlon and J. W. Rathke, *J. Power Sources*, 2000, **89**, 237-243.

57. M. Letellier, F. Chevallier and M. Morcrette, *Carbon*, 2007, **45**, 1025-1034.

58. J.M.Tarascon, A.S.Gozdz, C.Schmutz, F.Shokoohi and P.C.Warren, *Solid state Ionics*, 1996, **86**, 49-54.

59. J. Kawamura and Y. Iwai, *Tohoku Univ Takes MRI Images of Li-ion Battery.* http://techon.nikkeibp.co.jp/english/NEWS_EN/20090709/172827/ 2009.

60. R. E. Gerald, R. J. Klingler, G. Sandi, C. S. Johnson, L. G. Scanlon and J. W. Rathke, *J. Power Sources*, 2000, **89**, 237-243.

61. lightboxradiology.com.au., May 2015.

62. M. A. Bernstein, K. F. King and X. J. Zhou, *Elsevier*, 2004.

63. http://mri-q.com/what-is-phase-encoding.html, May 2015.

64. http://neurosurgerysurvivalguide.com/roundy/, May 2015.

65. D.S Eastwood, P. M Bayley, H. J. Chang, O. O. Taiwo, J. Vila-Comamala, D. JL. Brett, C. Rau, P. J. Withers, P. R. Shearing, C. P. Grey and P. D. Lee, *Chem. Comm.*, 2015, **51**, 266-268.

Chapter 2

1. http://www.gelifesciences.com/webapp/wcs/stores/servlet/catalog/en/GELifeSciences-us/products/AlternativeProductStructure_16176/28418346.

2. P. Arora and Z. M. Zhang, *Chem. Rev.*, 2004, **104**, 4419-4462.

3. R. Bhattacharyya, B. Key, H. Chen, A. S. Best, A. F. Hollenkamp and C. P. Grey, *Nat. Mater.*, 2010, **9**, 504-510.

4. R. Salomir, B. D. de Senneville and C. T. W. Moonen, *Concepts Magn. Reson.* , 2003, **19B**, 26-34.

5. J. P. Marques and R. Bowtell, *Concepts Magn. Reson. B* 2005, **25B**, 65-78.

6. A. J. Ilott, S. Chandrashekar, A. Klockner, H. J. Chang, N. M. Trease, C. P. Grey, L. Greengard and A. Jerschow, *J. Magn. Reson.*, 2014, **245**, 143-149.

7. D. Gugan, *Phys. Rev. B*, 1997, **56**.

8. F. T. Hedgcock, *Phys. Rev. Lett.*, 1960, **5**, 420-423.

9. N. M. Trease, L. Zhou, H. J. Chang, B. Y. Zhu and C. P. Grey, *Solid State Nucl. Magn. Reson.*, 2012, **42**, 62-70.

10. R. K. Harris, E. D. Becker, S. M. C. De Menezes, P. Granger, R. E. Hoffman and K. W. Zilm, *Solid State Nucl. Magn. Reson.*, 2008, **33**, 41-56.

11. C. P. Slichter, *Principles of Magnetic Resonance*, Springer-Verlag, 1990.

12. R. E. Hoffman, *J. Magn. Reson.*, 2006, **178**, 237-247.

13. A. Kubo, T. P. Spaniol and T. Terao, *J. Magn. Reson.*, 1998, **133**, 330-340.

14. N. Schweikert, A. Hofmann, M. Schulz, M. Scheuermann, S. T. Boles, T. Hanemann, H. Hahn and S. Indris, *J. Power Sources*, 2013, **228**, 237-243.

15. S. Chandrashekar, N. M. Trease, H. J. Chang, L.-S. Du, C. P. Grey and A. Jerschow, *Nat. Mater.*, 2012, **11**, 311-315.

16. T. Hirai, I. Yoshimatsu and J. Yamaki, *J. Electrochem. Soc.*, 1994, **141**, 611-614.

17. S. I. Tobishima, K. Hayashi, Y. Nemoto and J. I. Yamaki, *Electrochim. Acta*, 1998, **43**, 925-933.

Chapter 3

1. F. Ding, W. Xu, G. L. Graff, J. Zhang, M. L. Sushko, X. Chen, Y. Shao, M. H. Engelhard, Z. Nie, J. Xiao, X. Liu, P. V. Sushko, J. Liu and J. G. Zhang, *J. Am. Chem. Soc.*, 2013, **135**, 4450-4456.

2. F. Ding, W. Xu, X. Chen, J. Zhang, Y. Shao, M. H. Engelhard, Y. Zhang, T. A. Blake, G. L. Graff, X. Liu and J.-G. Zhang, *J. Phys. Chem. C*, 2014, **118**, 4043-4049.

3. D. Aurbach, Y. Ein-Ely and A. Zaban, *J. Electrochem. Soc.*, 1994, **141**, L1-L3.

4. K. Xu, *Chem. Rev.*, 2004, **104**, 4304-4117.

5. Y. S. Cohen, Y. Cohen and D. Aurbach, *J. Phys. Chem. B*, 2000, **104**, 12282-12291.

6. D. Aurbach, *J. Power Sources*, 2000, **89**, 206-218.

7. K. Hayash, Y. Nemoto, S. Tobishima and J. Yamaki, *Electrochim. Acta*, 1999, **44**, 2337-2344.

8. O. Crowther and A. C. West, *J. Electrochem. Soc.*, 2008, **155**, A806-A811.

9. S. Chandrashekar, N. M. Trease, H. J. Chang, L.-S. Du, C. P. Grey and A. Jerschow, *Nat. Mater.*, 2012, **11**, 311-315.

10. H. J. Chang, N. M. Trease, A. J. Ilott, D. Zeng, L. S. Du, A. Jerschow and C. P. Grey, *J. Phys. Chem. C (Accepted)*, 2015.

11. R. Fong, U. Vonsacken and J. R. Dahn, *J. Electrochem. Soc.*, 1990, **137**, 2009-2013.

12. S. H. Lee, *J. Phys. Chem.*, 1996, **100**, 1420-1425.

13. S. H. Lee and J. C. Rasaiah, *J. Chem. Phys.*, 1994, **101**, 6964.

14. H. Ohtaki, *Pure & Appl. Chem.*, 1987, **59**, 1143-1150.

15. S. K. Jeong, M. Inaba, Y. Iriyama, T. Abe and Z. Ogumi, *Electrochim. Acta*, 2002, **47**, 1975-1982.

16. Y. Matsuda, M. Ishikawa., S.Yoshitake and M. Morita, *J. Power Sources*, 1995, **54**, 301-305.

17. C. W. Bale, *J. Phase Equilibr.*, 1989, **10**, 262-264.

18. S. S. Zhang, *J. Power Sources*, 2006, **162**, 1379-1394.

19. Z. Li, J. Huang, B. Yann Liaw, V. Metzler and J. Zhang, *J. Power Sources*, 2014, **254**, 168-182.

20. R. Bhattacharyya, B. Key, H. Chen, A. S. Best, A. F. Hollenkamp and C. P. Grey, *Nat. Mater.*, 2010, **9**, 504-510.

Chapter 4

1. J. W. Diggle, A. R. Despic and J. O. M. Bockris, *J. Electrochem. Soc.*, 1969, **116**, 1503-1514.

2. J. L. Barton and J. O. M. Bockris, *Proc. R. Soc. London, Ser. A*, 1962, **268**, 485.

3. R. V. Magan and R. Sureshkumar, *J. Phys. Chem. B*, 2003, **107**, 10513-10520.

4. T. Witten and L. Sander, *Phys. Rev. Lett.*, 1981, **47**, 1400-1403.

5. J.-N. Chazalviel, *Phys. Rev. A*, 1990, **A 42**.

6. C. Brissot, M. Rosso, J.-N. Chazalviel and S. Lascaud, *J. Electrochem. Soc.*, 1999, **146**, 4393-4400.

7. C. Brissot, M. Rosso, J.-N. Chazalviel, P. Baudry and S. Lascaud, *Electrochim. Acta*, 1998, **43**, 1569.

8. C. Brissot, M. Rosso, J. N. Chazalviel and S. Lascaud, *J. Power Sources*, 2001, **94**, 212-218.

9. C. Brissot, M. Rosso, J. N. Chazalviel and S. Lascaud, *J. Power Sources*, 1999, **81**, 925-929.

10. H. E. Park, C. H. Hong and W. Y. Yoon, *J. Power Sources*, 2008, **178**, 765-768.

11. S. Chandrashekar, N. M. Trease, H. J. Chang, L.-S. Du, C. P. Grey and A. Jerschow, *Nat. Mater.*, 2012, **11**, 311-315.

12. M. Klett, M. Giesecke, A. Nyman, F. Hallberg, R. W. Lindstrom, G. Lindbergh and I. Furo, *J. Am. Chem. Soc.*, 2012, **134**, 14654-14657.

13. S. Klamor, K. Zick, T. Oerther, F. M. Schappacher, M. W. and and G. Brunklaus, *Phys. Chem. Chem. Phys.*, 2015, **17**, 4458-4465.

14. H. S. Gutowsky and B. R. McGarvey, *J. Chem. Phys.*, 1952, **20**, 1472-1477.

15. J. P. Marques and R. Bowtell, *Concepts Magn. Reson. B* 2005, **25B**, 65-78.

16. A. J. Ilott, S. Chandrashekar, A. Klockner, H. J. Chang, N. M. Trease, C. P. Grey, L. Greengard and A. Jerschow, *J. Magn. Reson.*, 2014, **245**, 143-149.

17. M. M. Britton, *Chemphyschem : a European journal of chemical physics and physical chemistry*, 2014, **15**, 1731-1736.

18. M. M. Britton, P. M. Bayley, P. C. Howlett, A. J. Davenport and M. Forsyth, *J. Phys. Chem. Lett.*, 2013, **4**, 3019-3023.

19. N. M. Trease, L. Zhou, H. J. Chang, B. Y. Zhu and C. P. Grey, *Solid State Nucl. Magn. Reson.*, 2012, **42**, 62-70.

20. A. Kubo, T. P. Spaniol and T. Terao, *J. Magn. Reson.*, 1998, **133**, 330-340.

21. D. Gugan, *Phys. Rev. B*, 1997, **56**.

22. H. J. Chang, N. M. Trease, A. J. Ilott, D. Zeng, L. S. Du, A. Jerschow and C. P. Grey, *J. Phys. Chem. C (Accepted)*, 2015.

23. N. Sato, *J. Power Sources*, 2001, **99**, 70-77.

24. D. Aurbach, E. Zinigrad, Y. Cohen and H. Teller, *Solid State Ionics*, 2002, **148**, 405-416.

25. M. Z. Mayers, J. W. Kaminski and T. F. Miller, *J. Phys. Chem. C*, 2012, **116**, 26214-26221.

26. E. Peled, *J. Electrochem. Soc.*, 1979, **126**, 2047-2051.

27. S. K. Jeong, M. Inaba, Y. Iriyama, T. Abe and Z. Ogumi, *Electrochim. Acta*, 2002, **47**, 1975-1982.

28. D. Aurbach, Y. Gofer, M. B. Zion and P. Aped, *J. Electrochem. Soc.*, 1992, **339**, 451-471.

29. D. Aurbach, E. Zinigrad, H. Teller and P. Danb, *J. Electrochem. Soc.*, 2000, **147**, 1274-1279.

30. D. Aurbach, *J. Power Sources*, 2000, **89**, 206-218.

Chapter 5

1. J. W. Diggle, A. R. Despic and J. O. M. Bockris, *J. Electrochem. Soc.*, 1969, **116**, 1503-1514.

2. R. F. Voss and M. Tomikiewicz, *J. Electrochem. Soc.*, 1985, **132**, 371-375.

3. C. Brissot, M. Rosso, J.-N. Chazalviel and S. Lascaud, *J. Electrochem. Soc.*, 1999, **146**, 4393-4400.

4. J.-N. Chazalviel, *Phys. Rev. A*, 1990, **A 42**.

5. J. Yamaki, S. Tobishima, K. Hayashi, K. Saito, Y. Nemoto and M. Arakawa, *J. Power Sources*, 1998, **74**, 219-227.

6. C. Brissot, M. Rosso, J. N. Chazalviel and S. Lascaud, *J. Power Sources*, 1999, **81**, 925-929.

7. C. Brissot, M. Rosso, J.-N. Chazalviel, P. Baudry and S. Lascaud, *Electrochim. Acta*, 1998, **43**, 1569.

8. J. K. Stark, Y. Ding and P. A. Kohl, *J. Electrochem. Soc.*, 2013, **160**, D337-D342.

9. J. K. S. Goodman and P. A. Kohl, *J. Electrochem. Soc.*, 2014, **161**, D418-D424.

10. C. M. Lopez, J. T. Vaughey and D. W. Dees, *J. Electrochem. Soc.*, 2009, **156**, A726-A729.

11. F. Orsini, A. Du Pasquier, B. Beaudoin, J. M. Tarascon, M. Trentin, N. Langenhuizen, E. De Beer and P. Notten, *J. Power Sources*, 1998, **76**, 19-29.

12. M. Dolle, L. Sannier, B. Beaudoin, M. Trentin and J. M. Tarascon, *Electrochem. Solid-State Lett.*, 2002, **5**, A286-A289.

13. L. Gireaud, S. Grugeon, S. Laruelle, B. Yrieix and J. M. Tarascon, *Electrochem. Commun.*, 2006, **8**, 1639-1649.

14. K. Nishikawa, T. Mori, T. Nishida, Y. Fukunaka, M. Rosso and T. Homma, *J. Electrochem. Soc.*, 2010, **157**, A1212.

15. R. Bhattacharyya, B. Key, H. Chen, A. S. Best, A. F. Hollenkamp and C. P. Grey, *Nat. Mater.*, 2010, **9**, 504-510.

16. S. Chandrashekar, N. M. Trease, H. J. Chang, L.-S. Du, C. P. Grey and A. Jerschow, *Nat. Mater.*, 2012, **11**, 311-315.

17. N. Schweikert, A. Hofmann, M. Schulz, M. Scheuermann, S. T. Boles, T. Hanemann, H. Hahn and S. Indris, *J. Power Sources*, 2013, **228**, 237-243.

18. P. R. Shearing, L. E. Howard, P. S. Jørgensen, N. P. Brandon and S. J. Harris, *Electrochem. Commun.*, 2010, **12**, 374-377.

19. D.S Eastwood, P. M Bayley, H. J. Chang, O. O. Taiwo, J. Vila-Comamala, D. JL. Brett, C. Rau, P. J. Withers, P. R. Shearing, C. P. Grey and P. D. Lee, *Chem. Comm.*, 2015, **51**, 266-268.

20. K. J. Harry, D. T. Hallinan, D. Y. Parkinson, A. A. MacDowell and N. P. Balsara, *Nat. Mater.*, 2013, **13**, 69-73.

21. D. Aurbach, E. Zinigrad, Y. Cohen and H. Teller, *Solid State Ionics*, 2002, **148**, 405-416.

22. A. Kolios, S. Srikanth and K. Salonitis, *Procedia CIRP*, 2014, **13**, 230-236.

23. G. S. Frankel, *J. Electrochem. Soc.*, 1998, **145**, 2186-2198.